ELECTRONIC AND THERMAL BEHAVIOR OF GERMANIUM TELLURIDE-TIN TELLURIDE SOLID SOLUTIONS NEAR THE STRUCTURAL PHASE TRANSITION

By

Corey C. Cooling

A DISSERTATION

Submitted to
Michigan State University
in partial fulfillment of the requirements
for the degree of

Physics – Doctor of Philosophy

2023

ABSTRACT

Humanity finds itself in an energy crisis, where our energy demands now and in the future are far out of balance with our ability to produce that energy safely and thoughtfully. Many energy systems today utilize the chemical energy stored in hydrocarbons in processes that create, in addition to ubiquitous carbon dioxide, extra energy in the form of heat that is usually wasted. This extra energy in the form of heat, in combustion engines and in other applications, instead of being wasted could be converted into usable electrical energy with the help of a class of materials called thermoelectrics.

Thermoelectric devices are a class of materials, usually semiconductors, that convert temperature gradients into usable electrical energy. One critical drawback of thermoelectric technology today is the relatively low efficiency of thermoelectric devices. In order to evaluate a material's efficiency researchers use the dimensionless figure-of-merit, ZT, which is a product of a number of electronic and thermal material properties. By examining the material properties which influence ZT values we can systematically develop higher efficiency thermoelectric devices.

Here we present a study of the structural and transport properties of GeTe-SnTe solid solutions near the temperatures of their structural phase transition. As two well-known class IV-VI semiconducting materials GeTe and SnTe have been well studied and developed for thermoelectric applications, but there exists a relative dearth of research on their solid solutions. As a complete solid solution, Sn can replace Ge at any concentration without changing the crystal system. One aspect about GeTe that makes it interesting for thermoelectrics is that its crystal structure transforms from a low-temperature rhombohedral phase to a high-temperature cubic rocksalt phase about 670K. By contrast, SnTe undergoes a similar transformation at about 100K. Previous studies have shown that in large crystals of GeTe replacing Sn for Ge, $Ge_{(1-x)}Sn_{(x)}Te$, lowers the transition temperature as a function of Sn content. By studying the solid solution across all values of x, $0 \leq x \leq 1$, one has available a unique crystal system with a structural phase transition spanning well above to well below room temperature.

For this study, polycrystalline samples were synthesized from ingots using power metallurgy techniques and their thermoelectric properties were measured from 300-770K.We show x-ray diffraction data to show the phase purity and lattice constant of these solid solutions, as well as observe the elastic constants at room temperature. We report phase transition temperatures from observations of changes in crystal structure at elevated and room temperatures. We then show the electrical conductivity, Seebeck coefficient, and thermal conductivity as a function of temperature and Sn content. Our results show that at low Sn concentrations, Sn atoms fill Ge vacancies that cause a decrease in the electrical conductivity from a reduction of the carrier concentration. At higher Sn concentrations these filled vacancies contribute to an increase in the carrier mobility which offsets the decrease in carrier concentration while also increasing the Seebeck coefficient. The thermal behavior of the system shows strong evidence of alloy scattering with a minimum near concentrations with similar amounts of Ge and Sn. Distinct discontinuities in the total thermal conductivity also provide evidence for the determination of structural transition temperatures. Taken together, these studies enable a complete characterization of the ZT for these materials above room temperature as well as a contribution to the structural phase diagram. The highest ZT values obtained at 400 °C in $Ge_{(1-x)}Sn_{(x)}Te$ were for x-values x=0.05 and x=0.60 with values of 0.36 and 0.31 respectively, which is impressive for unoptimized materials.

Dedicated to Alyssa, my cat Velly, and all the friends we made along the way.

ACKNOWLEDGEMENTS

I would first like to thank my advisor, Dr. Donald T. Morelli, for giving me the opportunity to study in his research group. In addition to being a great advisor with a wealth and depth of knowledge all things solid state physics and thermoelectrics, I thank him for his cheery optimism in the face of the many challenges we overcame in this study and will remember well catching up with him from time to time about Big Ten sports.

I would also like to thank my colleagues in the Morelli group who trained me as well as the Zevalkink research group for adopting me later in my research. I'd like to thank Dr. Jared Williams and Dr. Spencer Waldrop for teaching me about synthesis methods and especially operating the sealing station. I'd like to thank Dr. Daniel Weller for training me on the SPS and for being a resource to test ideas. I owe a deep appreciation for the work of Dr. Vijay Ponnabalam for maintaining the equipment around the laboratory as well as teaching me to build and repair much of the equipment myself. A special thanks to Gill Levental for performing the HT-XRD measurements. I'm appreciative of Ashiq Shawon in showing me how to use the Rigaku XRD and the RUS equipment. I'd like to thank Dr. Mario Calderon and Dr. Sevan Chanakian for their camaraderie as we attempted to refurbish many pieces of equipment as well as many hours of discussion and insight. I'd like to thank Dr. Alex Zevalkink specifically for letting me use her brand-new LFA and sponsoring me for a semester of research.

I'd like to thank my colleagues in the Physics and Astronomy graduate program for their fellowship in studying for graduate exams; especially Thomas Chuna, Dr. Isaac Yandow, Caley Harris, Dr. Daniel Paz, Tom-Erik Haugen, Dr. Tamas Budner, Dr. Kyle Krowpman, Dr. Carl Fields, Cami Monsalve, Dr. Aryn MacGilligan and many unnamed others.

I'd like to thank the faculty and staff I worked with in my classes and teaching

assignments, including Dr. Saul Beceiro Novo, Dr. Daryl McPadden, Dr. Katie Hinko, Dr. Remco Zegers, Mark Olson, and especially Kim Crosslan. I'm grateful for the MSU students who showed up to class with enthusiasm and optimism, especially my 'regulars' at my weekly help sessions. Teaching was a wonderful and challenging part of my time at MSU, especially in the wake of the violence experienced on campus on February 13, 2023. I implore the University to pay its support staff more, especially people critical to the daily functioning of departments.

I'd like to thank my labor union, the Graduate Employees Union, for their support and solidarity during my time here. Their tireless advocacy for graduate students ensured that I never had to worry about health insurance for myself or my partner as well as securing an equitable wage that I could live on during my course of study. I'm thankful for the many volunteers active in the GEU who ensure that its members are protected and represented and to the community forged in that mutual struggle.

I'd like to offer thanks to my teachers at the University of Northern Iowa and Vinton-Shellsburg High School for preparing me to engage in this program. I'd like to thank my undergraduate physics advisor, Dr. Paul Shand, for advising me during my first research experience as well as being a great mentor as I navigated the application process for graduate school. I'd like to thank my high school physics and math teacher Steve McGrew for making me memorize the quadratic formula when I was 15 as well as establishing an excellent math and physics foundation that carried me through my academic career.

Lastly, I'd like to thank my committee members, Dr. Alex Zevalkink, Dr. Xianglin Ke, Dr. Carlo Piermarocchi, and Dr. Scott Pratt. Your guidance and support in navigating a conclusion to these studies as well as dealing with a rather unprecedented sets of circumstances on campus and around the world was invaluable.

TABLE OF CONTENTS

CHAPTER 1 Introduction

Advanced human civilization since the dawn of agriculture has depended on the harmonious management of resources and energy to survive and flourish. After thousands of years of increasingly complex activity, humanity is now faced with new challenges stewarding resources and supplying energy for our many needs and endeavors. Many of these challenges have emerged from trying to meet ever increasing energy demands of western educated industrialized rich and democratic (WEIRD) countries [1]. Demand for energy in the coming decades is expected to continue to grow; however, the natural world's capacity to provide that energy is becoming more and more degraded. This makes the extraction of resources more difficult and therefore costly [1-3]. There is also a growing and incontrovertible scientific consensus that unless we rapidly shift energy systems away from carbon-based fossil fuels, we may push the climate to new equilibrium states marked by inconsistent climate patterns [4-5]. Attempts to condense the complexity of the problem into projections for the future and communicating those issues to the public and decision makers remains a challenge [84]. One formulation of this problem is expressed as the "carbon budget" that estimates we have a dwindling amount of time to make changes to our energy systems at current usage rates [6]. In addition to long-term problems such as removing carbon from the atmosphere there are also short-term problems related to the degradation of cooling aerosols that may be temporarily counteracting the effects of greenhouse gas emissions [7-8]. Any solution to these problems requires energy production and storage systems that look much different than the systems we have today, and so creative and innovative solutions are required. With this in mind, we understand that solving the challenges of the "energy crisis" is critical to the continued sustainable development and flourishing of human civilization.

A key to the development of a sustainable future for energy generation is increasing the efficiency of our existing energy systems as well as obtaining energy from unconventional sources. As it stands today, a large percentage of existing energy systems do not effectively utilize the energy made available from their fuels. A major source of the inefficiency is the energy lost as “wasted” heat [9]. Estimates done yearly by the Lawrence Livermore National Laboratory show that, for many of our power generation systems, a substantial portion of the energy generated is lost as ‘waste’ heat (see below in Figure 1.1) [10]. While there are entropic limits on the total efficiency of these processes, if we are going to risk the consequences of burning hydrocarbon fuels we would do well to capture as much of that ‘waste heat’ as possible and use it to supplement our energetic appetite. This is where the understanding and development of thermoelectric (TE) technology and devices holds promise. By either augmenting existing systems or as a standalone device for power generation applications, thermoelectric technology represents one avenue of improving our energy systems and can be one of many bricks in the foundation of a new sustainable energy economy. Thermoelectric devices are solid-state materials that can be used to convert heat absorbed at one end of a thermoelectric (TE) device into a useful electrical voltage.

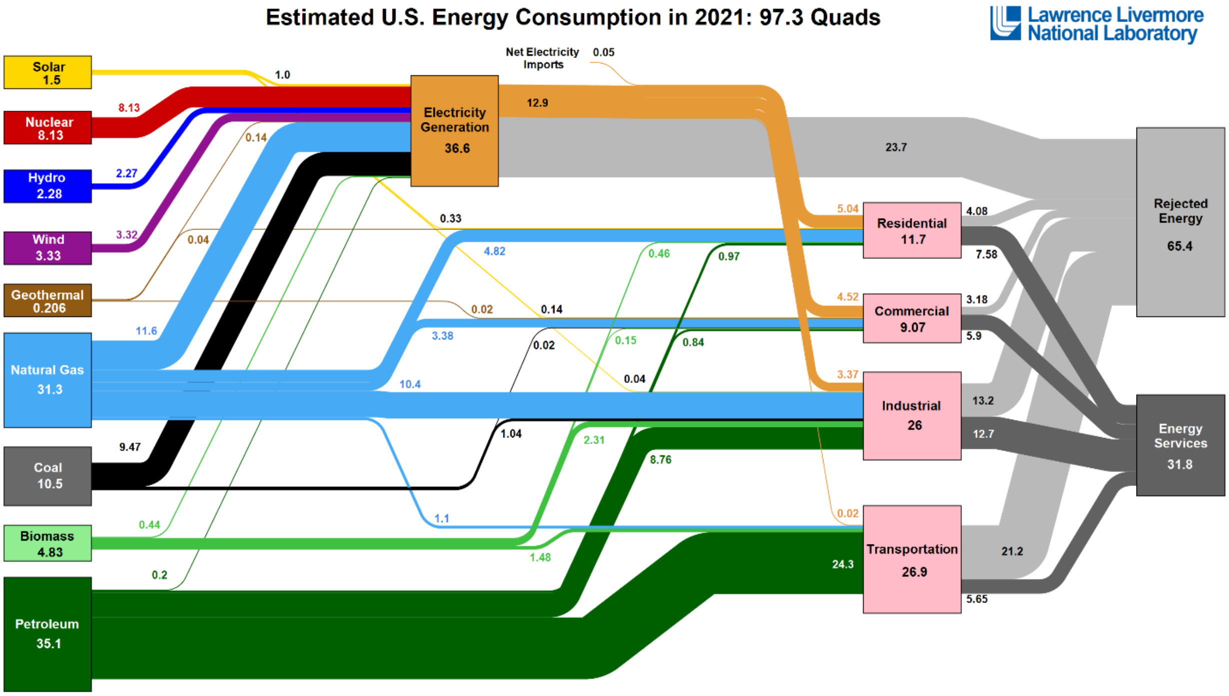

Figure 1.1: Energy sources and consumption estimates for the US in 2021. Note the large amounts of rejected energy from electricity generation and transportation sectors. Figure from reference [10]

1.2 Brief History of Thermoelectrics

The development of thermoelectrics started when the Seebeck effect was discovered by German physicist Johann Seebeck in the early 19th century, when he was experimenting on junctions and loops of dissimilar metals [11]. When one junction of the material loop was heated, he was able to detect a voltage difference at the opposite junction of the loop. The interdependence of electrical and thermal transport in solids was later further developed and formalized, and it was recognized that one can define a Seebeck coefficient for different materials. One can quantify the Seebeck coefficient of an arbitrary material with the following relation:

$$(S_1 - S_2) = \frac{\Delta V}{\Delta T} \tag{1.1}$$

Where S_2 is the Seebeck coefficient of a reference material, S_1 is the Seebeck coefficient of the material in question, and deltas V and T are the voltage and temperature differences respectively. One can determine reference values by measuring a junction where one material is superconducting and subsequently has a Seebeck coefficient of zero. Due to the two different charge carrier species, the Seebeck coefficient will be positive for “p-type” materials, and negative for “n-type” materials, which will be discussed in more detail in Chapter 2. All modern wire thermocouples operate under this principle, where two metals meet at the very tip of a thermocouple, and the voltage difference can easily be converted to a temperature reading.

After this discovery by Seebeck, the field continued to develop and later in the 19th century the French physicist Jean Peltier discovered the Peltier effect, whereby the ‘reverse’ of the Seebeck effect was demonstrated: that by passing a current through a junction of dissimilar metals, one can induce a temperature gradient at the junctions [12]. Today, devices known as

“Peltier coolers” operate using this effect. Later, William Thomson (later known as Lord Kelvin) contributed his insights and connected the two effects into what is known today as the Thompson Relations [13].

Following these discoveries, progress in the field of thermoelectrics was initially slow but picked up in the 20th century with the development of semiconductors and the physics that govern them. In the early 20th century, Edmund Altenkirch derived the theoretical efficiency of a thermoelectric generator and developed a key insight into thermoelectrics, the dimensionless figure of merit, *ZT* [14]. This figure of merit can be applied in the context of the Carnot efficiency to develop an understanding and upper bound on the efficiency of thermoelectric devices as a function of their material properties. This powerful formulation helps to guide the selection and development of promising thermoelectric materials:

$$\eta = \frac{T_h - T_c}{T_h} \frac{\sqrt{1+ZT}-1}{\sqrt{1+ZT} + T_c/T_h} \tag{1.2}$$

$$ZT = \frac{S^2\sigma}{\kappa} T \tag{1.3}$$

In equation 1.3, S is the Seebeck coefficient, σ is the electrical conductivity, κ is the thermal conductivity and T is the absolute temperature. In the 1930’s, Onsager showed that both the Seebeck and Peltier effects can be described as a natural consequence of the charge carrier transport [16]. Later in the 20th century, work by A.F. Ioffe popularized the notion of using semiconductors as base materials for developing thermoelectric devices (due to their high Seebeck coefficients) that led to some of the first commercial thermoelectric power generators and coolers [15]. With the powerful understanding provided by the formulation of *ZT* as the thermoelectric efficiency, semiconducting materials that had a high electrical conductivity while maintaining or reducing their thermal conductivity were identified as good candidates for further development. Work by Goldsmid on tellurides, especially Bi_2Te_3, led the field for many years and Bi_2Te_3 remains a competitive base material for thermoelectric applications [17].

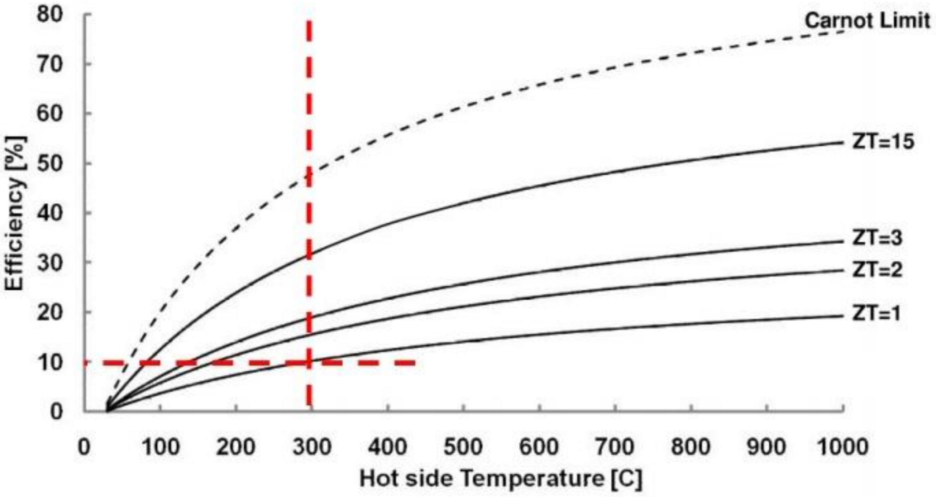

Figure 1.2: Carnot efficiencies for different ZT values. Note that at room temperature, a ZT of 1 is about 10% efficient.

In the latter half of the 20th century, thermoelectrics remained confined to niche applications as the field continued to develop materials with a high ZT over a broad temperature range. While not yet highly efficient, there are other aspects of thermoelectric power generation that make it attractive for different engineering applications. If a temperature gradient is maintained, the device will produce a usable voltage without any moving parts, which makes it extremely low maintenance. By stacking together many thermoelectric generators (TEG) together in series, relatively low voltages (typical thermoelectrics are on the order of microvolts per Kelvin temperature gradient) can be combined to produce a voltage of reasonable utility. With a long-lived heat source such as a radioactive material, a radioisotope thermoelectric generator (RTG) can function for years if not decades with no maintenance. One of the more successful applications of thermoelectric power generation has been in deep space applications, and the Voyager 1 and 2 probes were outfitted with RTGs that are still in operation some 40 years later [18]. Modern probes such as the Mars Rover *Curiosity* are outfitted with RTG's providing over 100W of power with several pounds of plutonium oxide as the long-lived heat source [19].

Modern approaches to developing thermoelectrics pursue a variety of avenues to improve the performance of these materials. A rather intuitive approach has been based around the "phonon-glass-electron-crystal' concept where a material is designed to scatter heat-carrying phonons while maintaining crystalline electronic performance [25-26]. Research in skutterudites and clathrate compounds have made use of so-called "rattlers" where a weakly-bonded atom absorbs phonons while confined to a "cage" in the crystal structure. Other routes have been to reduce the thermal conductivity to the lowest possible value through nanostructuring, complex crystal structures, quantum confinement, and/or maximizing anharmonicity in the crystal lattice [21-26,29-30]. One of the more exciting results of the last few years has been the development of ultralow thermal conductivity in single crystals of SnSe [20,27,31].

1.3 Motivation for GeTe and SnTe

Many tellurides were identified as good candidates for thermoelectric materials from the earliest days of the development of the field. In addition to Bi_2Te_3, PbTe, GeTe, and SnTe were identified as good candidates and an alloy of GeTe with silver and antimony called TAGS-85 was used in the Voyager probes [28]. This class of materials often have relatively high ZT values, maximizing at about 0.5-1.0, and are narrow band-gap semiconductors with high amount of symmetry in their crystal structure. They have useful thermal properties in that this class of materials has a high mass difference between the atoms, which reduces their thermal conductivity as well as useful and tunable electronic properties such as a degenerate band structure and large charge carrier effective masses. As such, they have been the subject of much interest in the development of thermoelectrics with a variety of strategies for optimizing the ZT performance [32-75,86,105-117]. There is an interplay between the competing thermal and electronic properties due to the contraindication of the material carrier concentration, and so finding the ‘sweet spot’ for an optimized carrier concentration is different in every material to maximize the ZT value (below in Figure 1.3, from reference [21]). The dependence of the variables in ZT on the carrier concentration will be further discussed in Chapter 2.

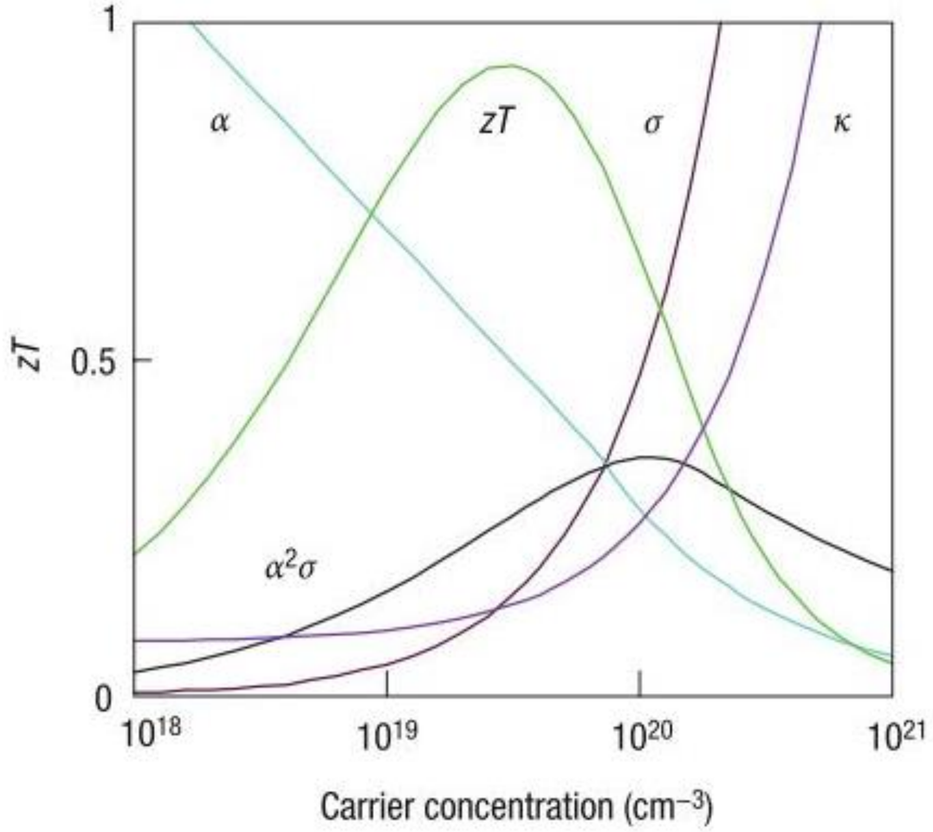

Figure 1.3: From [21], a figure showing the contraindication of the material properties as a function of carrier concentration versus ZT value. Here, α is the Seebeck coefficient, , *κ* is the thermal conductivity, and *σ* is the electrical conductivity.

While PbTe is recognized as a high performing thermoelectric material, there are other drawbacks to consider. Lead is widely recognized as a toxic material, and so research has been motivated to replace this toxic Pb with Ge or Sn. By replacing Pb, we can strive to maintain the high performance of this class of materials but without the toxicity or price. GeTe has been identified as the highest performer in terms of the electronic component, or power factor S^2s, and has been the subject of many studies [32-50]. SnTe has also been studied, both pristine and containing a variety of dopants, and has nominally better thermal properties in addition to Sn being a less expensive element than Ge [51-65]. In addition, both GeTe and SnTe exhibit a high-temperature cubic phase (space group Fm-3m), and a low-temperature phase that is rhombohedral (space group R3m) with the structural phase transformation occurring at 670K for GeTe and 97K for SnTe. It is also known that these materials form a complete solid solution, that substituting Ge for Sn at any concentration will not result in any line compounds [66]. By substituting Sn for Ge, the transition temperature is a tunable property governed by the amount substituted [67]. While there have been a number of studies on this solid solution [68-75], there is a relative dearth of information about the thermoelectric properties of polycrystalline samples, which this study aims to remedy. By being able to continuously vary the Sn concentration on the Ge site, we can quantify the effect of these features and observe how changes in the crystal structures affects the fundamental thermoelectric properties.

CHAPTER 2 PHYSICS OF THERMOELECTRICS

The study of thermoelectric materials and their performance lies firmly in the domain of solid-state physics and more specifically in the application of the physics of semiconductors. Thermoelectric materials can be understood through the fundamental material properties that govern the transport of charge carriers and phonons through a material. The electrical phenomena of interest are primarily the behavior of the electrical conductivity (σ) as well as the Seebeck coefficient (S), while the thermal behavior of a material can be understood through the thermal conductivity (κ). These variables, along with the temperature of a system (T) are used in conjunction to determine the efficiency of a thermoelectric material through the aforementioned dimensionless figure of merit ZT (equation 1.3). Resting on theoretical ground that has been stable for some time, the additional complexities of real materials and their performance make the computational prediction of these properties difficult. Specifically, the fact that many thermoelectric materials are polycrystalline and have variable grain sizes and defects makes a computational determination of ZT for a material difficult. Nevertheless, it is important to elucidate the underlying theoretical behavior in order to understand the most important concepts and parameters that govern the evaluation of thermoelectric materials as well as understanding the results and trends that emerge from the results presented in further chapters.

2.1 Electrical Conductivity

Electrical conductivity, σ, is defined as the ability of a material to conduct electric current. It is a measure of how well the material allows the flow of electrons in response to an applied electric field. If we choose to consider the Drude model, we can begin with some assumptions that there exist charged particles in a material, they freely move in response to a force generated by an external electric field, and they largely do not interact with each other. The quantification of conduction, the conductivity, can be explained by the frequency of charge carrier collisions on lattice sites, which limit the flow of charge carriers through a material. While simple on its face, the Drude model is a powerful conceptual framework from which we can closely approximate much of the behavior of metals, and to some extent semiconductors as well. For the latter case we know well that there are two charge carrier species, electrons and holes, but for the sake of brevity we take the perspective of electrons as charge carriers knowing the behavior for holes is similar.

Fundamentally, the formulation of σ can be traced back to simple concepts such as Ohm's Law and Newton's second law. Ohm's law states that the current (I) flowing is proportional to the voltage drop (V) across a material by the relation V= IR where (R), the resistance, depends on the material and its dimensions (length L and cross section A) but is independent of the applied voltage or current (equation 2.3). In a hypothetical resistor, the voltage drop across length L can be expressed as $V = E * L$, with E being the external electric field. If we consider the current density $j = I/A$, we can understand a relation between the current density j, electrical field E, and a material parameter ρ, which is the resistivity of a material and the inverse of the conductivity [76].

$$V = I\,R \tag{2.1}$$

$$j = \frac{I}{A}, I = A \cdot j \tag{2.2}$$

$$R = \rho\frac{L}{A} \tag{2.3}$$

$$E\,L = \rho\frac{L}{A} \cdot (A\,j) \tag{2.4}$$

$$E = \rho \cdot j \tag{2.5}$$

In the perspective of Drude, we can then imagine that the average velocity of charge carriers, v_{avg}, will be in the same direction through the material. We must also consider the number of charge carriers in a given volume that all equally contribute to the current density j, so we can rewrite the current density j as a product of this velocity, the number of charge carriers n, and the magnitude of an individual charge e.

$$j = -n\,e\,v_{avg} \tag{2.6}$$

Here the negative sign arises due to the fact that by convention j is in the direction of the flow of positive charge. To combine these terms we can consider an application of Newton's second law. If there is no external field, the average velocity of the charge carriers is zero because they are randomly oriented. When an external field is applied, the charge carriers accelerate in the direction of the current density j until they collide with a lattice site. Then, we can assume that the direction of the charge carrier after the collision is random, and thus v_0 does not contribute to the average velocity.

$$F = ma, F = eE \tag{2.7}$$

$$a = \frac{F}{m} = \frac{eE}{m} \tag{2.8}$$

$$v(t) = v_0 + at = v_0 + \frac{eE}{m}t \tag{2.9}$$

$$v_{avg} = \frac{e\,E}{m}t \tag{2.10}$$

By considering the average velocity v_{avg} and the average time between collisions as τ, we can replace the expression for v in our definition of $\boldsymbol{j}$ to have an expression for the current density as a function of the electric field, where:

$$j = n\,e\left(\frac{eE}{m}t\right) = \left(\frac{ne^2\tau}{m*}\right)E \tag{2.11}$$

$$j = \frac{n\,e^2\,\tau}{m*}\,E \tag{2.12}$$

So that we can express the proportionally value relation between electric field and current density as the electric resistivity as defined from our expression for the material resistivity $J = \sigma * E$, where $\sigma = 1/\rho$, *and* $\sigma = \frac{n\,e^2\tau}{m*}$, where σ is the electrical conductivity, and the electrical resistivity is its inverse.

$$\sigma = \frac{n\,e^2\tau}{m*} \tag{2.13}$$

One often sees the electrical conductivity is expressed as $\sigma = n\,e\,\mu$, where μ is the “electronic mobility” because it captures two essential parameters: the scattering relaxation time τ as well as the charge carrier mass *m*. If our charges are instead moving in the conduction band of a semiconductor, the behavior of this mass is more properly understood as m*, or the *effective mass*, as the curvature of electronic bands affects the effective mass of charge carriers [76].

$$\mu = \frac{e\,\tau}{m*} \ , \ \sigma = \frac{n\,e^2\,\tau}{m*} \qquad (2.14)$$

Of course, this result is recovered for a crystalline metal, and is incomplete without additional discussion of the function of these parameters as a function of temperature as well as a discussion of the band structure of semiconductors, which will also detail the various contributions to the scattering time τ as well as the relation between band structure and $m*$.

2.2 Carrier Concentration and Mobility

While in metals we can use the semiclassical model to describe the overall themes regarding the behavior of the transport of charge carriers, we need to refine our understanding when the material in question is semiconducting. In particular, the carrier concentration cannot be simply taken as a constant, but in fact depends on many additional factors. Specifically, semiconductors do not have the same number of allowed energy states at any given energy, but have a variable density of allowed energy states, known as the density of states (DOS). More critically, semiconductors exhibit a ‘gap’ in the allowed energy states for charge carriers, between the conduction band and the valence band (see Figure 2.1 below). Another important concept is the Fermi level, that is the energy level for a given charge carrier in equilibrium that has a 50% chance of being occupied. For metals the Fermi level is within the conduction band, and when carriers gain energy from an external field, they easily occupy higher energy states allowed by the unfilled states in the conduction band. For semiconductors the Fermi level is within the gap between allowed energy bands, and so a more detailed description is required for understanding the behavior of these materials. If the gap is wide enough, carriers are unable to gain enough energy to cross the gap and conduct electricity and therefore exhibit no conduction at all; these are referred to as insulating materials.

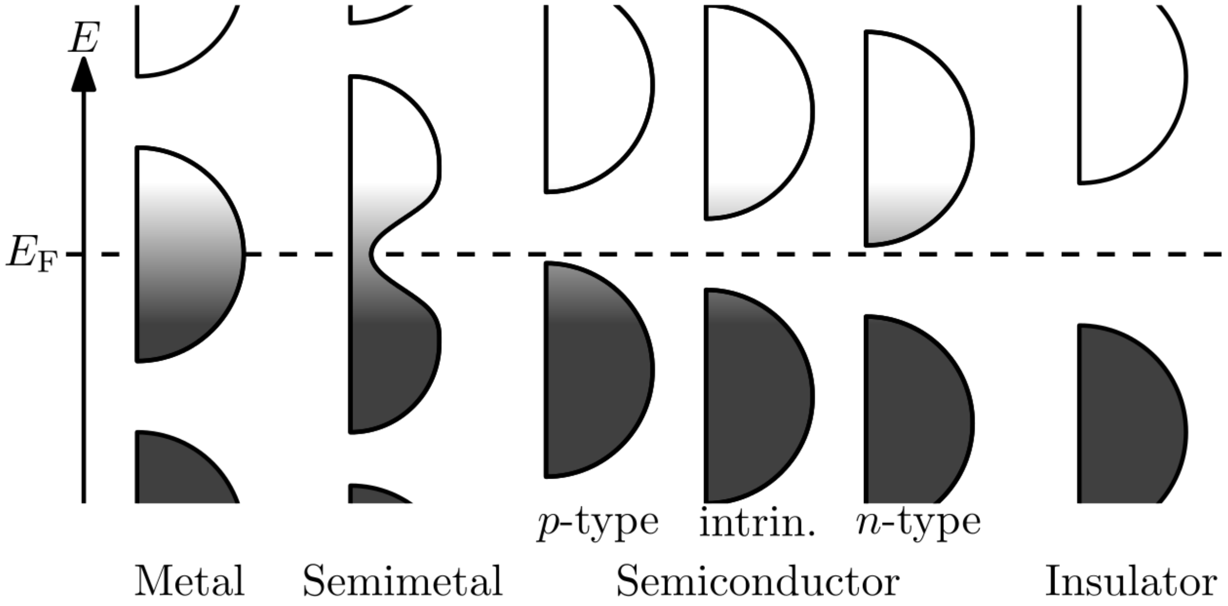

Figure 2.1: Illustration of electronic bands for metals, insulators, and semiconductors. Note the gap in semiconductors, and the distance between the band edge and the Fermi level (E_F) for p-type versus n-type semiconductors. *Image from* *https://en.wikipedia.org/wiki/Valence_and_conduction_bands*

Using the powerful formulation provided by Fermi-Dirac statistics as well as the density of states formulation we can express the carrier concentration:

$$n = \int_0^{\infty} f(E)g(E)dE \tag{2.15}$$

Where *f(E)* is the Fermi-Dirac distribution function and g(E) is the density of states for a free electron:

$$f(E) = \left(1 + e^{\frac{E-E_F}{k_b T}}\right)^{-1} \tag{2.16}$$

$$g(E) = \frac{\sqrt{2}m{*}^{3/2}}{\hbar^3\,\pi^2}\sqrt{2E} \tag{2.17}$$

Where *m** is the effective mass, *E* is the energy above the conduction band edge, E_f is the Fermi energy, and *T* is the temperature. If we then combine these equations, we can then recover the terms that depend on the effective mass and energy separately:

$$n = \frac{m*^{3/2}}{\hbar^3\,\pi^2}\int_0^\infty \frac{\sqrt{2E}}{1+e^{\frac{E-E_F}{k_bT}}}dE \tag{2.18}$$

$$n = N_c\,\frac{2}{\sqrt{\pi}}F_{1/2}\left(\frac{E_F}{k_bT}\right) \tag{2.19}$$

$$N_c = 2\,\left(\frac{2\pi m*k_bT}{\hbar^2}\right)^{3/2} \tag{2.20}$$

Where $F_{1/2}$ is the Fermi-Dirac integral, and N_c is the effective density of states at the conduction band edge. If $E_f = 0$, then we recover the result for the carrier concentration at the conduction band edge. However, for semiconductors this is often not the case, and we may make further simplifications for when the value of E_f inside the Fermi-Dirac integral is in fact not near the conduction band edge but rather several factors of k_bT into the gap. The previous integral formulation then takes the form [76]:

$$n \cong \frac{m*}{\hbar^3\pi^2}^{3/2}\,e^{\frac{-(E_C-E_F)}{k_bT}}\,\int_{Ec}^{\infty}e^{\frac{-(E-E_C)}{k_bT}}\,\sqrt{2E}dE \tag{2.21}$$

If we then take into further consideration the law of mass action, that the number of electrons (*n*) and holes (*p*) should be the same number (that is, each electron promoted out of the conduction band will leave behind a hole) and understanding that the energy term dominates the exponential relative to the temperature term inside the integrand, we can multiply the equation for *n* by itself to obtain the *intrinsic concentration* n_i. Taking the square root:

$$n = p, \quad n\cdot p = n_i^2 \tag{2.22}$$

$$n_i \approx \left(\frac{m*T}{\hbar^2\,2\pi}\right)^{3/2}\,e^{\frac{-(E_C-E_F)}{k_bT}} \tag{2.23}$$

Knowing that the Fermi level E_f is halfway between the valence and conduction bands (assuming equality of electron and hole effective masses), we can rewrite the above in terms of the Energy gap E_g and can clearly see how the intrinsic carrier concentration is a function of the temperature, effective mass, and the band gap energy.

$$n_i \approx \left(\frac{m{*}T}{\hbar^2\,2\pi}\right)^{3/2} e^{\frac{-E_g}{2k_bT}} \tag{2.24}$$

The above is a simplification of the effective masses of the two charge carrier species, but that is not necessarily the case. If the masses are not equal, the Fermi level will move in the direction of the band with the lower effective mass, but in most materials the ratio of masses is near unity. When this is the case, the Fermi level will still be within several k_bT of the center and our approach is still a useful formulation for understanding the most important parameters governing the carrier concentration. With this formulation, one can then consider the behavior of the electrical conductivity of a metal versus an intrinsic semiconductor. While a metal with a relatively stable carrier concentration will see its electrical conductivity decrease with temperature as the time between collisions τ decreases as thermally excited lattice sites cause more collisions, the semiconductor will see an increase in the electrical conductivity with temperature as the carrier concentration increases with temperature.

Armed with this understanding, one can also appreciate the utility of doping a semiconducting material. By substituting a small number of ‘impurity’ atoms into the lattice with a different valence than the base material, one can tune the carrier concentration of a material in the direction (up or down) to one’s choosing. Substituting atoms with a higher valence, which add electrons is referred to as an “n-type” dopant while atoms with a lower valence will be “p-type” dopants. These additional electrons or holes will then finely tune the total carrier concentration by adjusting the intrinsic concentration plus the number of ionized donor substitutes.

The overall performance of a doped intrinsic semiconductor as a function of temperature will depend on the particulars of the base material and doping concentration but follow a general pattern. At extremely low temperatures, there is not enough energy for any of the carriers from donors or intrinsically to bridge the band gap and the concentration is very low. As temperature increases, the carrier concentration will increase as dopant atoms become ionized and contribute to the total charge carrier concentration but will eventually saturate once all donors are ionized. Then the concentration will remain stable or 'saturated' until the temperature reaches a high enough level to promote intrinsic carriers to be excited across the band gap, and the carrier concentration again increases as a power law with temperature.

We return again to the standard formulation of the electrical conductivity $\sigma = n\, e\, \mu$, and now that we have a better understanding of what goes into n, we now examine the electron mobility μ and how it also contributes to our understanding of semiconducting behavior. Recall above our formulation for μ:

$$\mu = \frac{e\,\tau}{m*} \tag{2.25}$$

Where *t* is the average time between scattering events and *m** is the effective mass. There is a variety of processes that cause scattering events, and Matthiessen's rule [85] states that these scattering events can be added as reciprocals:

$$\frac{1}{\tau} = \frac{1}{\tau_{impurities}} + \frac{1}{\tau_{lattice}} + \frac{1}{\tau_{defects}} + \cdots \tag{2.26}$$

Where each τ^{-1} represents the scattering rate for impurities (carriers scattering off ionized atoms in a doped material), scattering from defects in the material, or interaction of carriers with phonons in the lattice (lattice). One can also consider the electronic mobility in the same formulation:

$$\frac{1}{\mu} = \frac{1}{\mu_{impurities}} + \frac{1}{\mu_{lattice}} + \frac{1}{\mu_{defects}} + \cdots \qquad (2.27)$$

For the impurity scattering, the contribution to the mobility will depend on both the concentration of impurities (N_i) as well as the effective mass and temperature in the following form [77-78]:

$$\mu_{impurities} \sim \frac{T^{3/2}}{N_i\sqrt{m*}} \qquad (2.28)$$

While the impurity scattering in general increases with temperature and decreases with concentration (as the available sites of scattering increase), the contribution from interaction with phonons has a different form [79]:

$$\mu_{lattice} \sim T^{-3/2}\, m*^{-5/2} \qquad (2.29)$$

When taking both into account, one can see the complex behavior of mobility and consequently conductivity as a function of temperature. For a doped semiconductor one very well might see a hump in the conductivity as a function of temperature as the carrier concentration approaches and then saturates the contribution from doped carrier saturates, followed by a dip as the mobility decreases with more interaction from phonons, before finally rising again with carrier concentration when intrinsic carriers are activated at a greater rate than the mobility decreases at higher temperatures. The location of the peaks and valleys in the conductivity temperature curve would depend on where the mobility peaks and behavior of the carrier concentration for each system.

At higher temperatures and high carrier concentrations when a material enters the intrinsic region (with n on the order of or exceeding ~10^{21} carriers per cubic centimeter), charge carriers scattering off of each other become an important mechanism to consider as well. At this stage, the mobility will decrease at a greater rate than the contribution of more carriers, and the more metallic behavior (where conductivity decreases with temperature) will be expected. For a highly doped semiconductor, this behavior will present itself at much lower temperatures, and the highly doped semiconductor will exhibit behavior more like a metal, and in general will decrease with temperature.

2.3 Seebeck Coefficient

The Seebeck effect is the fundamental basis of thermoelectric power generation, the conversion of heat into electricity. The Seebeck coefficient, also known as the thermopower, is a key parameter in describing the transport properties of thermoelectric materials. As stated in Chapter 1, we can initially simply express the Seebeck coefficient as the ratio of the measured voltage in a sample divided by the temperature gradient across the same sample:

$$S = -\frac{\Delta V}{\Delta T} = -\frac{(V_{Hot} - V_{Cold})}{(T_{Hot} - T_{Cold})} \tag{2.30}$$

If we understand that in a hypothetical bar of material, the T_{hot} end will have charge carriers that have a higher energy, and they will diffuse down to the cold end of the material. This buildup of charge on the cold side of the bar, an imbalance of charge, will generate an electric field and if the charge carriers are electrons will have a lower potential. Electrons being a negatively charged particle will then necessarily introduce a negative sign into the expression above. The result is that for n-type materials, whose dominant carrier type is electrons, the Seebeck coefficient will have a negative value while p-type materials will have a positive Seebeck coefficient. Typical Seebeck values for thermoelectric materials are expressed in microvolts-per-Kelvin or (µV/K) and a 'good' Seebeck value is on the order of 100 uV/K. (the best values, typical values?). At room temperature, pristine GeTe has a Seebeck coefficient of +34 uV/K, owing to many naturally occurring vacancies on the Ge site that make the dominant carrier species holes [36].

As the primary mechanism for the Seebeck effect is the movement and diffusion of charge carriers, the scattering of carriers, the effective mass, and the carrier concentration play an important role in the overall magnitude of the Seebeck coefficient. As such it has a complex form and is usually expressed in the form of Fermi-Dirac integrals while also considering the differing scattering mechanisms present in a material. It is usually expressed in the general form:

$$S = \pm\left(\frac{(s+2)F_{s+1}(\epsilon)}{(s+1)F_s(\epsilon)} - \epsilon\right) \tag{2.31}$$

Where F_x are Fermi integrals, ϵ is the Fermi energy (Ef/k_bT), and s is the carrier scattering parameter, which takes values s=0, ½, or 2 for phonon, defect, and ionic impurity scattering respectively. Real systems have a mixture of all these scattering rates, and so for a given temperature a mixture of scattering mechanisms contributes to the total. For metals and degenerate semiconductors this is usually expressed by the Pisarenko equation which is an empirical formula widely used in the field of thermoelectrics that expresses the magnitude as a function of the effective mass, carrier concentration and temperature:

$$S = \frac{8\pi^2k^2}{3eh^2}T\, m * \left(\frac{\pi}{3n}\right)^{2/3} \tag{2.32}$$

Knowing full well that the carrier concentration *n* is also itself a function of the effective mass, shown in the previous sections, it can be understood how interrelated these expressions are to both the effective mass of charge carriers as well as the carrier concentration. The challenge presented by developing thermoelectric materials lies in this contraindication of the carrier concentration: the conductivity benefits from a high carrier concentration while the Seebeck benefits from a lower carrier concentration. The result is that for a given material system there exists and optimal carrier concentration *n* that maximizes the value $S^2\sigma$. This term, the numerator and representing the electrical portion of *ZT*, is often called the *power factor*.

For some materials, both species of carrier concentration may diffuse down the length of a material. If this indeed happens, the Seebeck coefficient is resolved from the weighted average of the conductivities and Seebeck coefficients of each charge species [80]:

$$S \approx \frac{S_n\sigma_n + S_p\sigma_p}{\sigma_n + \sigma_p} \qquad (2.33)$$

For a more complete description of the transport behavior in the electronic perspective, we must also consider the thermal energy transported by charge carriers as they move through a material. The relationship between the thermal conductivity of charge carriers, called the *electronic thermal conductivity* or k_e is given by the Wiedemann-Franz law [82]:

$$\kappa_e = \sigma L T \qquad (2.34)$$

This empirical law is also based from Drude theory of electrical conductivity where σ is the electrical conductivity, T is temperature and L is the Lorenz number. Typically one can take the value of L as a constant, that is $L_0 = 2.44 \text{ x } 10^{-8}\ V^2K^{-2}$. However, this model usually fails for materials at high and low temperatures, as well as for highly doped semiconductors. This can lead to errors in calculating the contribution of the different parts of the thermal conductivity by overestimating the electronic portion κ_e by as much as 40%. Recent work by Kim, Gibbs and Snyder [81] show that for materials with a significant Seebeck coefficient, a better approximation for the Lorenz value as a function of the Seebeck coefficient is more appropriate:

$$L = 1.5\ \exp\left[-\frac{|S|}{116}\right] \cdot 10^{-8}\ W\Omega\, K^{-2} \qquad (2.35)$$

Where S is in the units of µV/K. This approximation has been the standard formulation in the thermoelectric community when a full characterization of the Lorenz number is not possible. This formulation has been shown to agree with experimental results in many TE materials including IV-VI semiconductors like PbTe and alloys of Si-Ge [81].

2.4 Thermal Conductivity

Thermal conductivity is a fundamental property of materials that describes their ability to conduct heat. It is defined as the rate at which heat flows through a material per unit area per unit temperature difference and is typically expressed in units of Watts per meter Kelvin (W/mK). The total thermal conductivity is the sum of the two different contributions from the different mechanisms for heat transfer in a material:

$$\kappa_{total} = \kappa_{electronic} + \kappa_{lattice} \tag{2.36}$$

Where $\kappa_{electronic}$ is the heat carried by the movement of charge carriers as detailed above, and $\kappa_{lattice}$ is the heat carried by the conduction of quantized wave packets, called phonons, as they travel through a material crystal lattice via vibrations. While the electronic behavior of materials is in the numerator of the figure of merit *ZT*, the denominator is only the thermal conductivity. Typically for semiconductors the electronic thermal conductivity makes a small overall contribution; thus a common approach to developing high efficiency thermoelectrics and maximizing *ZT* has focused on methods for reducing $\kappa_{lattice}$ to as small as possible without negatively impacting the electronic properties.

To understand the mechanism of heat transfer through a solid material, it is helpful to imagine a toy model that bears significant resemblance to real systems. Consider a periodic array of atoms in three dimensions as a network of interconnected masses and springs. When an atom is displaced from its lattice site, it exerts a force on its neighbors' atoms not dissimilar from the linear spring restoring force. As the initial atom comes back to rest at its initial lattice site, the displacement is taken up by neighboring atoms and the displacement can be understood as a wave that travels through the lattice. This wave packet is known as a phonon and is a quantized representation of the disturbance of atoms from their lattice sites. Any material above absolute zero will see atomic motion around the lattice sites, which can be understood in a macroscopic way as the temperature of the system. Starting at absolute zero with no atomic motion, as temperature is increased the lowest energy (lowest frequency) vibrational modes will be activated first, and as temperature goes higher more phonon modes with higher energy will be activated.

In many textbooks the formulation for $\kappa_{lattice}$ is relatively straightforward, but truly understanding the behavior of a material as a function of temperature calls for a more nuanced exposition of where this formulation comes from, particularly as a function of temperature. Much like how the electrical conductivity is a scalar relation between the current density and the electric field, thermal conductivity can be thought of as the scalar relation between the heat flow and the temperature gradient.

$$\kappa_{lattice} = \frac{1}{3} C\, v\, l \tag{2.37}$$

$$H = \kappa\, \Delta T \tag{2.38}$$

Where C is the volumetric heat capacity, v is the speed of sound, and l is the mean free path for the travel of phonons between scattering events. With H as the heat flow and T as the temperature gradient, thermal conductivity (in our case, just considering conduction from the lattice) is the scalar relating the two. A more careful consideration of H can be defined with help from the Boltzmann transport equations, which relate the heat flow to the number of phonons, the group velocity and the energy carried by these phonons ħω. We can then re-arrange the above to get κ by itself [83]:

$$H = \sum N(k)\hbar\omega(k)v(k) \tag{2.39}$$

$$\kappa = \frac{H}{\Delta T} = \frac{1}{\Delta T} \sum N(k) \hbar\omega(k) v(k) \qquad (2.40)$$

To further simplify, we can implement what is called the relaxation-time approximation, where the number of increased phonons per change in temperature in some relaxation time *t* is small, i.e. $\left(\frac{\partial N}{\partial T}\right) = \frac{N_0 - N}{\tau}$ and that $\left(\frac{\partial N}{\partial T}\right) \approx \frac{\partial N_0}{\partial T}$. This allows us to turn our sum into an integral up the highest activated phonon mode[83]:

$$\kappa = \frac{1}{3} \int_0^{\omega_{max}} \hbar\omega \; v^2 \, \tau \, \frac{\partial N_0}{\partial T} \, f(\omega) d\omega \qquad (2.41)$$

Where *f(ω)* is the phonon density of states with *τ* as our relaxation time. To inch ever closer to the simplified version we are used to seeing an insight of the Debye model assumes that the phonon dispersion curve is linear and we introduce a theoretical temperature called the Debye temperature. The Debye temperature is the temperature at which every available phonon mode in the system is activated, as at low temperatures only the lowest energy modes of vibration are activated. Due to the physical spacing of the lattice and finite number of atoms in a primitive cell, there is a maximum frequency that will meet the boundary conditions of a periodic crystal system. If we consider the highest frequency mode possible in a material system, it will have energy $k_b T_D$, where T_D is the Debye temperature, usually denoted as θ_D. Implementing this approach with the above expression, we can rewrite our integral in term of the Debye temperature and the scaled integrand $x = \hbar\omega / k_b T$.

$$\kappa = \frac{k_b}{2\pi^2 v} \left(\frac{k_b}{\hbar}\right)^3 T^3 \int_0^{\theta_D/T} \tau(x) \; \frac{x^4 e^x}{(e^x - 1)^2} dx \qquad (2.42)$$

If we now re-introduce the concept of the "mean free path" of a phonon (*l*= *vt*), we can then even further simplify the expression to separate out an expression for the heat capacity from the velocity and mean free path products:

$$\kappa = \frac{1}{3} v^2 \ T^3 \ \int_0^{\theta_D/T} \tau(x) \ \frac{x^4 e^x}{(e^x-1)^2} dx \tag{2.43}$$

$$\kappa = \frac{1}{3} v \ \int_0^{\theta_D/T} l(x) \ C(x) dx \ , \tag{2.44}$$

$$C(x) = \frac{3k_b}{2\pi^2 v^3} \left(\frac{k_b}{\hbar}\right)^3 \ T^3 \ \int_0^{\theta_D/T} \frac{x^4 e^x}{(e^x-1)^2} \ dx \tag{2.45}$$

Where we now have κ and *l* as functions of the dimensionless parameter *x*, and we recover something that looks very similar to the 'textbook' formulation of the thermal conductivity κ= *(1/3)c*v*l* (or if you like κ *= (1/3) C* v^2 ** τ) if we execute the integral and find values for *l* and *C*. We can then understand that the heat capacity as well as the mean free path are indeed functions of temperature and phonon frequency. This formulation allows us to consider the effects on these parameters separately and how this might show up in the behavior of materials. For low temperatures, it can be easily seen by the formulation of *C(x)* that the heat capacity follows a cubic dependence on *T*. Starting at a low value near absolute zero, the heat capacity rises rapidly with *T* until all the phonon modes have been activated and we approach the Debye temperature. After this, the high-temperature limits applied to the integral and the heat capacity becomes a constant value, which is described as the Dulong-Petit law where the heat capacity is a constant value based on the average molar mass of the material, i.e.:

$$C \propto T^3 \ , T \ll \theta_D \tag{2.46}$$

$$C = const. \ , \ const \sim \frac{3k_b N_A}{moles} \qquad T \gg \theta_D \tag{2.47}$$

For the present study, the materials in question have Debye temperatures well below room temperature as the reported Debye temperatures for GeTe and SnTe range from 180-200K and 160-180K respectively [86]. As such, with all measurements done in this study at or well above room temperature, we take the Dulong-Petit values as useful approximations for the heat capacity. This leads us back to the textbook form of the lattice thermal conductivity, with the explicit dependence on mean free path l ($l=v\,\tau$) or with the time between scattering events τ:

$$\kappa_{lattice} = (1/3)C\,v\,l = (1/3)C\,v^2\,\tau \qquad (2.48)$$

If we more closely consider the speed v or the speed of sound through the material, we can see that its value is closely related to the material density as well as the elasticity of the material.

$$v_{sound} = \sqrt{\frac{K}{d}} \qquad (2.49)$$

Where K is the coefficient of stiffness and d is the density. Elasticity is the ability of a material to reversibly deform up in response to stress. The coefficient of stiffness might be more appropriately expressed as a tensor K_{ij} to account for the number of possible directions the deformation might take. When the sample dimensions are much bigger than the grains of the material (as it is in the present study, with grain sizes on the order of tens of microns) the so-called *isotropic approximation* allows us to simplify the tensor. Fortunately for polycrystalline materials, the (generally) random orientation of grains in the sample as well as the symmetry of the crystal system reduce the components of K_{ij} to just two independent components K_{11} and K_{44}, which are more commonly referred to as C_{11} and C_{44}.

In principle, the speed of sound is the addition between the different component waves that are possible, the longitudinal and transverse modes, which are distinct:

$$v_{sound} = \left[\frac{1}{3}\left(\frac{1}{v_l^3} + \frac{2}{v_t^3}\right)\right]^{-\frac{1}{3}} \tag{2.50}$$

Borrowing some terminology from our friends in engineering, we can express the different moduli in terms of the above values in the elastic tensor, and more fully appreciate how these elastic tensor values affect the speed of sound. The shear modulus (G) is just C_{44}, while the bulk modulus $B = C_{11} - \frac{4}{3}C_{44}$. Applying to the two modes of sound propagation:

$$v_{longitdinal} = \sqrt{\frac{C_{11}}{d}} \tag{2.51}$$

$$v_{transverse} = \sqrt{\frac{C_{44}}{d}} \tag{2.52}$$

The mean free path, or closely related time between scattering events, is often the parameter of interest when developing materials with ever-lower thermal conductivity. Much like the Mattheisen's rule mentioned above, we can consider the contributions from different scattering mechanisms separately. These scattering mechanisms depend not only on the material composition and crystal structure, but also on macroscopic qualities such as the grain size, sample purity, and presence of vacancies in the lattice. In the present study, the most important scattering mechanisms present in these materials are impurity (point-defect) scattering, boundary scattering, and what is called phonon-phonon Umklapp scattering.

$$\frac{1}{\tau_{lattice}} = \frac{1}{\tau_{impurities}} + \frac{1}{\tau_{grains}} + \frac{1}{\tau_{Umklapp}} \tag{2.53}$$

Boundary scattering is related to the scattering of phonons off the boundaries of the sample itself, or rather the boundaries of neighboring grains in the material for a polycrystalline material.

Processing techniques in the synthesis phase of polycrystalline formation such as ball-milling or sintering parameters are the primary way of affecting this rate, by reducing the mean free path down to the size of an individual grain. As this primarily affects phonons with long wavelengths, it is more important for low-temperature behavior.

Impurity scattering refers to a variety of impurities that can be present in the material. These impurities generally are confined to a single atomic site (thus giving rise to the appellation point defect) and may be as small as the mass differences in different isotopes present in a material to as large as a vacancy on the lattice site. Work on several materials systems, including rutile [119] and diamond [87] irradiated with neutrons showed that lattice vacancies could play an important role in reducing thermal conductivity. For this study, we expect impurity scattering to be important for the materials in this solid solution, as GeTe has a relatively high rate of naturally occurring vacancies on the Ge site [36]. While SnTe also has naturally occurring vacancies, they occur at a lower rate than that of GeTe [51]. In each case, these impurities give rise to the observed carrier concentrations of the materials, as each vacancy results in a contribution to the p-type carrier concentration. The solid solution of GeTe and SnTe presents a type of impurity one might reasonably also call alloy scattering, in which Sn may be viewed as a point defect on the Ge site in GeTe, or alternatively Ge as a point defect on the Sn site in SnTe.

If we compare the thermal conductivity of pure Ge versus GeTe, the GeTe system will have a nominally lower thermal conductivity due to the larger average atomic mass of Ge (m= 72.64u) and Te (m=127.6u), as well as the lower Debye temperature of the binary compound. If we then further modify the system by alloying with Sn (m=118.71u) on the Ge site, then we will further disrupt the propagation of phonons and further suppress the thermal conductivity. Because the highest energy phonons approach the wavelength of the lattice spacing, these effects will be important at all temperatures, but especially at high temperatures. It was shown by Rayleigh that the relationship between scattering rates for sound was related strongly to the frequency [89]. Between the solid solution of GeTe and SnTe, we might expect the minimum conductivity due to impurity scattering to occur in the middle ($GeSnTe_2$), where the random assignment of Ge and Sn atoms provides for the maximum disorder in the lattice and provides the most amount of scattering [90]. Work by Klemens showed that the affect due to mass differences scaled as the square of mass differences [88]:

$$\frac{1}{\tau} \sim \left(\frac{\Delta M}{\mathrm{M}}\right)^2 \tag{2.54}$$

Umklapp scattering (from the German word *umklappen* “to turn over”, a phrase proposed by a student of Wolfgang Pauli, Rudolf Peierls) is a process by which two phonons scatter off of each other, and the resulting phonon vector lies outside the first Brillouin zone of the crystal, so when translated back into the original Brillouin zone, it points away from the vectors of the first two phonons. Studies by Glen Slack in the mid 20th century gave us a rough relationship between the temperature and the thermal conduction due to Umklapp processes at low temperature [91]:

$$\kappa_U \sim T\, e^{\frac{\theta_D}{2T}}, \qquad T \cdot 10 \; < \; \theta_D \tag{2.55}$$

At higher temperatures, the number of phonons continues to increase, and one would expect the phonon-phonon interactions to be more and more likely, which would strongly decrease the thermal conductivity as temperature increases. For higher temperatures, all the above processes contribute to the total thermal conductivity, and it has been shown experimentally that the general trend for thermal conductivity varies inversely with temperature, that is:

$$\kappa_{lattice} \sim T^{\,-1} \quad T \; \gg \; \theta_D \tag{2.56}$$

Taking the many above processes into account, Slack *et al* combined all these variables into a succinct expression for thermal conductivity to serve as a guide for selecting low (or high) thermal conductivity materials sufficiently above the Debye temperature [92]:

$$\kappa = c \frac{\overline{M}\,\theta_d V}{T\gamma^2 N^{2/3}} \tag{2.57}$$

Where M is the average atomic mass, θ is the Debye temperature, γ is the Grüneisen parameter, V is the volume per atom and N is the number of atoms per unit cell. This not only reflects the expected T^{-1} dependence, but also considers crystal system qualities such as the number of atoms per unit cell and their volume.

Of particular importance in this equation is the Grüneisen parameter. Physically this is associated with terms higher than quadratic in the potential energy relation for atomic motion – in other words, it is a measure of deviations from perfectly harmonic (Hooke's law) behavior. A perfectly harmonic lattice would have a Grüneisen parameter approaching zero, and an infinitely large lattice thermal conductivity. Of course, all solids possess some deviation from perfectly harmonic lattice vibrational spectra and thus have finite (non-zero) Grüneisen parameter. As can be inferred from Equation 2.58 above, a large Grüneisen parameter is a strong predictor of a low lattice thermal conductivity and recent work has been devoted to identifying and developing materials with these desirable properties for thermoelectric applications.

Macroscopically, the average Grüneisen parameter may be related to the coefficient of thermal expansion of a solid:

$$\gamma = \frac{\alpha B}{C_V d} \tag{2.58}$$

Where α is the thermal coefficient of expansion, B is the bulk modulus, C_V is the heat capacity at constant volume and the material density is d.

For a solid solution, alloy or defect scattering will have a varying effect as a function of the amount of substitution. Starting with the end members on each side at their respective pristine thermal conductivities (on the order of 5-10 W/mK) [35,51] as dopant is introduced the thermal conductivity will decrease due to the mass differences introduced into the lattice. This will continue until the conductivity as a function of substitution flattens or levels out at intermediate values of substitution. This shape, which one might reasonably call a "bathtub" shape is modeled by the following function:

$$\kappa_0 = \frac{\tan^{-1} x}{x} \tag{2.59}$$

Where *x* is the amount of dopant in the solid solution, i.e., the "*x*" in $\mathrm{GeTe}_{(1-x)}\,\mathrm{Sn}_{(x)}\,\mathrm{Te}$. This study will use this notation often in this context, taking "*x*" to be the fraction of Sn atoms alloyed onto the Ge lattice site. In Figure 2.2 below, an illustration of this shape is depicted from [93].

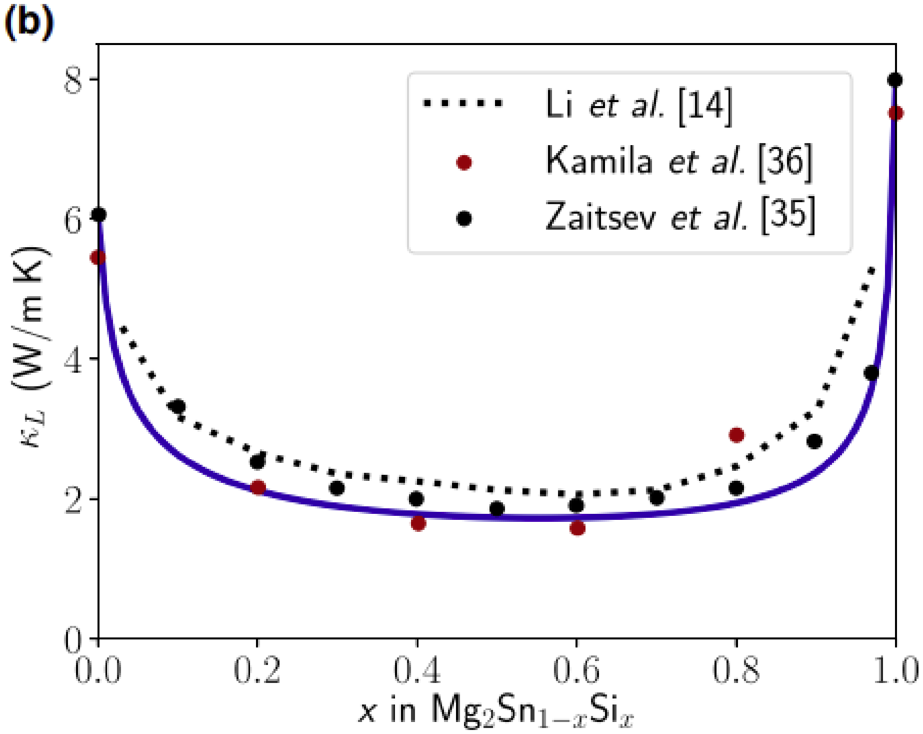

Figure 2.2: Demonstration of the "bathtub" shape due to alloy scattering in Magnesium Silicide alloys from [93]. Note the rapid drop-off in lattice thermal conductivity even at small dopant amounts.

2.5 Thermoelectric Figure of Merit

We return again to the dimensionless figure-of-merit *ZT* that demonstrates the importance of maximizing the electronic performance of a material while also limiting the thermal conductivity:

$$ZT = \frac{\sigma S^2}{\kappa_e + \kappa_l} \tag{2.60}$$

But as we can understand from above, there are also deeper parameters that underlie the complex interrelation between the above fundamental parameters that we could use to express *ZT* to use as a guide for identifying or designing promising thermoelectric materials:

$$ZT \propto \frac{m_*^2 \, \mu \, \gamma^2}{\overline{M} \, \theta_D V} \tag{2.61}$$

Where m^* is the effective mass, μ is the mobility, γ is the Grüneisen parameter, M is the average atomic mass, and θ is the Debye temperature. This makes a little more explicit how challenging developing high-*ZT* materials can be, as effective mass and mobility are inversely correlated. In addition, as mentioned above there exists an optimal carrier concentration for a given material that maximizes the electronic performance as well as the thermal conductivity, as the electronic portion of the thermal conductivity rises with electronic conductivity. An excellent and oft-repeated figure by Snyder *et al.* [21] in Figure 2.3 below demonstrates this graphically.

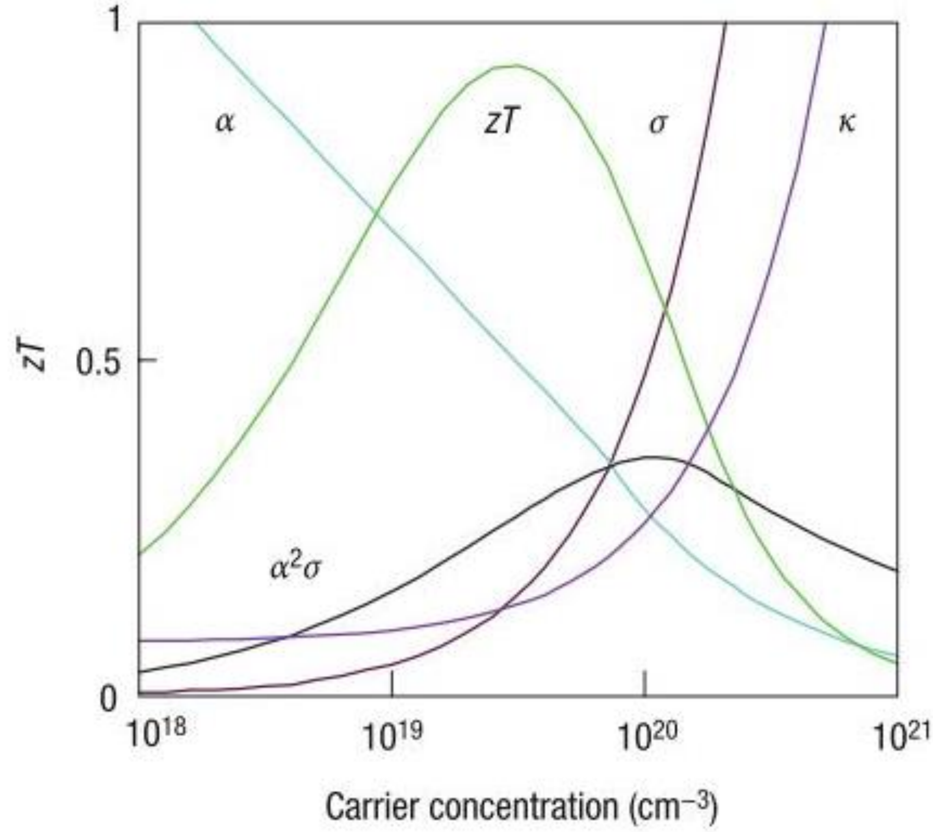

Figure 2.3: From [21], a figure showing the contraindication of the material properties as a function of carrier concentration versus ZT value. Here, α is the Seebeck coefficient, , κ is the thermal conductivity, and σ is the electrical conductivity.

CHAPTER 3 EXPERIMENTAL METHODS

All samples were synthesized via direct fusion as ingots from elements obtained from Alfa-Aesar in small pieces or powder with at least 99.999% purity (also described as 5N+). Stoichiometric amounts were separately weighed out on plastic trays and loaded into a quartz ampoule with an inner diameter of 10mm and a rounded bottom. These quartz ampoules were then transferred to a sealing station. At the sealing station, the ampoules were subjected to a vacuum of at least 1x10^{-5} Torr and sealed with an oxygen-methane torch.

Sealed ampoules were placed in Thermolite box furnaces and gradually heated to a maximum temperature of 950 °C to completely melt the elemental powders. Once at temperature, ampoules were soaked at 950 °C for at least 8 hours and then gradually cooled to room temperature. No ingots were annealed or quenched, to ensure that samples would not have high-temperature structures ‘frozen-in’. Once cooled to room temperature, the quartz ampoules were broken open and the resulting ingots were extracted, ranging from 4-8 grams per ingot. Due to the random nature of heating and cooling regarding specific crystallographic orientations, this synthesis procedure produces samples that are polycrystalline in nature. We did not see any long-range ordering of the domains in our samples, and any ordering would be upset by our powder processing techniques detailed below. A picture of a sealed ampoule and an extracted ingot is shown below in Figures 3.1 and 3.2.

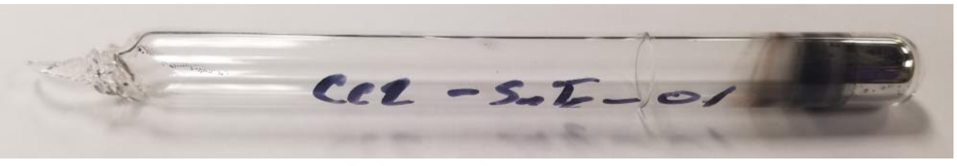

Figure 3.1: A sealed ampoule containing a SnTe ingot

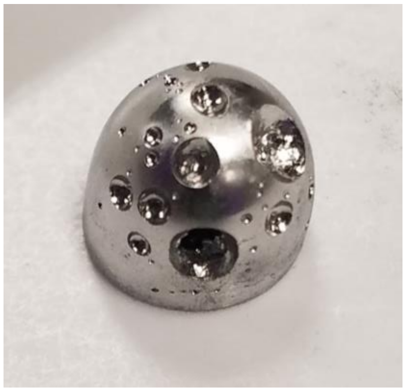

Figure 3.2: The bottom view of an extracted ingot of a Germanium-rich sample.

Many thermoelectric materials, including tellurides and especially materials undergoing a crystal phase transition, do not readily form high density ingots. Fresh ingots were porous and brittle, likely owing to large grain sizes formed during the slow cooling process. Large grain sizes are known to decrease yield strength and hardness, rendering samples mechanically weak. To address this and minimize the effects of porosity and low density, a procedure to grind ingots into fine powders before a consolidation procedure was developed.

3.1 Powder Processing and Sintering

Furnace fresh ingots were extracted from quartz ampoules manually and hand-ground in a mortar and pestle. To check sample purity, samples were subjected to x-ray diffraction. To further prepare samples for sintering in a Spark-Plasma-Sintering apparatus, samples were subjected to a high-energy ball mill with stainless steel media. Sample powders were loaded under an argon atmosphere in a stainless-steel jar with 4-6 stainless steel ball bearings and mixed in a SPEX MixerMill 8000D for five minutes. Initial samples were milled for longer times, but this additional milling was determined to be unnecessary and introduced additional mechanical stress on grains in the sample, evidenced by cracked and brittle samples as well as broader XRD peaks in excessively milled samples.

An attempt was made to circumvent the direct fusion synthesis process and synthesize powders by milling elemental powders in stoichiometric amounts, by mechanical alloying. Several end-members and solid-solution samples were attempted with ball-mill times upwards of three hours. When checked for purity via XRD, these samples produced powder that did not have sufficient sample purity with large contributions from unreacted elemental powder. This gave us renewed motivation to pursue synthesis via the traditional direct fusion synthesis method.

After milling for five minutes, sample powder was manually extracted from the stainless-steel jar and again subjected to x-ray diffraction. After this, sample powder was collected into a glass vial for preparation for solidification. Sample densification and solidification were achieved using a water-cooled Dr. Sinter Spark-Plasma-Sinter 211LX (SPS). Our process was to load powder into a 10mm diameter graphite die, with graphite foil spacers above and below 10mm graphite punches. Up to 3 grams of powder could fit in a single die, but typically were loaded with about half that amount of powder. The loaded die would then be loaded into the SPS chamber and brought under vacuum. The SPS subjects the die to a large uniaxial pressure and then utilizes an AC current to generate joule heating between the top and bottom electrodes. With a thermocouple connected directly to the die, the SPS has precise temperature and pressure controls that are monitored in a data acquisition computer.

After reviewing available literature SPS synthesis parameters a temperature profile for the SPS was developed. A similar temperature profile, depicted in Figure 3.3, was used for all the powder samples to compress powder samples into a cylinder with >95% theoretical density. The profile was chosen through process optimization to consistently yield samples that were durable and dense: up to 300C in five minutes, up to 400C in another five minutes, and then holding at 400C for 20 minutes, before linearly cooling down to room temperature over 30 minutes, with the first three steps at 40 MPa of pressure (near the maximum pressure that the graphite die could withstand). Upon linear cooling pressure was gradually reduced from 40MPa to prevent cracking in the samples. Samples were extracted from the SPS and dies at room temperature, sanded on both sides to remove the graphite foil, and again subjected to x-ray diffraction.

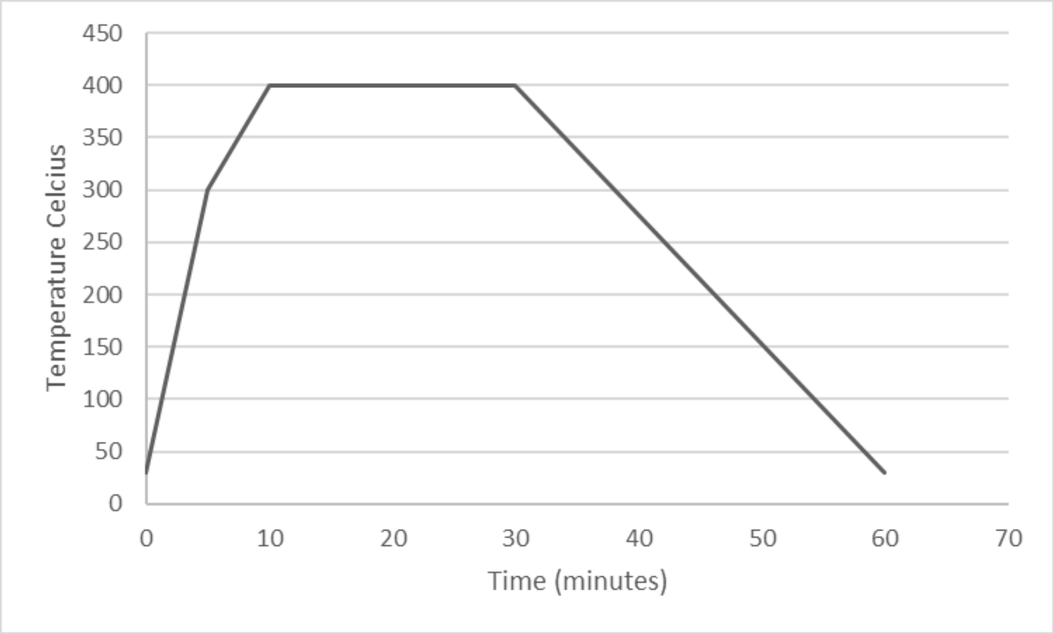

Figure 3.3: Spark plasma sintering temperature profile used for all samples.

Sample density is a key parameter in evaluating if the sample in question achieved sufficient consolidation. After SPS, all samples had their density measured in two ways: geometrically via a scale and calipers, and via the Archimedes method by submerging in ethanol. Sample density was compared to theoretical desired values, either literature values for end-members GeTe and SnTe or that derived from a linear rule of mixtures for solid-solution samples. Details for sample density can be found in the Appendix. After process optimization with the SPS, only samples of at least 95% theoretical density were selected for further characterization.

Figure 3.4: An image of a series of samples after SPS and polishing.

3.2 Phase purity and compositional analysis

At many of the steps of the synthesis process, X-ray diffraction (XRD) analysis was used to analyze the phase purity of the samples and evaluate any change in microstructure. X-ray diffraction is an analysis technique that utilizes the periodic nature of crystal lattices to generate an XRD pattern that reflects the constructive interference of scattered x-rays incident on different planes of atoms in the lattice. The crystal structure as well as lattice parameters can be extracted from an XRD pattern, so it is a powerful, fast, and non-destructive technique for evaluating both the phase purity of metallic powders and samples and other crystallographic properties.

Crystal lattice spacings are on the order of angstroms, so therefore for optical scattering to take place the incident light must have a wavelength on the same length scale. The condition for evenly spaced atoms to scatter light constructively is given by Bragg's Law:

$$n\lambda = 2d\, sin\theta \tag{3.1}$$

Where n is an integer, λ is the wavelength of incident light, d is the lattice spacing, and θ is the angle of the incident rays onto the sample. With this understanding, one can generate a theoretical XRD pattern for any given material based simply on its crystal structure and lattice spacing. Powder x-ray diffraction is a well-established technique, so one can make use of large libraries of powder diffraction files (PDFs) and software techniques by which to analyze and compare XRD patterns generated from samples. By analyzing and indexing each peak according to the Miller crystallographic indices, one can calculate lattice parameters.

Being a cubic material at room temperature, SnTe has many symmetries in its crystal structure, and all those symmetric signals combine to form the largest characteristic peak at just above 30 degrees 2θ. Because our synthesis method produced polycrystalline samples, we did not consider the relative orientations of our sample compared to the XRD, since the random orientation of our samples would produce enough grains to reflect all the lattice planes needed to render a full XRD spectrum. Any extra peaks can be compared to known peak profiles of varied materials to characterize the phase purity of the samples. Using our synthesis process, we were able to create samples that showed phase purity within the detection limit of our XRD analysis. When present, the most common impurity was unreacted elemental tellurium.

During synthesis, sample XRD was performed at room temperature on a Rigaku MiniFlex-II using Cu-Kα radiation powered at 30 kV at 15 mA, with the radiation λ = 1.54 Å. Samples were placed on glass slides and leveled to be even with the glass slide surface. For a select few samples while equipment was available, XRD was also taken at elevated temperatures. For samples x=0.25 and x=0.50, high-temperature XRD (HT-XRD) was taken every twenty degrees up to 200C to characterize the temperature of the phase transition. Room temperature and HT-XRD was performed under vacuum on a Rigaku Smartlab XRD, with the same type of radiation. Analysis of raw data was done in either the Jade 9 or PDXL2 software packages for the two different XRD machines, respectively.

3.3 Resonant Ultrasound Spectroscopy

Resonant Ultrasound Spectroscopy is a technique to measure the elastic constants of a material by matching the resonant frequencies of a sample to a predicted set of frequencies given a sample's dimensions, density, crystal structure and elastic constants [94-98,112]. Resonant Ultrasound Spectroscopy (RUS) was performed on samples to characterize their elastic constants. Being non-destructive, this analysis technique allowed us to measure the elastic response for cylindrical samples created in our SPS dies. Precise sample geometry and density are critical factors for this measurement, as they may shift or disrupt resonant peaks, so with polishing we were able to prepare RUS samples that were free of chips, cracks, defects, and geometrical deformations. Using an iterative process, we continuously adjusted C_{11} and C_{44} values until the predicted resonances closely matched the observed peak positions [96]. All room-temperature measurements were formed on a portable stage from Alamo Creek Engineering (ACE) [99].

The RUS system enables us to calculate the elastic constants of a material by placing the sample between a pair of piezoelectric transducers (pictured below in Figure 3.5). One transducer sweeps a range of vibrational frequencies while the other transducer monitors the sample for resonance peaks. When the first transducer sweeps through a frequency that matches one of the many fundamental resonant frequencies of the material, the sample vibrates, and this movement is picked up by the receiving transducer. One can then construct a spectrum of peak locations with their frequencies with the aid of software. This study used the "Resonance Spectrometer" software package, with a representative image in Figure 3.6 below [100-101]. The data for these resonance peaks can then be compared to a predicted resonance pattern for a given sample's geometry, density, crystal system and elastic constants. The differences between observed and predicted peaks can then be adjusted iteratively to change the C11 and C44 values in a way that minimizes the differences between the observed and predicted peak locations. This study used the Cyl.exe software to calculate elastic moduli [94].

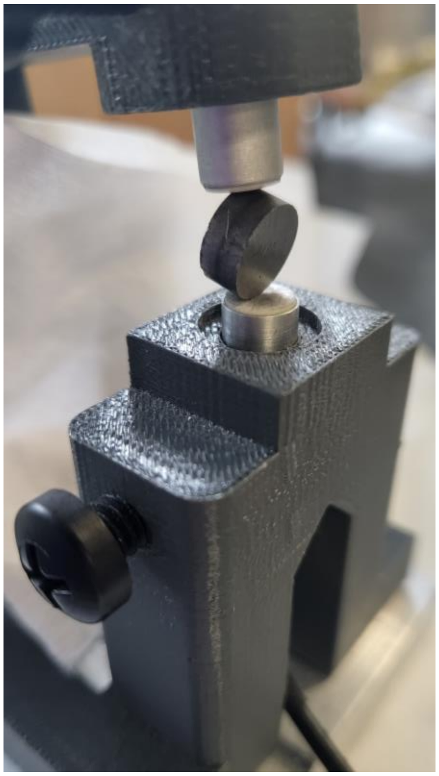

Figure 3.5: A picture of the RUS stage with a cylindrical sample mounted between the top and bottom transducers.

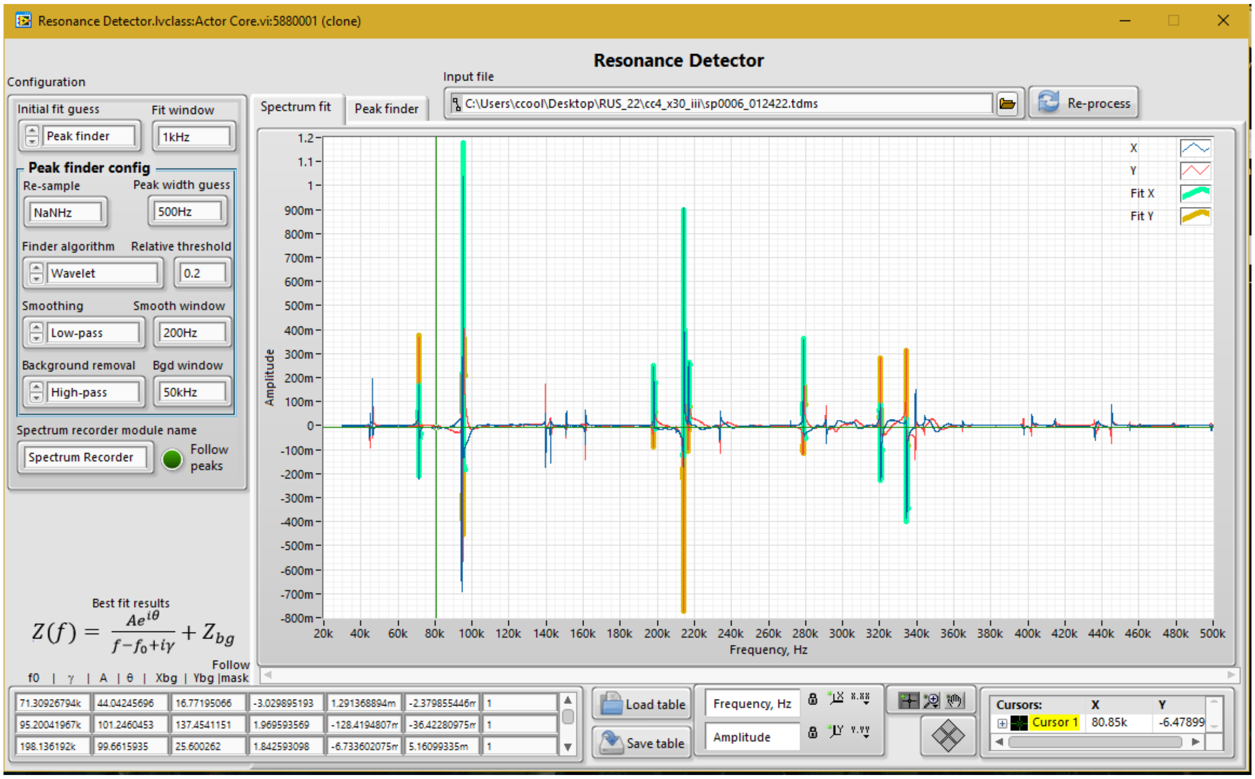

Resonance Detector.lvclass:Actor Core.vi:5880001 (clone)

Resonance Detector

Configuration

Initial fit guess: Peak finder
Fit window: 1kHz

Peak finder config

Re-sample: NaNHz
Peak width guess: 500Hz
Finder algorithm: Wavelet
Relative threshold: 0.2
Smoothing: Low-pass
Smooth window: 200Hz
Background removal: High-pass
Bgd window: 50kHz

Spectrum recorder module name: Spectrum Recorder
● Follow peaks

Input file: C:\Users\ccool\Desktop\RUS_22\cc4_x30_iii\sp0006_012422.tdms

Best fit results

$$Z(f) = \frac{Ae^{i\theta}}{f-f_0+i\gamma} + Z_{bg}$$

f0	γ	A	θ	Xbg	Ybg	Follow mask
71.30926794k	44.04245696	16.77195066	-3.029895193	1.291368894m	-2.379855446m	1
95.20041967k	101.2460453	137.4541151	1.969593569	-128.4194807m	-36.42280975m	1
198.136192k	99.6615935	25.600262	1.842593098	-6.733602075m	5.16099335m	1

Cursors:	X	Y
Cursor 1	80.85k	-6.47899

Figure 3.6: An image capture of the “Resonance Spectrometer” software used for RUS analysis.

3.5 Laser Flash Analysis

Thermal diffusivity measurements were performed on all samples were performed by Laser-Flash Analysis (LFA). LFA directly measures the thermal diffusivity of a material by monitoring the radiation on the back surface of a sample over time after it has been briefly illuminated by a pulse of laser energy on its front surface. All measurements were performed on a Netzsche LFA 467 utilizing a pyroceram reference material. The nature of the LFA measurement requires samples in the form of thin disks. To achieve this, samples prepared via the SPS process were polished and thinned with fine-grit sandpaper to be less than 2mm thick, taking care to ensure that both sides of the sample were parallel to each other. After polishing, samples were coated with a thin layer of graphite spray to ensure good absorption of the thermal energy of the laser and minimize laser reflections off the sample. Four samples were prepared at a time and measured using a carousel mechanism every 10 °C from 50 °C first heating up to 450 °C and back down to room temperature (see Figure 3.7). The LFA would take three ‘shots’ per temperature step and report the individual values as well as averages in the output data file.

Using the known relationship (Equation 3.2) between thermal diffusivity (α), density (d), and heat capacity (C_p), we calculated total thermal conductivity values from the experimental diffusivity values. Density values were obtained again geometrically from weighing the sample and measuring with calipers to ensure consistent density values. The heat capacity constant for all samples was determined according to the Dulong-Petit relationship, where the value can be determined using the known molar masses of the stochiometric elements of the sample [118]. See the Appendix for details on the calculations of heat capacity.

$$\kappa_{total} = \alpha \cdot d \cdot C_p \tag{3.2}$$

Figure 3.7: An image of four LFA samples in the 4-sample carousel inside the LFA.

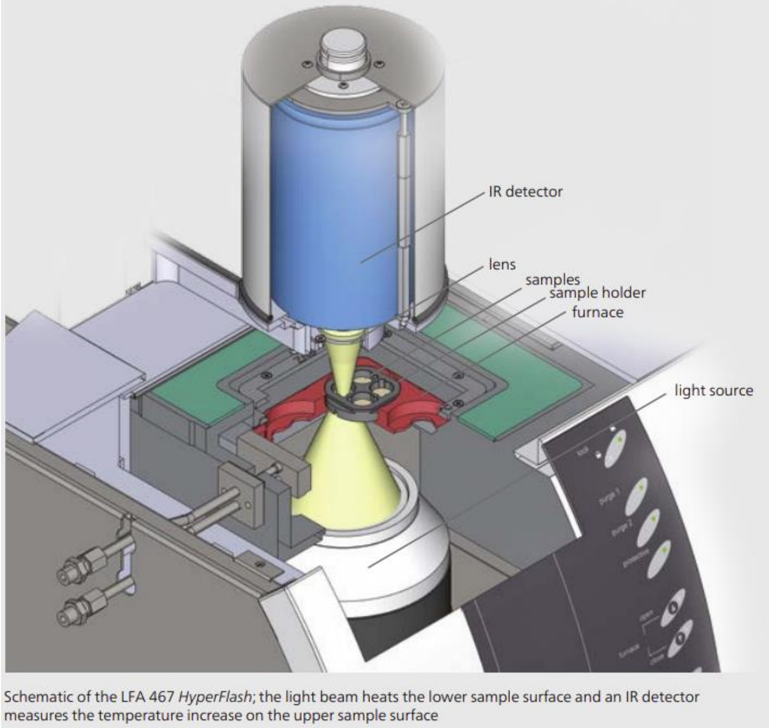

Schematic of the LFA 467 *HyperFlash*; the light beam heats the lower sample surface and an IR detector measures the temperature increase on the upper sample surface

Figure 3.8: A schematic of the LFA equipment Image from Netzsch product website [102].

3.6 Electrical resistivity and Seebeck coefficient

To characterize the material's electrical resistance and Seebeck coefficient, samples were characterized in an Ulvac-ZEM3 instrument (ZEM) up to 500 °C. This measurement requires the sample to be in the form of a rectangular prism. To this end, the cylindrical sample was cut with a low-speed diamond saw and sanded down to be a rectangular prism and its dimensions measured carefully with calipers. The sample was then carefully mounted into the ZEM between two electrodes and gently tightened into place. Then two spring-loaded thermocouples were pressed against the sample at a separation distance measured by a camera mounted to the ZEM stage, before being covered with a radiation shield and sealed in a chamber under vacuum. The sample chamber was evacuated and purged with Helium several times before being backfilled with a small amount high-purity Helium. A schematic of the sample mounted in the ZEM is displayed below in Figure 3.9.

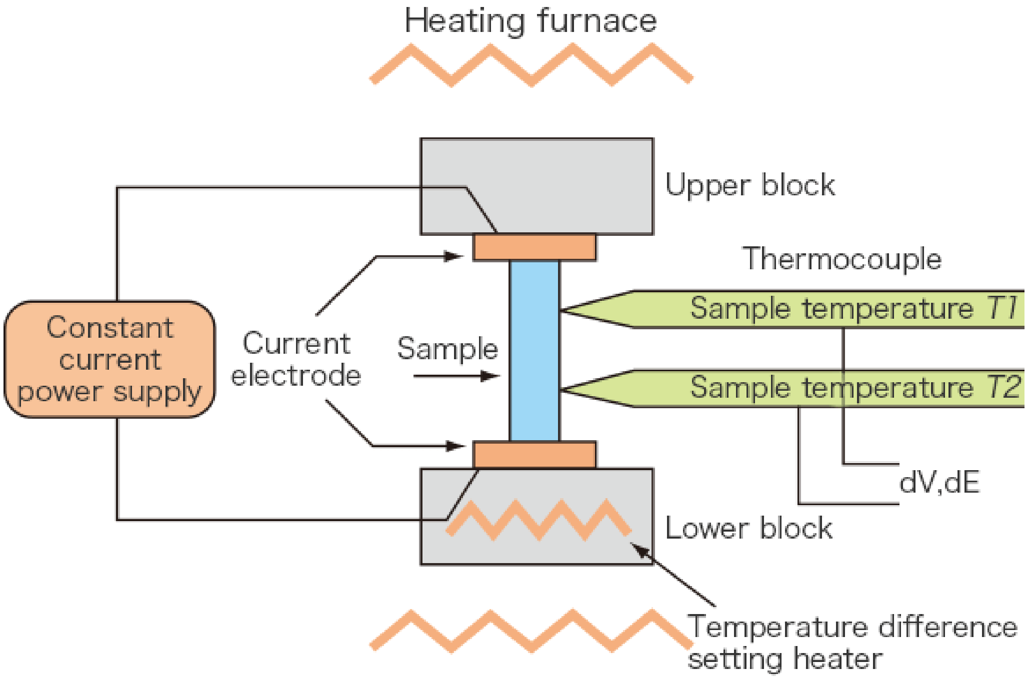

Figure 3.9: A schematic of how ZEM operates [103].

The ZEM measures sample resistivity via the 4-point method, with the top and bottom electrodes serving as current contacts and one leg of each thermocouple as the voltage contacts. Samples were measured at room temperature before vacuuming to ensure a strong signal and good contact with the sample. To measure the Seebeck coefficient at every temperature step, the ZEM activates a heater encased in the lower electrode arm. This heater in turn generates a temperature gradient across the sample, monitored by the spring-loaded thermocouples. The Seebeck coefficient (below) is calculated by dividing the voltage difference between the thermocouple contacts by the temperature gradient value. Typical values for these materials are in the micro-volt per Kelvin range.

$$S = \frac{\Delta V}{\Delta T} \tag{3.3}$$

The ZEM measured sample resistivity and Seebeck coefficient three times per temperature step and reported average values per step on both heating and cooling. Temperature profiles were set so that a temperature difference of at least 1 degree Celsius was achieved between probe thermocouples. To further analyze the lattice and electronic contributions to the thermal conductivity, ZEM data was used in conjunction with the Wiedemann-Franz Law, where ρ is electrical resistivity, T is temperature and L is the Lorenz number [82].

$$\kappa_{electric} = \frac{L \cdot T}{\rho} \tag{3.4}$$

As detailed in Chapter 2 the Lorenz number can be treated as a constant in most metals, but for highly degenerate semiconductors where the Seebeck coefficient is significant an approximation commonly used for thermoelectrics is shown above in Equation 2.35 [81]. This approximation can be used for every data point we have a Seebeck coefficient for and enables a better calculation of the electronic contribution to the thermal conductivity. Taken together, the ZEM characterization lets us combine the data from the LFA to fully describe the thermal conductivity of the samples and their electronic and lattice contributions.

$$\kappa_{total} = \kappa_{electronic} + \kappa_{lattice} \tag{3.5}$$

3.7 Hall effect measurement

A select few samples were selected for further characterization with a room temperature Hall effect measurement of carrier concentration and carrier mobility. A Hall measurement makes use of the fact that electrons carry a magnetic moment and therefore their paths of motion will be deflected by magnetic fields [104]. By placing a sample in a large magnetic field on one axis and connecting the sample electronically to a current on an orthogonal axis, one can measure the carrier concentration of a sample from the voltage observed perpendicular to the previous two axis. This voltage generated by the external magnetic field, called the Hall Voltage (V_H), can then be used to calculate the carrier concentration from other sample parameters (see equations 3.6-3.8 below).

$$V_H = \frac{I_x B_z}{n\,e\,t} \tag{3.6}$$

$$\frac{V_H t}{I\,B} = \frac{1}{n\,e} \tag{3.7}$$

$$\frac{1}{\rho} = n\,e\,\mu \tag{3.8}$$

Where I is the current, B is the magnetic field, t is the thickness of the sample and n is the carrier concentration. By measuring the sample voltage, external field and applied current carefully, one can then calculate the carrier concentration with equation 3.7. We did this, and while already attached to the stage we then measured the sample resistivity with conjunction with the above calculation for n enables us to calculate the carrier mobility μ via equation 3.8.

A custom-built room temperature Hall apparatus equipped with a reversible 1.5 Tesla GMW Model 5403 electromagnet was outfitted with a LakeShore 421 Gaussmeter to measure the strength of the magnetic field on a mounted sample. Samples of known dimensions were sanded a thin as possible, ~0.5mm, and mounted with five contacts to the Hall stage to simultaneously measure the sample current, field, Hall and resistive voltages. Sample current was supplied by a Keithley 2400-LV Sourcemeter and sample voltage was collected with a Keithley precision multimeter. By varying or reversing the field strength a linear relationship can be developed as a more robust measurement of the carrier concentration. We varied the field from -1.6 to +1.6 T and collected 10 data points per measurement of carrier concentration. Figure 3.11 is an example of a scan of Hall voltage versus yield for a sample of pure SnTe, and is illustrative of the challenge of this measurement (at least with the equipment available to us). Despite a very large sample current of 50 mA, the Hall voltage over the applied field range of -1.6 to +1.6 T is less than 3 μV, in spite of the thinness of the sample. This is a consequence of the very high carrier concentration of this sample (and indeed all of the samples in this study). A picture of a sample mounted on the Hall stage is shown below.

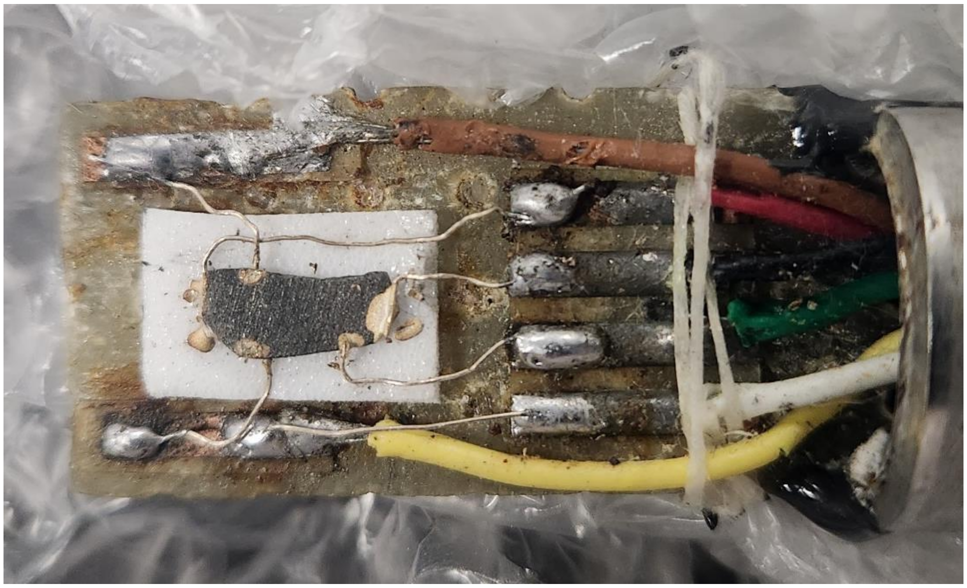

Figure 3.10: An image of a sample mounted on the Hall stage. Note the five contacts at different points on the sample.

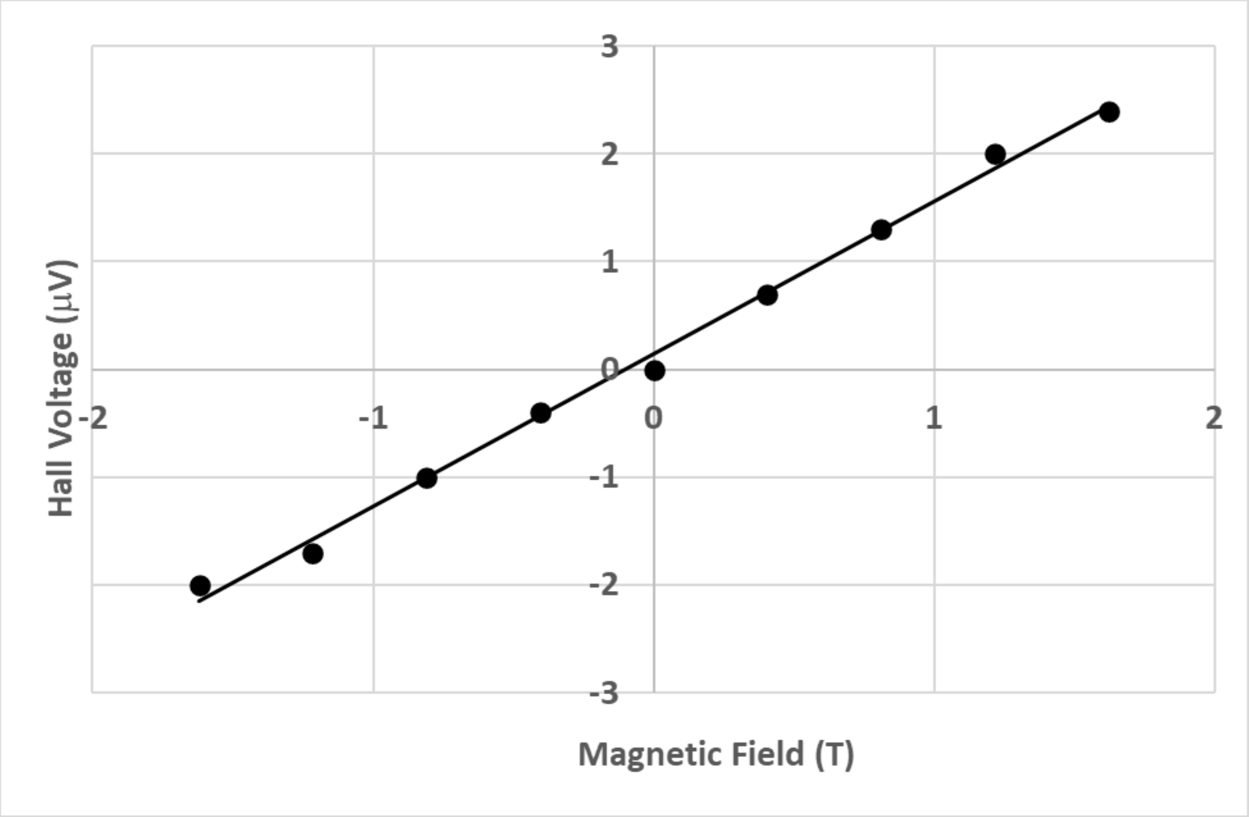

Figure 3.11: Hall measurement results for SnTe. Note the large fields and relatively small voltage signal.

3.8 Synthesis Summary

We describe a way to consistently synthesize polycrystalline GeTe-SnTe samples from ingots grown using direct fusion. Upon extraction of a prepared ingot of known stoichiometry, ingots were gently hand-ground by mortar and pestle before being loaded under Argon into stainless steel ball-mill jars with stainless steel ball-bearings with a mass/media ratio of about unity. High-energy ball milling was done in a short step of about 5 minutes – samples ball-milled for longer times (~30 minutes) proved to be of low density and/or brittle. Following milling, samples were loaded into SPS dies and pressed into cylinders/disks and pressed at 40MPa for 20 minutes at a maximum temperature of 400 °C before linearly reducing the pressure as the sample cools. Samples held at maximum temperature for longer times or samples cooled very quickly from the SPS hold temperatures proved to be brittle and did not survive to characterization.

We report that attempts to synthesize samples other than using direct fusion synthesis to be unsuccessful. Milling stochiometric amounts of elemental powder in the high-energy ball mill for several hours proved unable to provide samples free of unreacted elemental powder. Attempts at reactive-SPS (RSPS), where elemental fusion occurs during the SPS process, also proved unsuccessful. It is possible that long ball-mill times and rapid temperature changes, especially in samples transiting a phase transition, introduced additional stress and strain in the crystal lattice. This additional strain may have manifested itself in brittle or low-density samples, but more research is needed to quantify the precise effects of these synthesis processes on the microstructure and behavior of the system.

CHAPTER 4 STRUCTURAL BEHAVIOR STRUCTURAL STUDY THROUGH X-RAY DIFFRACTION AND RESONANT ULTRASOUND SPECTROSCOPY

A phase diagram first published by Bierly *et al o*f large crystals grown in 1963 demonstrated that GeTe and SnTe form a complete solid solution, where replacing Ge with Sn does not produce any intermediate compounds [67]. A key difference between GeTe and SnTe is that at room temperature they have different crystal structures. As can be seen in the original figure (below in Figure 4.1) from Bierly, both compounds have a high temperature cubic rocksalt phase (space group Fm-3m) and a low temperature rhombohedral phase (space group R3m), but while the temperature at which this transition occurs is well above room temperature for GeTe (~700K) it is well below room temperature for SnTe (~100K). As we increase the parameter ‘x’ as the occupation of Sn on the Ge site $Ge_{1-x}Sn_xTe$, the temperature of this transition decreases smoothly from the GeTe value towards the SnTe value. [67]. Much of the motivation for this thesis stems from the fact that these solid solutions thus offer the opportunity to study this structural phase transition and its effect on thermal and electronic transport over a very wide temperature range by controlling the composition of this binary alloy system.

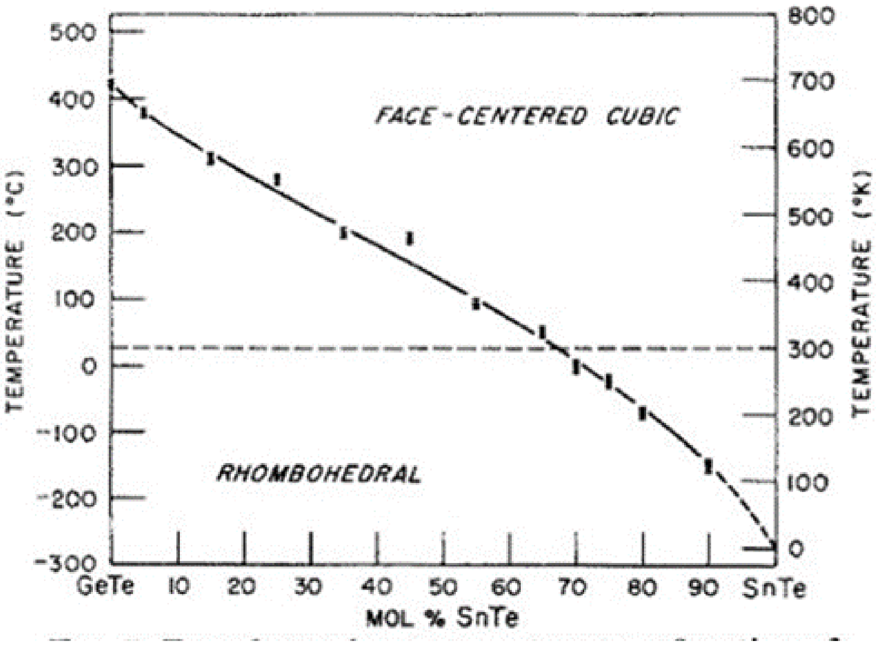

Figure 4.1: Figure from a 1963 paper from Bierly *et al* showing their proposed phase diagram of the GeTe-SnTe solid solution.

The cubic crystal system is the simplest and most symmetrical of the fourteen Bravais lattices. Within this cubic crystal system family, there exist three crystal types: simple cubic (SC), with lattice points at the vertices of a cube; body centered cubic (BCC), with an additional lattice site at the center of the cube; and face-centered cubic (FCC), with lattice sites on the eight corners of the cube and at the center of each of its six faces. The cubic structures extant in the GeTe-SnTe system assume the FCC habit, with a unit cell that is a cube, and its axes are all of equal length and perpendicular to each other. It is often called the "rocksalt" structure because table salt, NaCl, has this FCC crystal structure. NaCl is also a good comparison because it features two species of atoms that occupy every other site in the crystal lattice. The materials in this study, at the appropriate temperature to be in the cubic phase, exhibit similar characteristics. The usual crystallographic axes a, b, and c are equal and the angles between these axes are 90°. Due to the high symmetry in the cubic system, cubic materials are very common in semiconducting, thermoelectric, and other applications due to their versatility.

In slight contrast to the cubic system, the rhombohedral crystal group R3m comes from the class of trigonal systems and has less symmetry. It can be imagined as either a slight distortion of the cubic system or expressed as part of a larger hexagonal cell, which will be used below to compare structural data from different crystal systems. If we choose to imagine a distorted cubic cell, the rhombohedral R3m structure exhibited by room temperature GeTe differs from the cubic structure by an elongation along the (111) body diagonal, where the lattice spacings a=b=c is maintained but the cubic angle of 90° is reduced to something less. In the hexagonal translation, a=b is maintained, but the third parameter c is instead the length of the body diagonal, with the subsequent angles locked at 90 and 120 degrees respectively. An example for this translation is shown below in Figure 4.2. For rhombohedral GeTe, accepted literature values have the interior distortion angle very close to 90°, usually 88°- 88.3° [67].

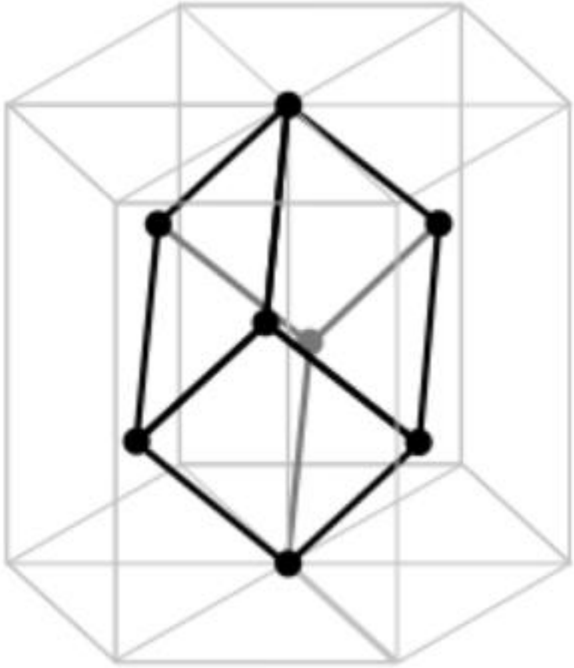

Figure 4.2: This example is an illustration of the rhombohedral cell (dark lines) within a larger hexagonal cell (faint grey lines).

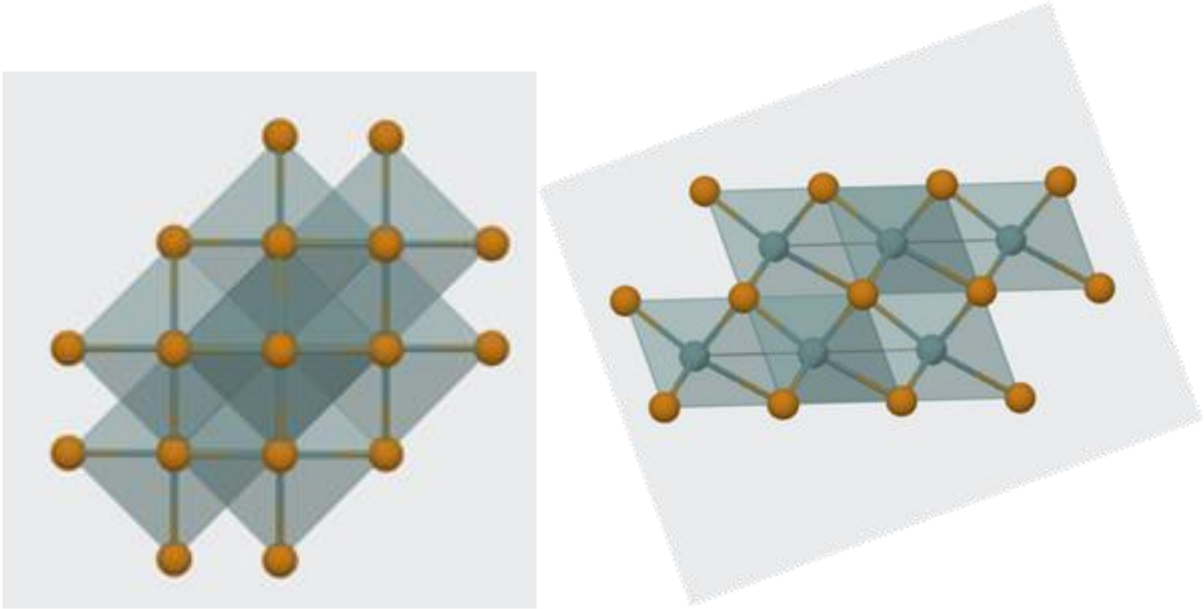

Figure 4.3: Illustrations of cubic and rhombohedral structures generated by Materials Project. In this example, the rhombohedral angle is exaggerated but for GeTe the distortion angle is very close to 90°.

In order to compare cubic and rhombohedral systems, it is necessary to translate the parameters to a common crystal system. By comparing the expression for the volumes of each primitive cell, we can develop a relationship between the rhombohedral parameters and the cubic parameters to make a direct comparison of lattice constants. To find the associated rhombohedral angle from the hexagonal system, angles were calculated using a matrix transformation with the known relationships between crystal systems. Given rhombohedral lattice parameters a_R and c_R and cubic lattice parameter a_C we can develop the equivalence from their volumes:

$$V_{Rh} = \frac{\sqrt{3}}{2} a_R^2 c_R \tag{4.1}$$

$$V_C = a_C^3 \tag{4.2}$$

Setting them equal and solving, we develop the condition for when rhombohedral parameters yield a cubic structure:

$$\frac{c_R}{a_R} = \frac{2\sqrt{3}}{\sqrt{2}} \tag{4.3}$$

$$a_C = a_R\sqrt{2} \tag{4.4}$$

$$c_R = a_c\sqrt{3} \tag{4.5}$$

In sum, this translation allows us to continuously compare lattice values and angles as we switch between cubic and rhombohedral crystal systems.

4.1 X-ray Diffraction of $Ge_{1-x}Sn_xTe$

X-ray diffraction (XRD), being a non-destructive evaluation method, was performed throughout the synthesis process to monitor any changes in the crystal structure as well as identify the presence of secondary phases and ensure sample purity. In addition, the peaks produced by an XRD pattern can be fitted to literature and database peak profiles such as the Inorganic Crystal Structure Database (ICSD). Through a process called Rietveld refinement, important sample parameters like the crystal group, lattice spacing, and angles for a theoretical XRD pattern can be compared against a real pattern and refined with a scoring mechanism. This is the standard practice for evaluating crystalline materials and is a highly developed procedure. For Rietveld refinements below, the software package used was PDXL 2 developed by Rigaku.

We begin with XRD patterns obtained from our end member materials: powdered GeTe and SnTe. As well-studied materials there are many reference patterns with which to compare our data, and a representative of each of these reference patterns is displayed below the spectra to demonstrate both the correctness of fit as well as the sample purity. While the patterns are similar, there are two key differences that reflect their different lattice parameters and crystal structures. As Sn is slightly larger than Ge, the lattice parameter of SnTe is larger than that of GeTe, pushing all peaks for the former compound to smaller angles. In addition, the rhombohedral structure of GeTe causes what is a single peak in SnTe at about 40° to split into two peaks. As sample temperature rises or as Sn is substituted on the Ge site, these peaks narrow and eventually overlap in the cubic phase.

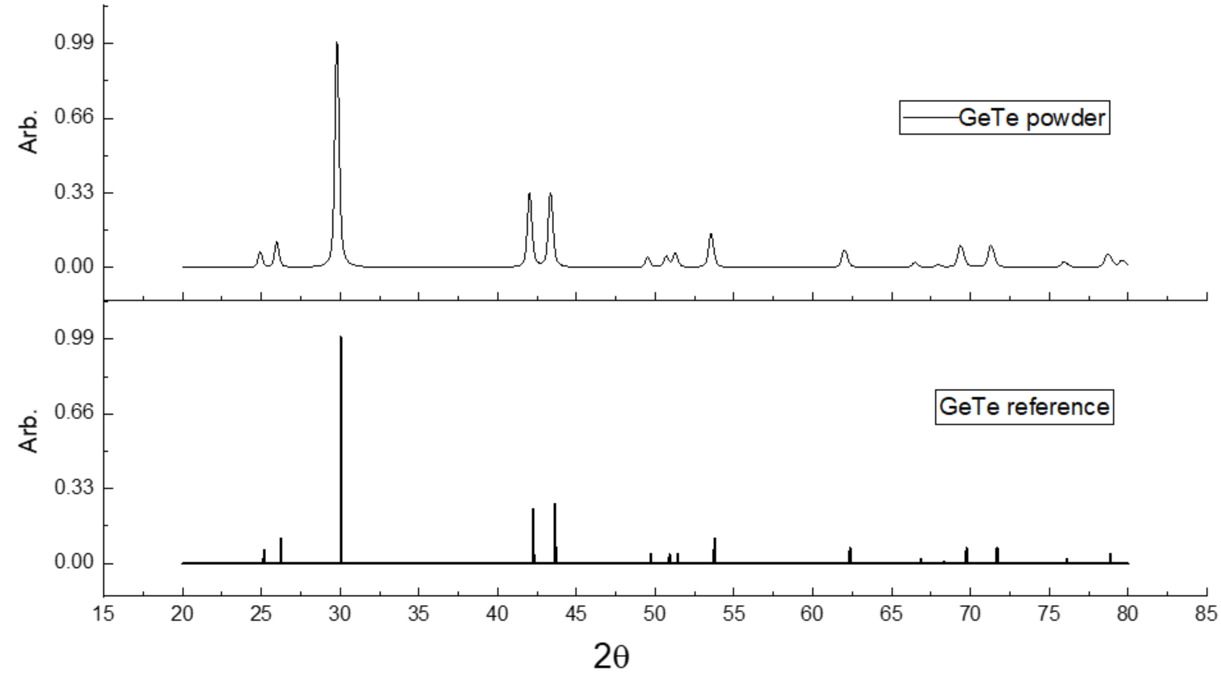

Figure 4.4: Representative GeTe powder XRD data with reference. Note the doublet peak between 40- and 45-degrees 2θ, an indicator of rhombohedral structure.

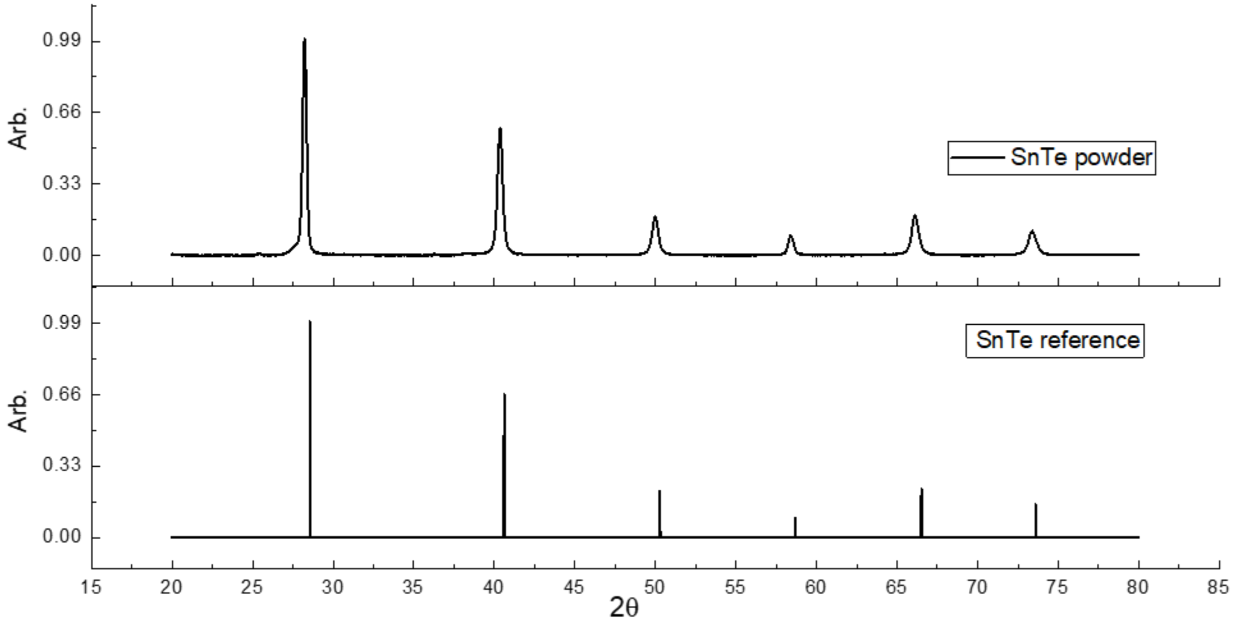

Figure 4.5: SnTe powder XRD data with reference. Due to high symmetry in the cubic system, many peaks overlap so there are relatively few peaks.

As Sn is substituted onto the Ge site in small amounts, its incorporation into the lattice raises the average lattice distance in the crystal primitive cell. This slightly shifts the peak positions, but the doublet peak in the mid 40° is maintained, albeit at a slightly narrower spacing. As demonstrated in Figures 4.6 and 4.7 below, the whole pattern and the inset show a rhombohedral structure that is becoming more and more cubic as Sn content increases. Here and throughout, we will refer to solid-solution samples by their 'x' values in $Ge_{(1-x)}Sn_{(x)}Te$ which indicates their Sn content; x=0.05 means 5% Sn on the Ge site, x=0.20 means 20% and so on, where x=0.0 is GeTe and x=1.0 is SnTe.

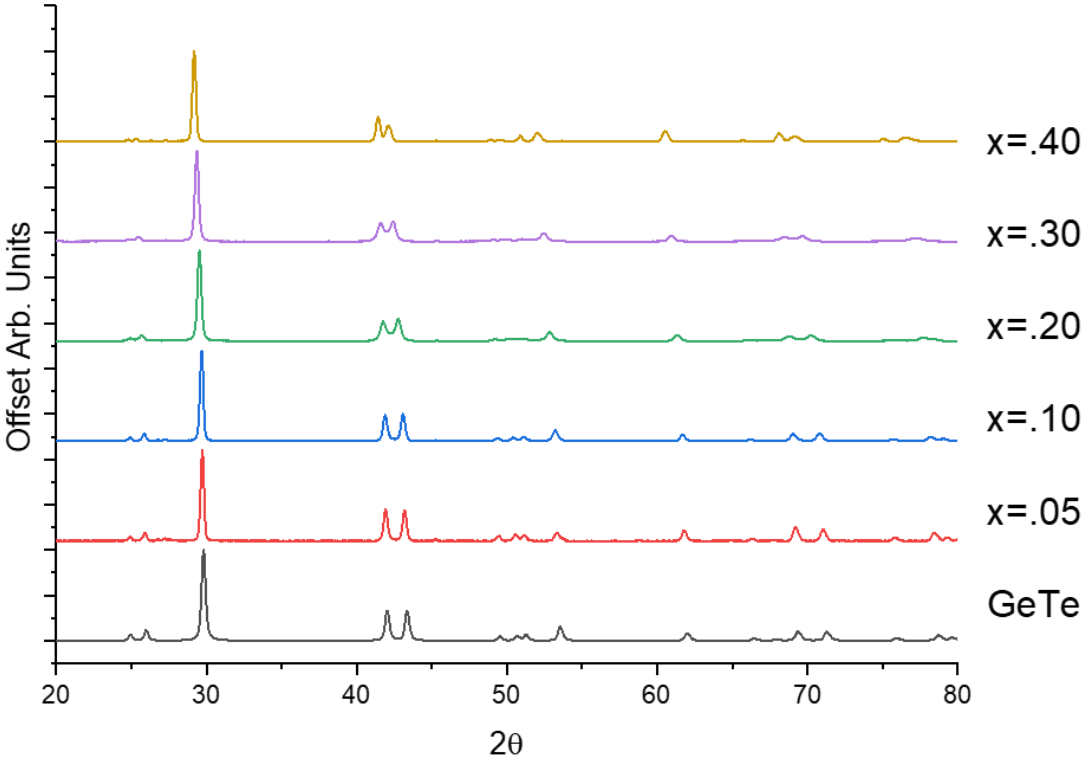

Figure 4.6: XRD spectra of Germanium rich samples up to x=.40, demonstrating high sample purity and no significant contributions from other phases.

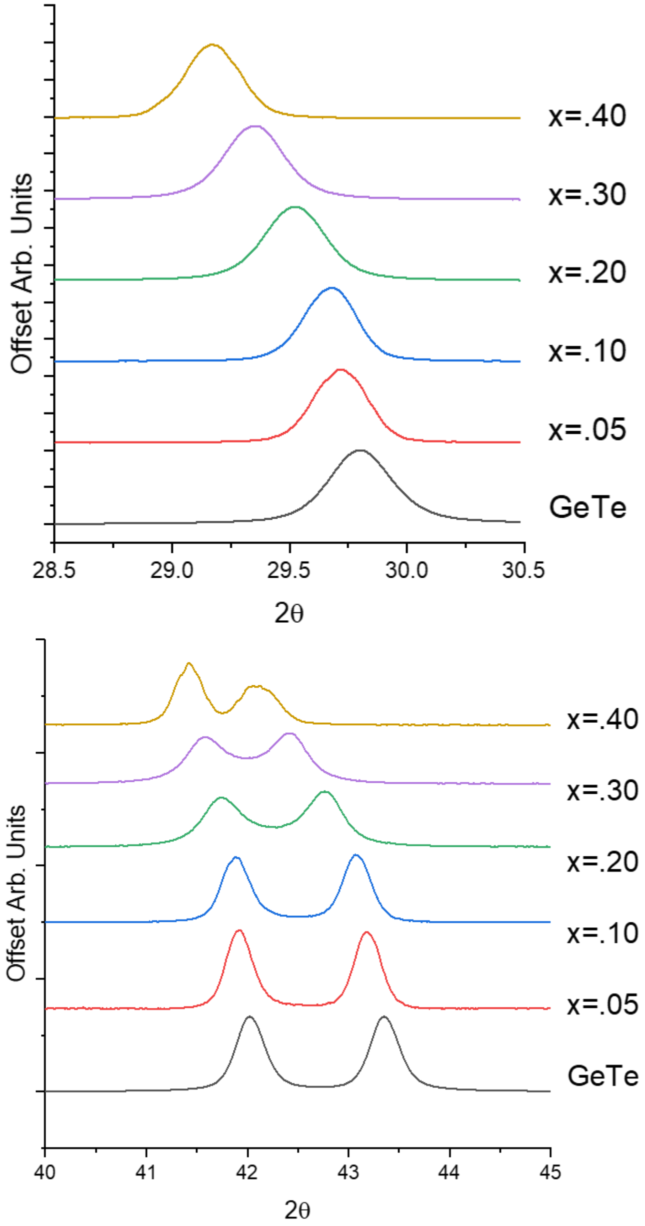

Figure 4.7: Insets from the data in Figure 4.6 showing the trends of the main peak (above) near 30° and the double peak (below) between 41-44°. The shifting of peaks to lower values indicates a larger lattice parameter, and the narrowing of the doublet indicates a smaller rhombohedral angle.

As we approach samples that are cubic at room temperature, the distinct doublet peaks are harder to resolve as the overlap becomes more significant. While the literature data suggests the cubic phase may be reached at about x=.70, our collected data suggests that x=.60

reflects a nearly cubic structure at room temperature, with a calculated rhombohedral angle of 89.99°. A full list of calculated lattice parameters and rhombohedral angles for room temperature samples is detailed below in Table 4.1.

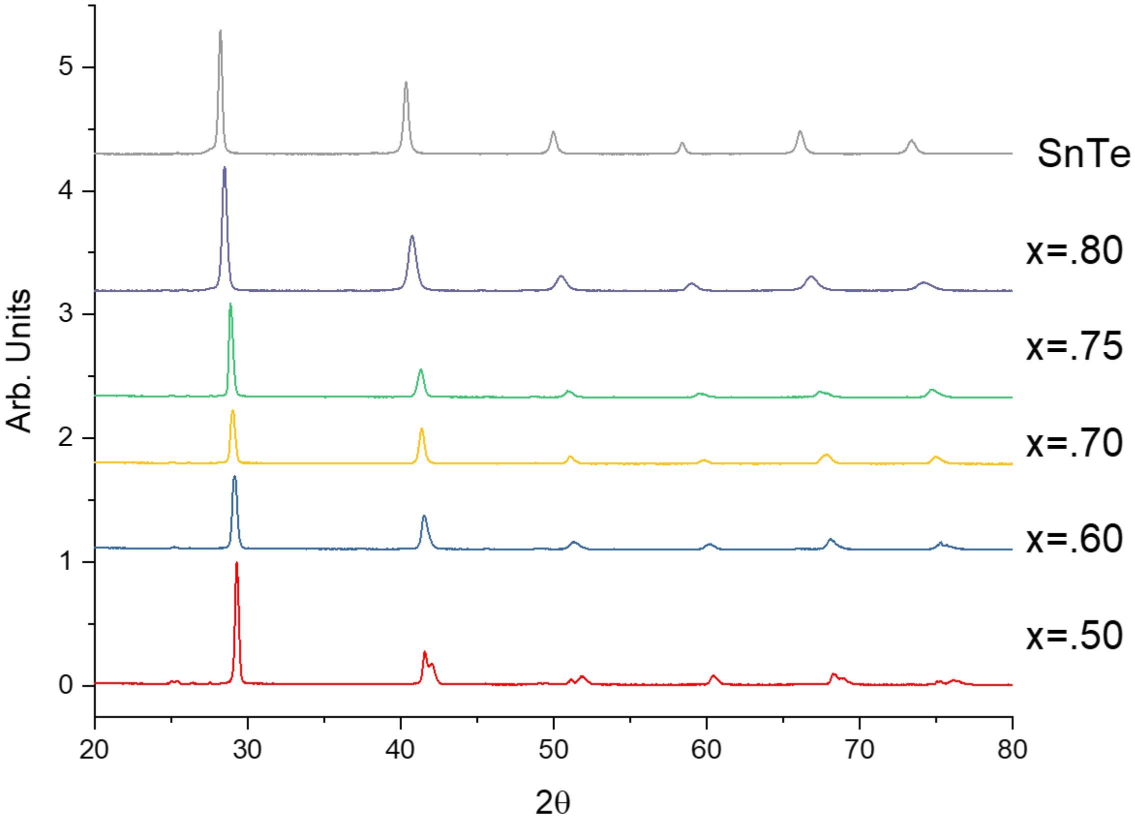

Figure 4.8: XRD spectra of Sn rich samples showing high sample purity. Note the gradual shift to lower angles as Sn content increases, and the peak splitting in the x=.50 sample at about 42°.

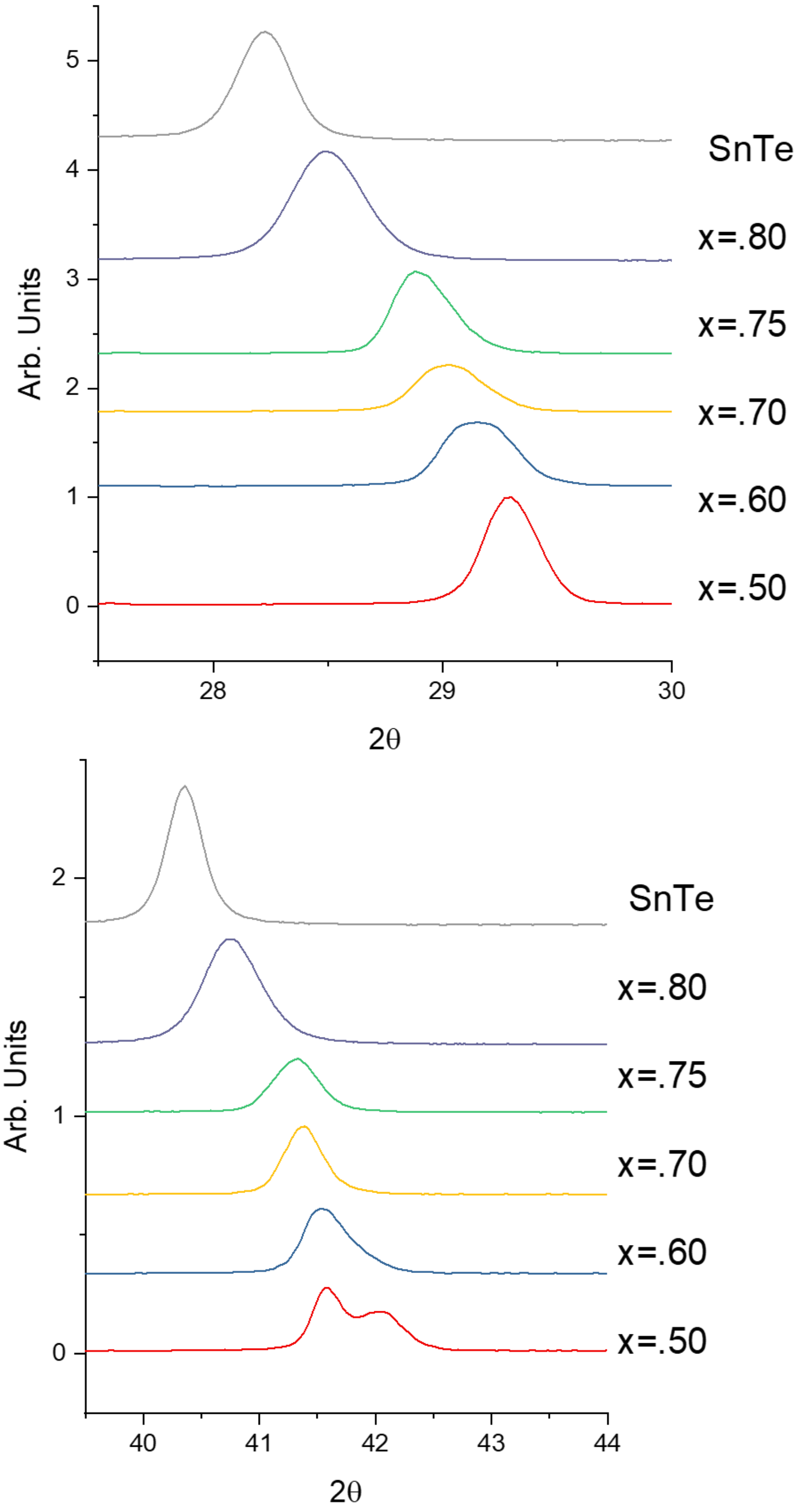

Figure 4.9: Insets from the data in Figure 4.8 showing the trends of the main peak (above) near 30° which is consistent with a larger lattice parameter with more Sn content. The inset of the second largest peak and the double peak (below) between 41-43° shows how the x=.50 sample is still rhombohedral, the x=.60 has a broad peak that is nearly cubic, and the x=.70 shows one peak reflecting a cubic structure.

Sn content "x"	a_H (Å)	C_H (Å)	a_R (Å)	angle α_R	a_C (Å)	angle α_c
0	8.332	10.674	5.982	88.27		
0.05	8.362	10.691	5.996	88.41		
0.2	8.452	10.703	6.045	88.71		
0.3	8.520	10.722	6.080	88.95		
0.4	8.580	10.760	6.116	89.09		
0.5	8.654	10.783	6.155	89.34		
0.6	8.779	10.752	6.207	89.99		
0.7	8.810	10.790			6.2296	90
0.8	8.854	10.844			6.2606	90
1	8.938	10.947			6.3201	90

Table 4.1: A table of fitted hexagonal lattice constants from Rietveld refinements at room temperature. Cubic samples were converted into an equivalent hexagonal lattice using the relationships above.

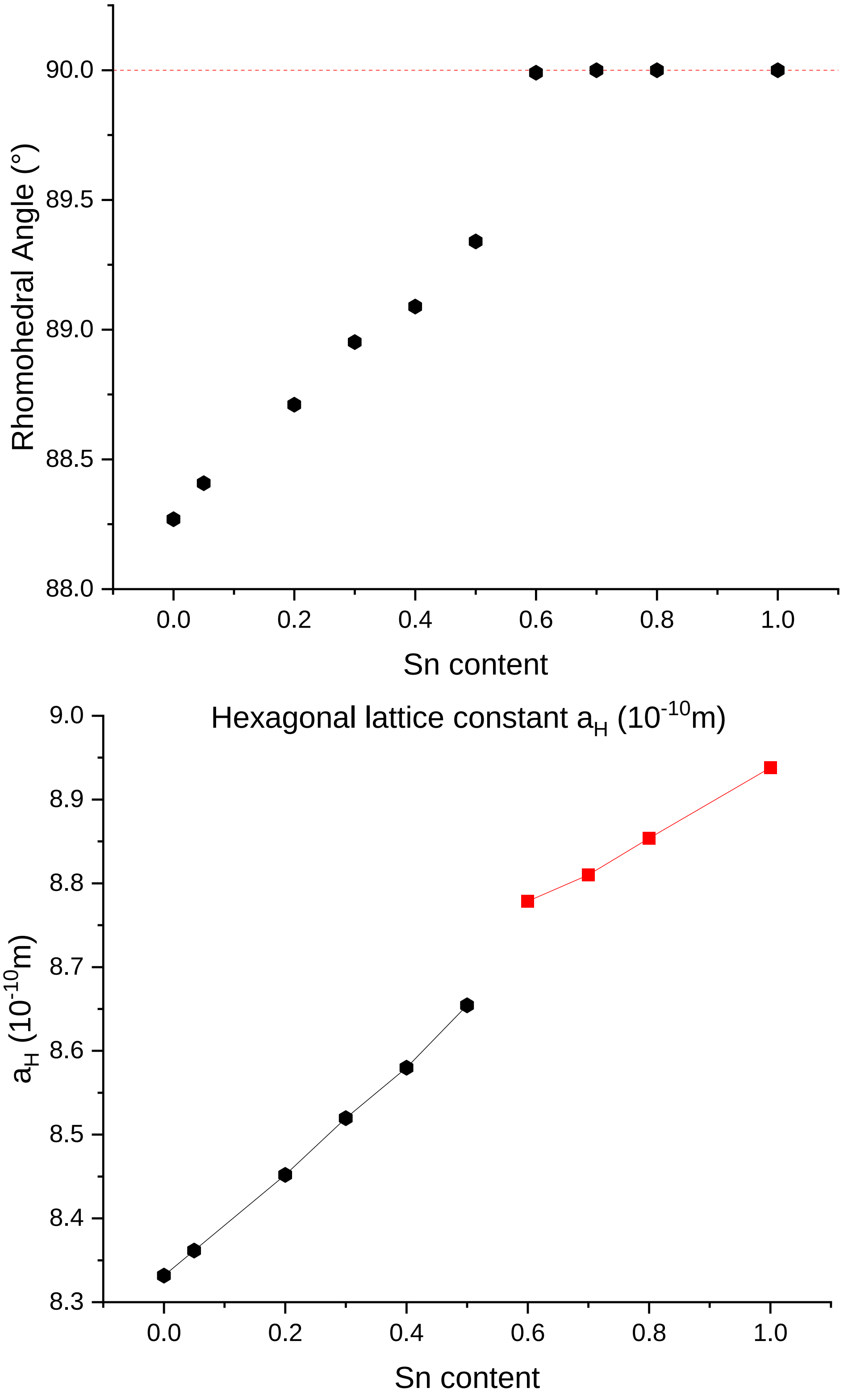

Figure 4.10a: Graphical representation of the data in table 4.1, showing the rhombohedral angle versus Sn content (top) and hexagonal lattice constant versus Sn content (bottom) at room temperature.

In addition to the room temperature XRD data, high-temperature data was taken while equipment was available on the same setup for a select number of powder samples we synthesized. These samples demonstrated a stark contrast in the XRD patterns between cubic and rhombohedral phases and showed that the transition occurs over a fairly narrow temperature range and is reversible. For x=.25 the transition temperature indicated by HT-XRD was 230° C +/- 10 and for x=.50 at about 130° C +/- 10.

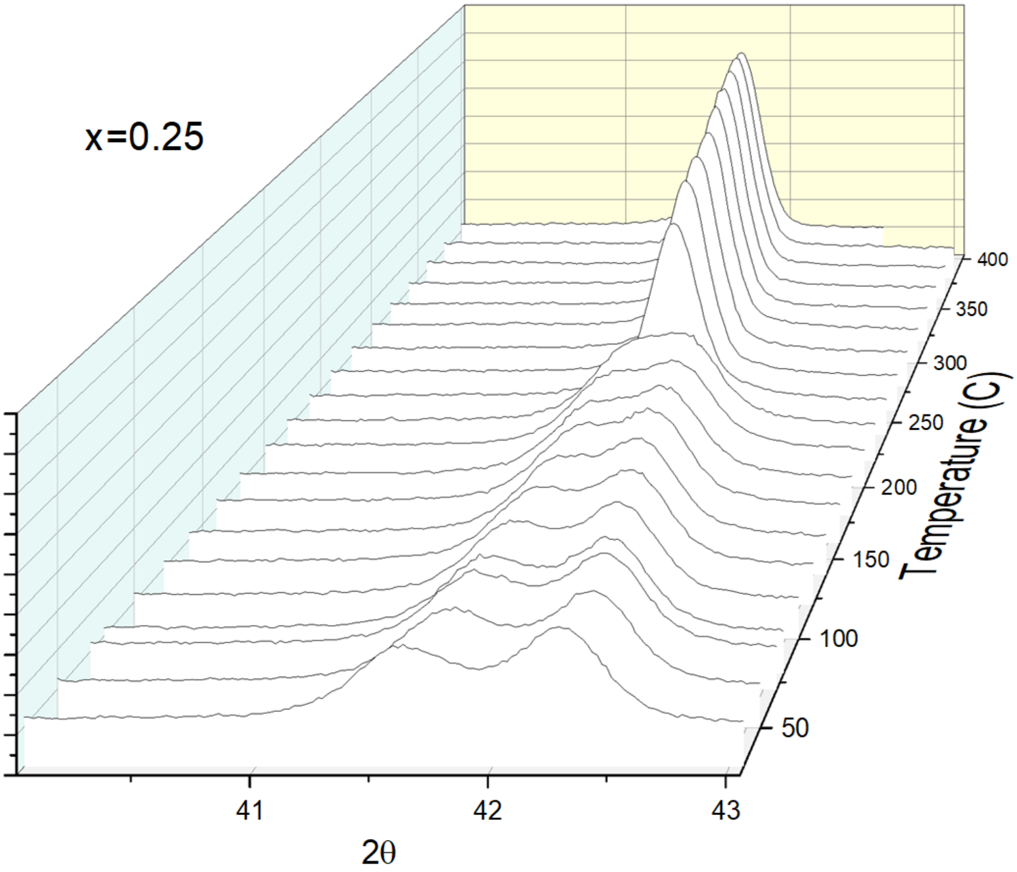

Figure 4.11: High-temperature XRD spectra for x=.25 upon heating. This is an inset of the full spectrum showing the behavior of the doublet peak combining to a single peak at 240° C

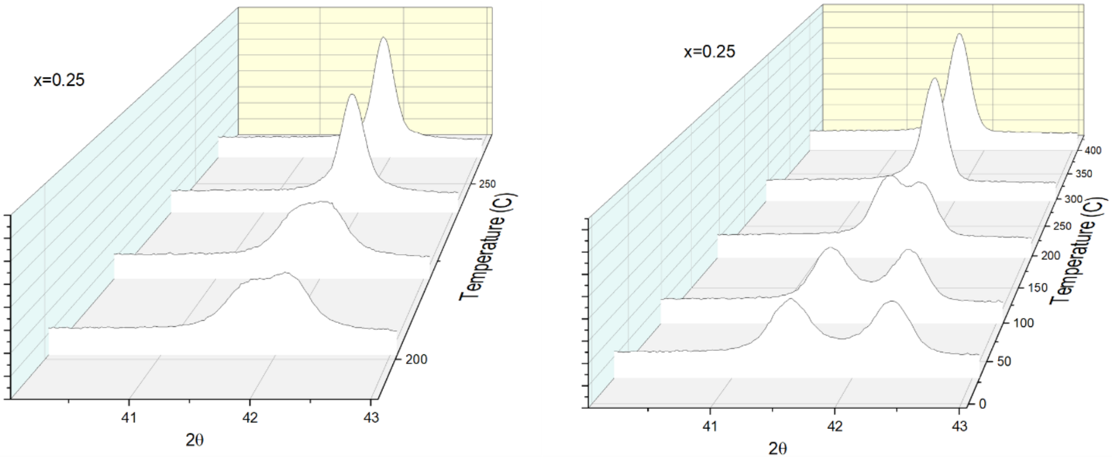

Figure 4.12: Insets for the same spectra, showing the rapidity of the transition. Left, a closer view of the peaks combining upon heating between 220° C and 240° C . On right, the same sample but data taken upon cooling, showing the peak splitting between 300° C and 200° C.

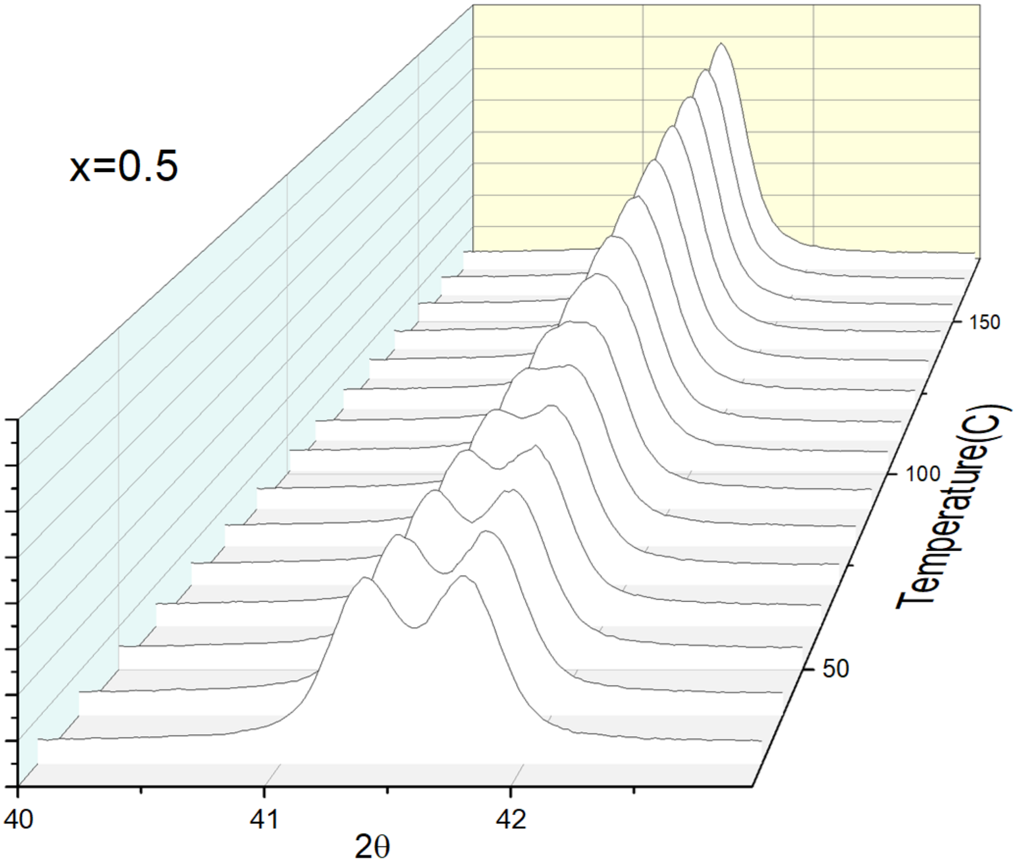

Figure 4.13: HT-XRD spectra for an x=0.5 upon heating. Note how the doublet peak flattens before truly combing at 130° C.

While the phase transition temperature of GeTe has a well-studied and established phase transition temperature around 400 °C, the transition temperatures for $Ge_{(1-x)}Sn_{(x)}Te$ alloys have been reported by scant few researchers since the initial phase diagram published by Bierly et al in 1963. Here we report important contributions provided by analysis of High-Temperature XRD data of Sn concentrations x=0.25 and x=0.50 demonstrated quite persuasively in Figures 4.11 and 4.13. These transition temperatures (at 240°C for x=0.25 and 130°C for x=0.50 respectively) are displayed alongside the reported data points from Bierly (1963) below in Figure 6.1. Also included in this figure is a single contribution of the room-temperature XRD analysis, that of the firmly cubic phase displayed by the x=0.70 sample. Taken together they agree well with the initial work, but with some gaps still to be worked out.

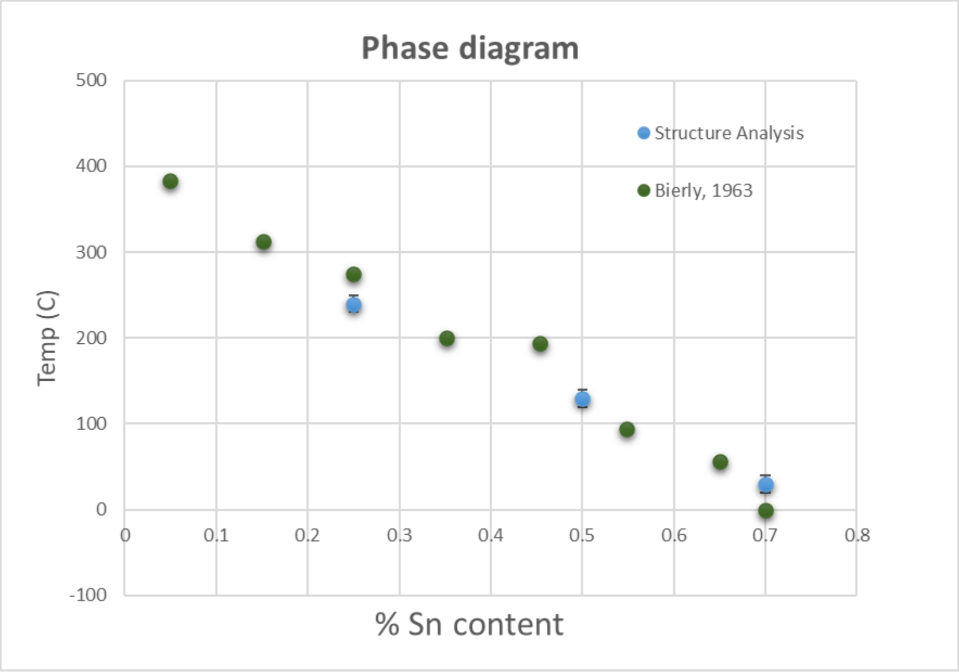

Figure 4.14: Phase transition temperatures from XRD in this study (blue) compared with data from Bierly et al (green). Note the error bars on the XRD data of ±10 °C which reflect the step size of the HT-XRD scans as well as uncertainty in the room-temperature data.

4.2 Resonant Ultrasound Spectroscopy of $Ge_{1-x}Sn_xTe$

Resonant Ultrasound Spectroscopy (RUS) is an emerging method for the characterization of the vibrational character of crystalline materials [112]. Relying on sample dimensions and density, RUS probes a sample by sweeping through a spectrum of frequencies and picking up on which frequencies activate the harmonic modes of a material. As it relies on external physical parameters to iteratively evaluate elastic constants, sample quality is of utmost importance. Critical to the evaluation of sample quality is the material density. A sample may have low density due to a variety of factors, including voids or cracks, incomplete fusion of materials during synthesis, or mechanical stresses unevenly applied during sample processing and sintering. As such, all synthesized samples were checked for density after the SPS process using both geometrical and Archimedes methods to ensure high sample quality. Any sample below 95% theoretical density was not used for further measurements. Theoretical sample density was determined using a simple rule of mixtures following a linear trend between the end members. A good sample density is critical to not only RUS measurements, but also in the thermal characterization process of the Laser Flash Analysis (LFA).

Another critical aspect for RUS measurements is a sample with well-defined dimensions that is free of chips, cracks, and other physical irregularities. A minor crack in a sample will disrupt the natural modes of vibration in a sample and will mix the RUS signal with errant noise. In addition, the sample must have parallel sides and sharply defined edges, as the sample is positioned between two piezoelectric pickups that contact the sample edges. To assure good contact with the sample as well as minimizing any anisotropic affects, sample contact with the transducers was rotated to different parts of the sample and spectra were compared to ensure that the spectra were representative of the performance of the material.

As mentioned in Chapters 2 and 3, due to the symmetry of cubic and rhombohedral crystal systems, the elastic tensor can be reduced to just two key components, C_{11} and C_{44}. Using an iterative process described by Migliori *et al* [94] initial elastic tensor ansatz parameters generated an expected series of RUS peaks that were fit to observed spectra taken from the sample, using a least-squares method [100-101]. Results for C_{11} and C_{44} values are displayed below in Figure 4.15. As described in Chapter 2, these elastic tensors can be used in conjunction with sample density to calculate the speed of sound, which is shown as a function of Sn content in Figure 4.16.

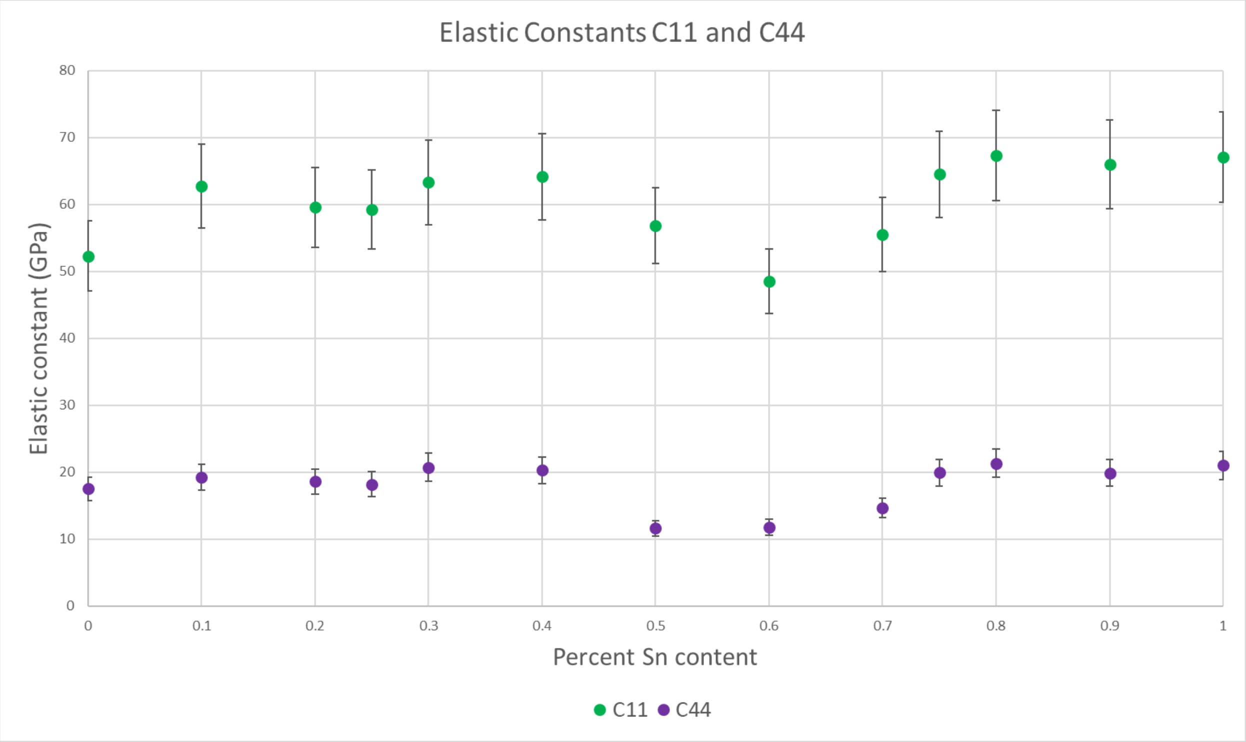

Figure 4.15: Elastic constant values for matrix indices C11 and C44 as a function of Sn content. Trend shows a softening near expected structural transition. Data shown with 10% error bars.

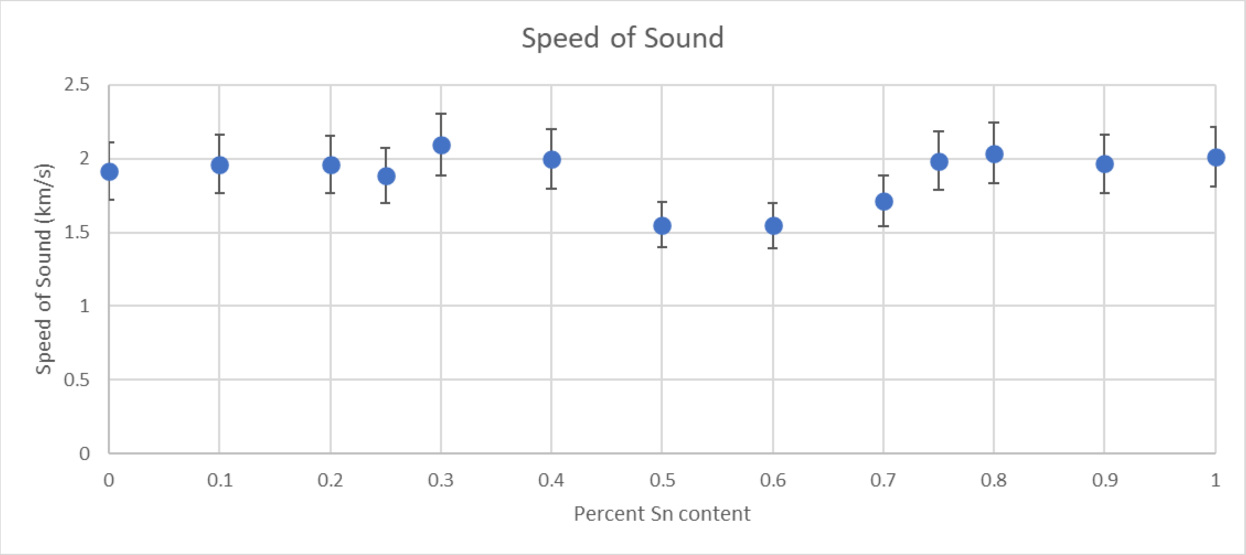

Figure 4.16: Speed of sound values calculated from elastic moduli data. Speed of sound data supports more evidence of lattice softening near structural transition temperature. Data shown with 10% error bars.

With the room temperature measurements offering clues, we can compare these RUS results to similar data taken as a function of temperature. Previous studies of this transition by Seddon [109] show that the elastic moduli soften as they approach the structural phase transition before sharply stiffening and flattening out at a higher value than before. This is demonstrated with a diagram from Seddon's paper shared below in Figure 4.17. We recover results that at room temperature seemingly agree, but a more thorough characterization of these elastic constants as a function of temperature would be a fruitful direction of study.

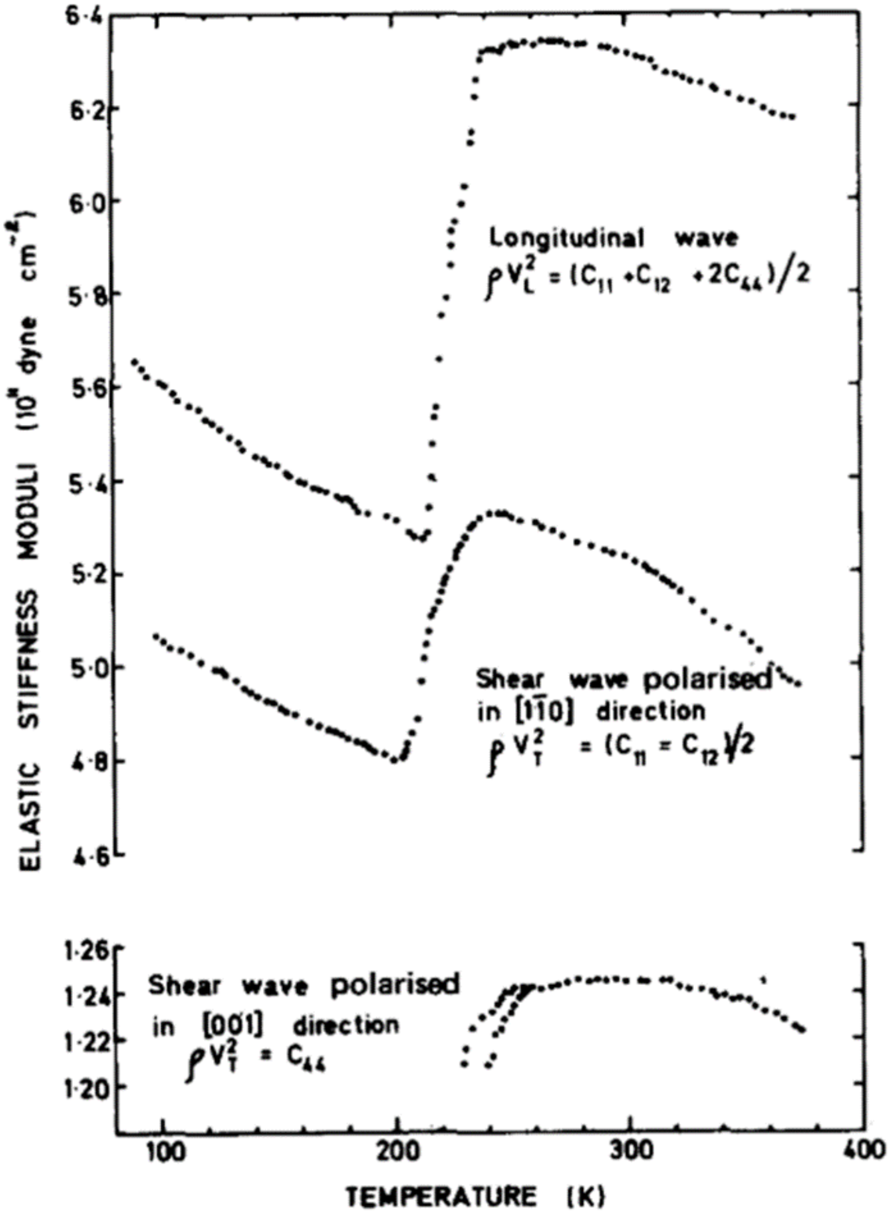

FIG. 1. The elastic moduli derived from the velocities of ultrasonic waves propagated in the [110] direction of 20 mole.% GeTe–80 mole.% SnTe alloy single crystal.

Figure 4.17: A figure reproduced from Seddon's 1975 paper [109]. Note the shape of the elastic moduli curve as a function of temperature as it approaches the structural phase transition. This is for a sample 'x' value of x=0.80, which is predicted to be cubic at room temperature.

4.3 Section Summary

The x-ray diffraction data make a strong case for the samples being single-phase with little to no secondary phases. In addition, the analysis of lattice constants shows that the solid solution neatly and gradually modifies the lattice parameter from one end-member to the other, showing the behavior of the predicted solid solution with trends that follow the rule of mixtures. High temperature data demonstrates the rapid and reversible changes in crystal structure near the temperatures expected from literature. The characteristic feature in the rhombohedral to cubic structural phase transition in these mixed crystals is the convergence of a double peak in the range of 40-45 degrees 2θ as the rhombohedral structure evolves into the cubic one, related to the "stretch" along the body diagonal and a concomitant increase of the rhombohedral angle to 90 degrees. We shall see in Chapter 5 that these subtle changes in crystal structure can have profound effects on the electronic and thermal behavior of these semiconductors.

Consistent with the observations from our XRD data, when the system is near the expected structural transition temperature, as is the case for x=0.50- 0.70 samples, the RUS data indicates a softening of the elastic constants. In general samples doped with a little tin ("Ge-rich") have higher elastic constants than GeTe, while samples with little Ge content ("Sn-rich") closely match the behavior of end member SnTe. This trend is most pronounced in the C_{11} data and less so in the C_{44} and speed of sound data. These measurements lead to the conclusion that when the system temperature is in proximity to this crystallographic transition there is an overall softening of the structure. For samples x=0.80 and above we see an increase in the C11 elastic constant compared to the room-temperature rhombohedral samples, but only by a small amount.

CHAPTER 5 ELECTRICAL TRANSPORT AND ANALYSIS: RESISTIVITY, SEEBECK, AND HALL DATA

This chapter will detail the data obtained from electronic transport measurements via the methods described in Chapter 3, specifically the electrical resistivity, Seebeck coefficient, and Hall data. Of critical interest for any thermoelectric characterization, this data enables a calculation of the electronic portion of ZT, the *power factor*, from data collected from the ZEM in the form of electronic resistivity and Seebeck coefficient. Trends in transport data can be used to make inferences about the underlying mechanisms that drive the observed behavior of the material. Many samples were synthesized via methods described in Chapter 3, but not all samples survived to characterization. Some samples had densities far below theoretical density, while other samples were brittle and did not survive the full characterization process. The results shown below are from representative samples for which the same physical sample was carried through each process. In practice, density and RUS measurements were followed by LFA measurements of thermal conductivity with ZEM measurements of resistivity and Seebeck occurring last.

5.1 Electronic Resistivity of the $Ge_{(1-x)}Sn_{(x)}Te$ system

As a well-studied material, it has been discovered that while pristine GeTe is predicted to be a semiconductor with a band gap on the order of 0.3 eV, in practice it often exhibits nearly metallic properties [33]. This is due to the low vacancy formation energy on the Ge site, and with every Ge vacancy providing a nominal +2 charge [45,115]. These vacancies are responsible for making GeTe a *p*-type semiconductor, and a high number vacancies can push the carrier concentration to values that often make GeTe exhibit metallic behavior. As the vacancies are naturally occurring, it is difficult to precisely control the number of vacancies and this in turn results in a large spread of reported resistivity values, as the resistivity is directly correlated with the carrier concentration. All this to say that semiconductor systems are very sensitive to small changes in stoichiometry and defects such as vacancies can play a large role in determining their properties, and GeTe is no exception. As we move from GeTe into the $Ge_{1-x}Sn_xTe$ system, at low concentrations of Sn we might expect to see a large change in the electrical behavior as some of these vacancies are filled by Sn atoms. This was demonstrated by a 1975 paper on these materials from Lewis, J. E., and Lasjaunias, J. C. [68] with their resistivity data displayed in Figure 5.1 below. Note that this is not the absolute value of the resistivity, but the difference between measured values and the value for GeTe, which they cited as 1.1×10^{-4} Ohm-m. As single crystals, the quoted absolute values of resistivity will be in general lower than the polycrystalline samples developed in this study, but the shape of the curve is the most interesting and salient point.

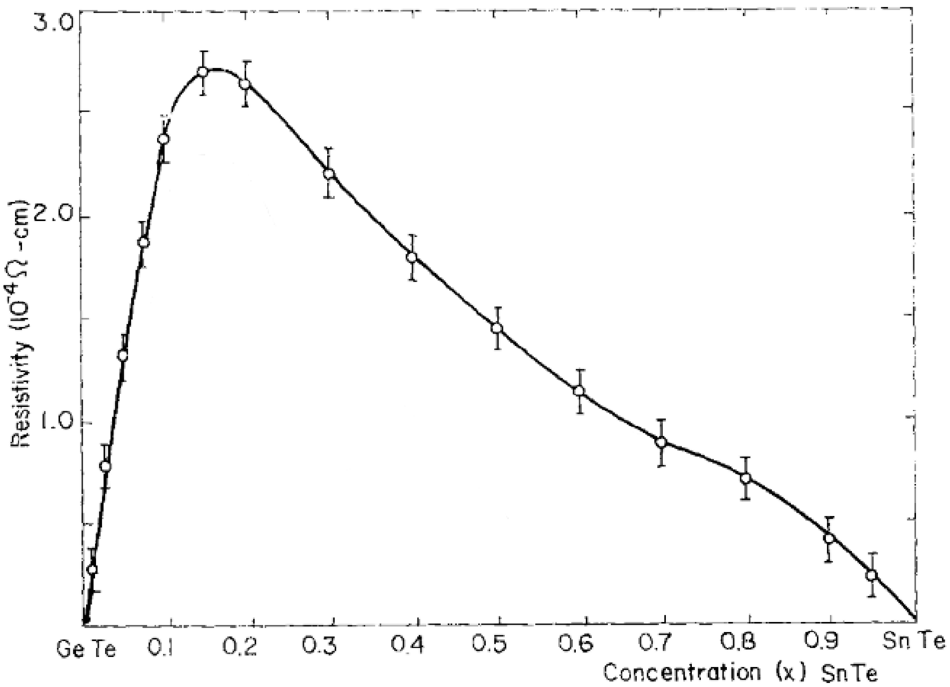

Figure 5.1: Resistivity of Ge(1-x)Sn(x)Te system from Lewis *et al* (1975) [68]. Note the rapid increase in resistivity as Sn is introduced, which then peaks and descends at higher Sn concentrations.

Several samples of GeTe were produced and measurements on the ZEM showed similar results. In general, the resistivity of GeTe increases with temperature which is indicative of a metallic system. A representative data set of the resistivity of GeTe in addition to sample literature data is shown in Figure 5.2.

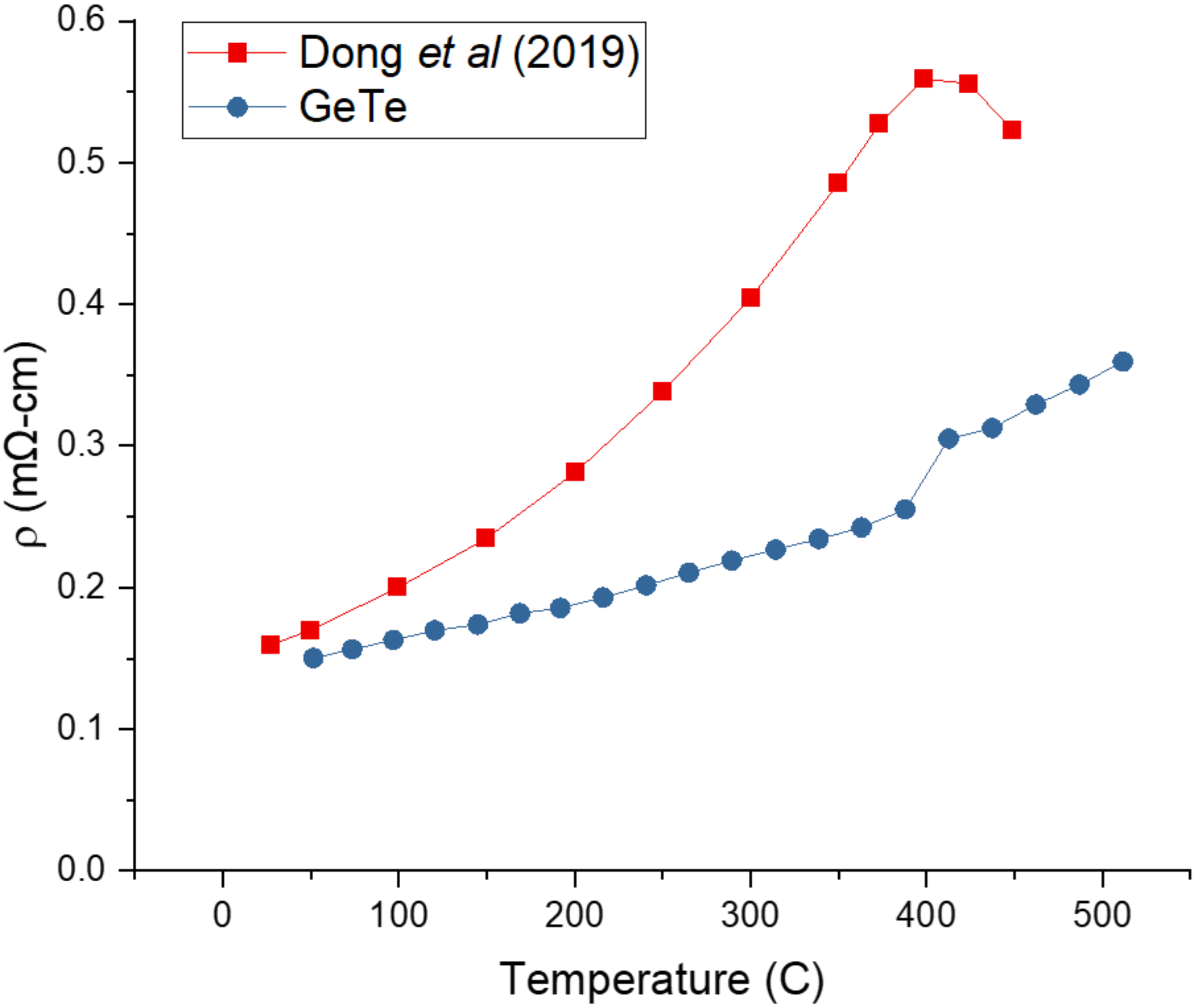

Figure 5.2: Resistivity of GeTe in this study compared to a literature data set. Note the discontinuity in resistivity about the temperature of the structural phase transition in both data sets. Dong *et al* is in the references as [42].

Not being strictly smooth curves, many measurements have discontinuities in temperature ranges that were suggestive of the effect of the structural phase transition. Some data sets were more dramatic than others, for example consider the data set for x=0.10 below in Figure 5.3. For samples with low concentrations of Sn, the resistivity rose substantially with the inclusion of Sn, with the peak resistivity occurring in the x=0.10 sample.

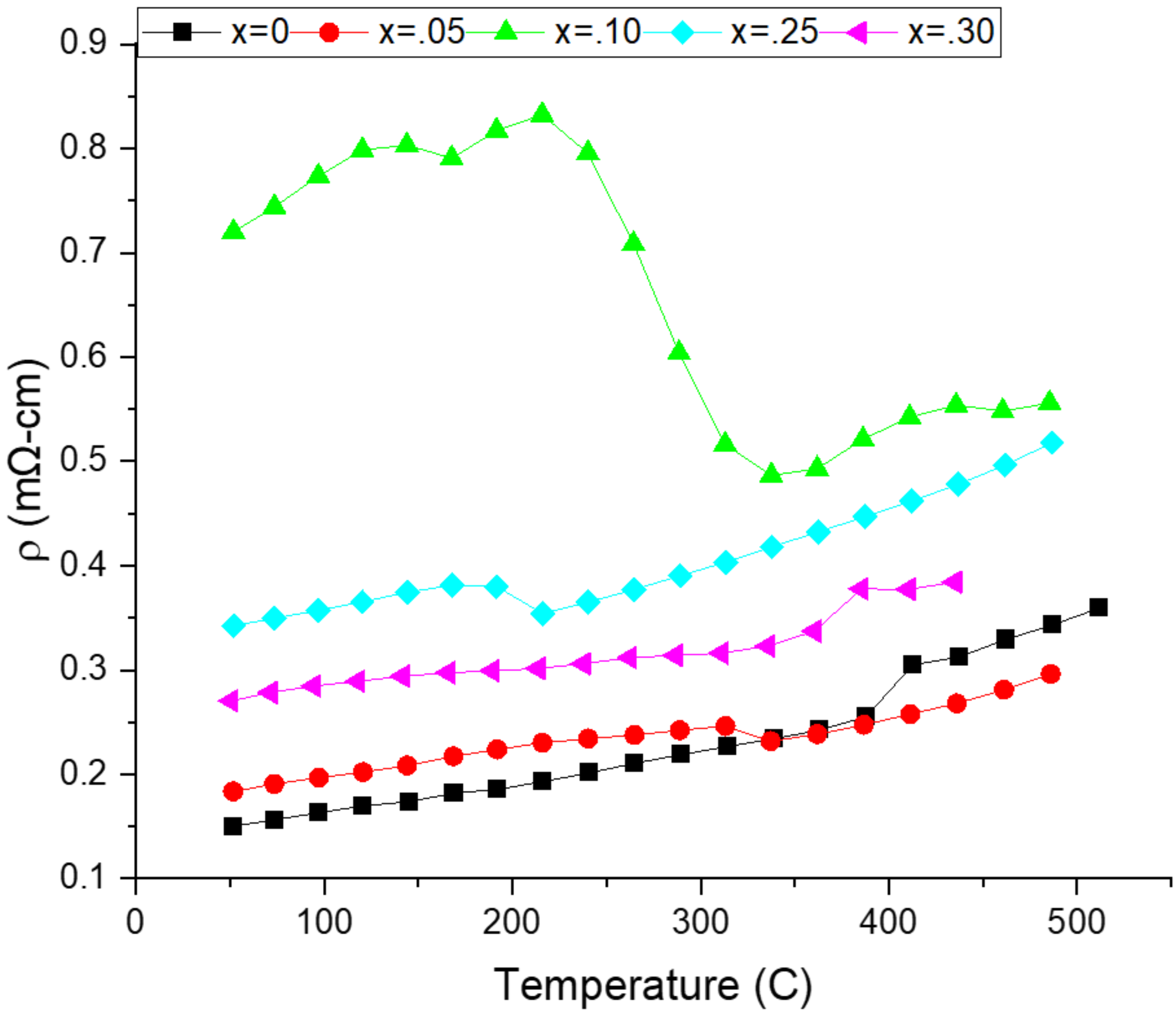

Figure 5.3: Resistivity of Ge-rich samples. GeTe data is re-represented as the x=0 dataset. Note the peak in resistivity for x=.10 samples, as well as small discontinuities in the other series.

Examining the Ge-rich resistivity data it can also be seen that while the GeTe sample appears to shift to a higher resistivity with the structural transition, the x=0.05 and especially the x=0.10 see a decrease in the resistivity at the phase transition temperature. One can also see a trend in the lower temperature phase that agrees with Lewis *et al* in that the observed resistivity forms a peak on the Ge-rich side of the solid solution and then quickly descends back towards an intermediate value. We will see this trend continue for the Sn-rich samples. As with the end member GeTe, the trend of increasing resistivity with temperature suggests metallic behavior in the system driven perhaps by a high carrier concentration and an increasing rate of carrier-carrier scattering.

While many synthesized concentrations of Sn on the Ge site provided consistent resistivity data from sample to sample, others proved more difficult. In particular the samples with x-values of x=0.20 and x=0.40 showed a spread in resistivity values. In Figure 5.4 below are two measurements of x=0.20 from different samples, both lower than the x=0.10 resistivity but it is unclear which data set accurately represents the trend in resistivity as it decreases with Sn content. Both series also show bends in the curve suggestive of phase transition temperatures, but at different temperatures. If we were to take the Bierly et al. phase transition figure as a guide, these samples should transition from rhombohedral to cubic at about 300 °C.

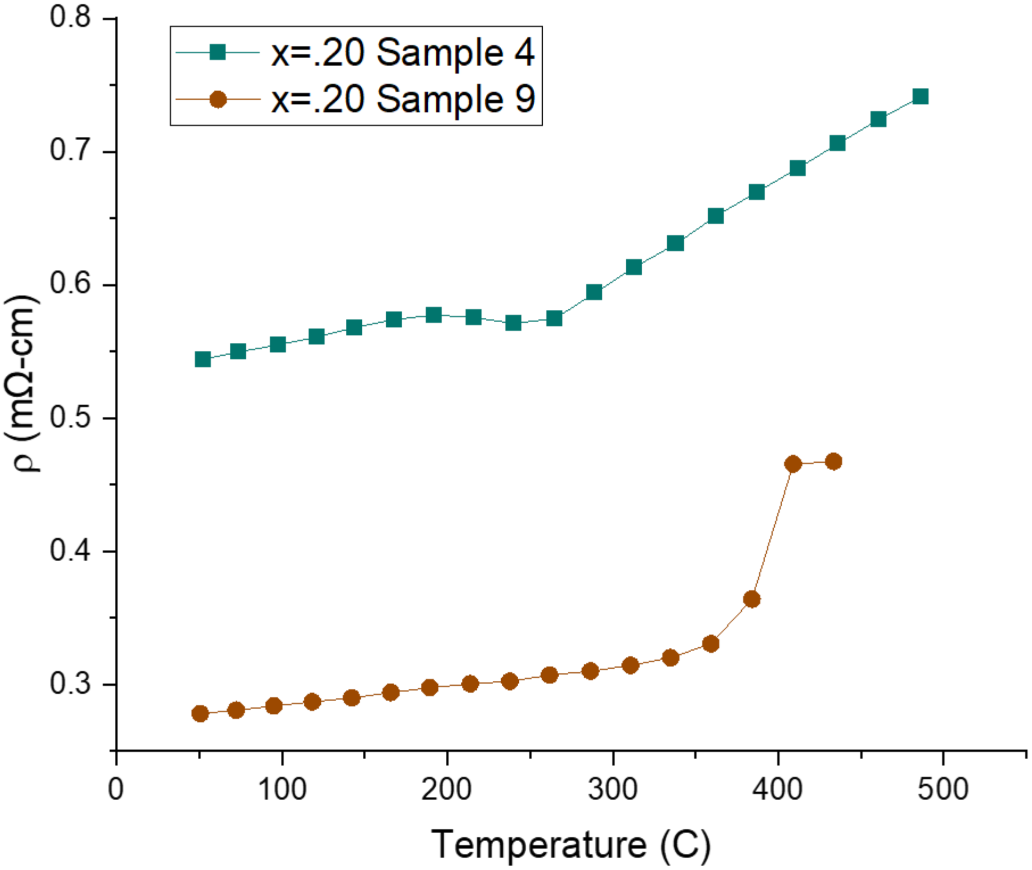

Figure 5.4: Spread of resistivity values for the x=.20 samples.

In addition, the x=0.40 results had inconsistent resistivity results. Below in Figure 5.5 the differences are shown quite starkly. While one series has a generally increasing resistivity with temperature, the other series has a pronounced negative slope indicative of semiconducting behavior. Both data sets have resistivity values well above those shown by higher concentrations of Sn, which are shown later in this section.

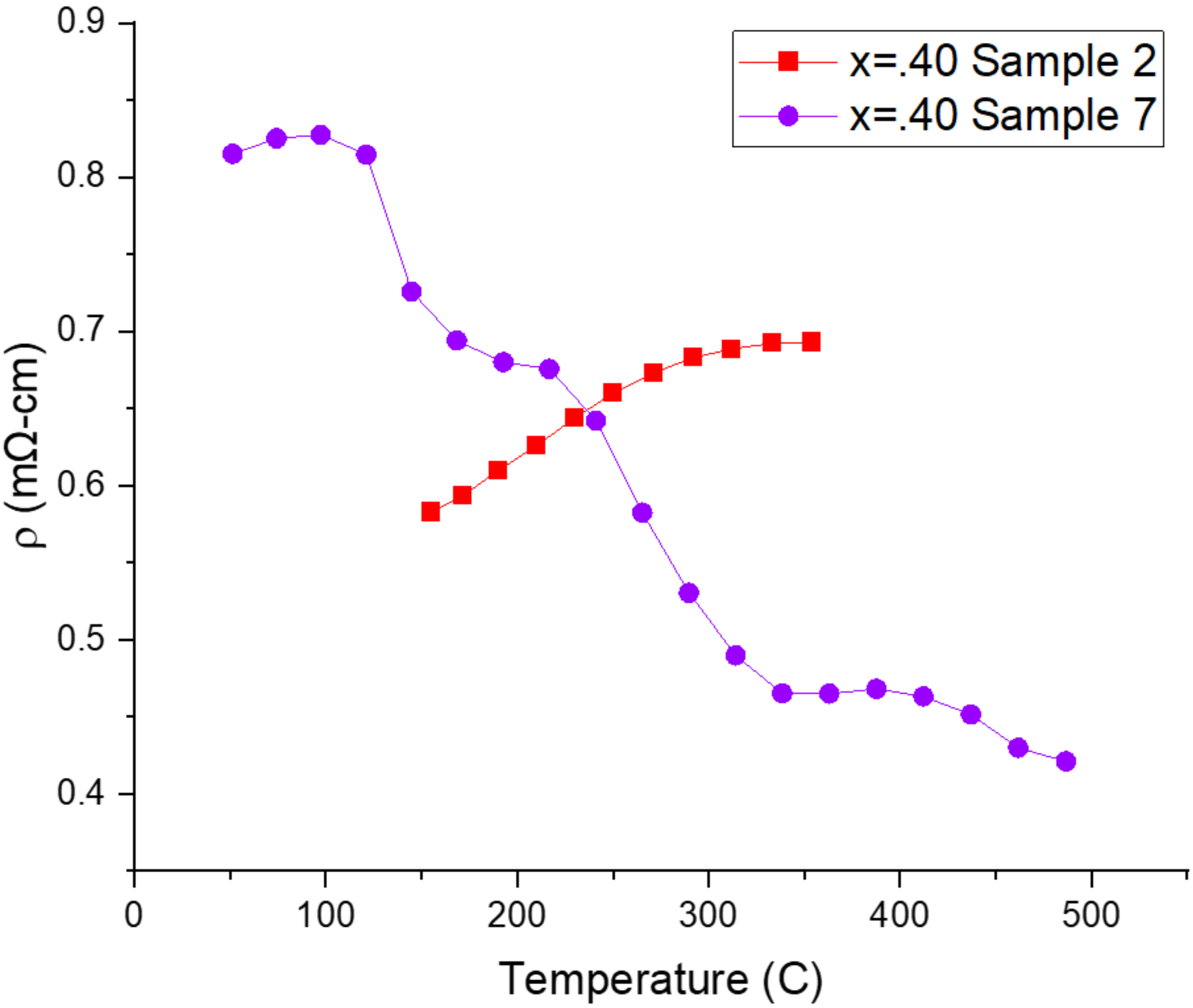

Figure 5.5: Resistivity values for x=.40 samples.

As we get closer to the Sn-rich region of the solid solution, the resistivity results are less dramatic and more well-behaved. As can be seen in Figure 5.6, the increase in Sn content causes the resistivity to level off and the values are within a similar range for samples with Sn concentrations of x=0.50 and above. As with previous samples, the rise in the resistivity with temperature is consistent with a degenerate semiconductor's behavior.

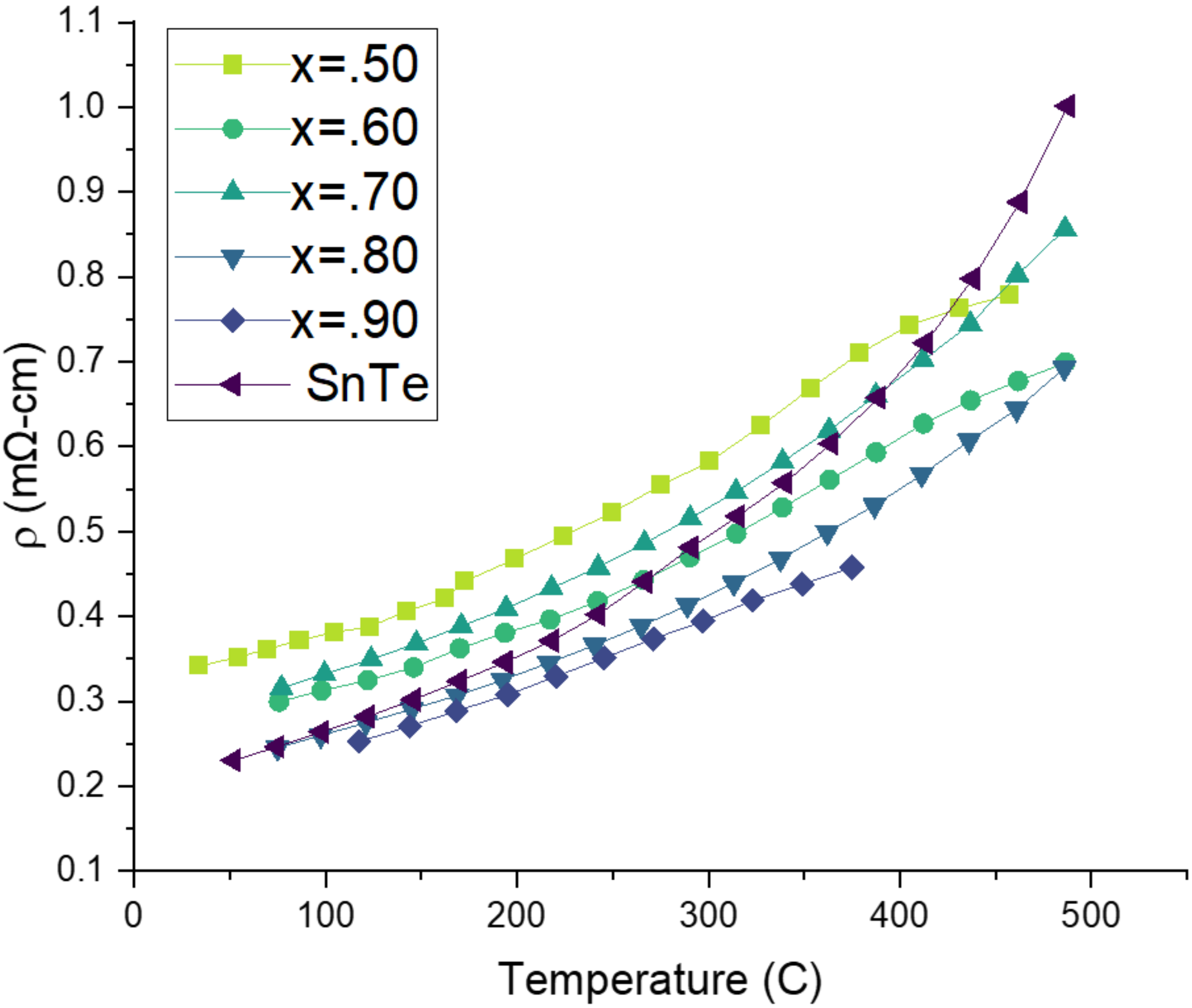

Figure 5.6: Electrical resistivity of Sn-rich samples x.50 and above up to SnTe. Note the rising resistance with temperature, a hallmark of degenerate semiconductors.

Taking together the resistivity data we can construct a figure like the one developed by Lewis *et al* for comparison. We recover a similar result where resistivity quickly rises at small amount of Sn alloying before leveling off closer to the values of the end members GeTe and SnTe, displayed in Figure 5.7. With equipment available to us data was taken up through the structural transition temperature of GeTe (approximately 400C). Data was taken upon heating and cooling, but only heating data is displayed for ease of reading. Cooling data did not significantly deviate from heating data for all resistivity measurements. Data for x=0.20 and x=0.40 are omitted due to the inconsistency in data for these compositions.

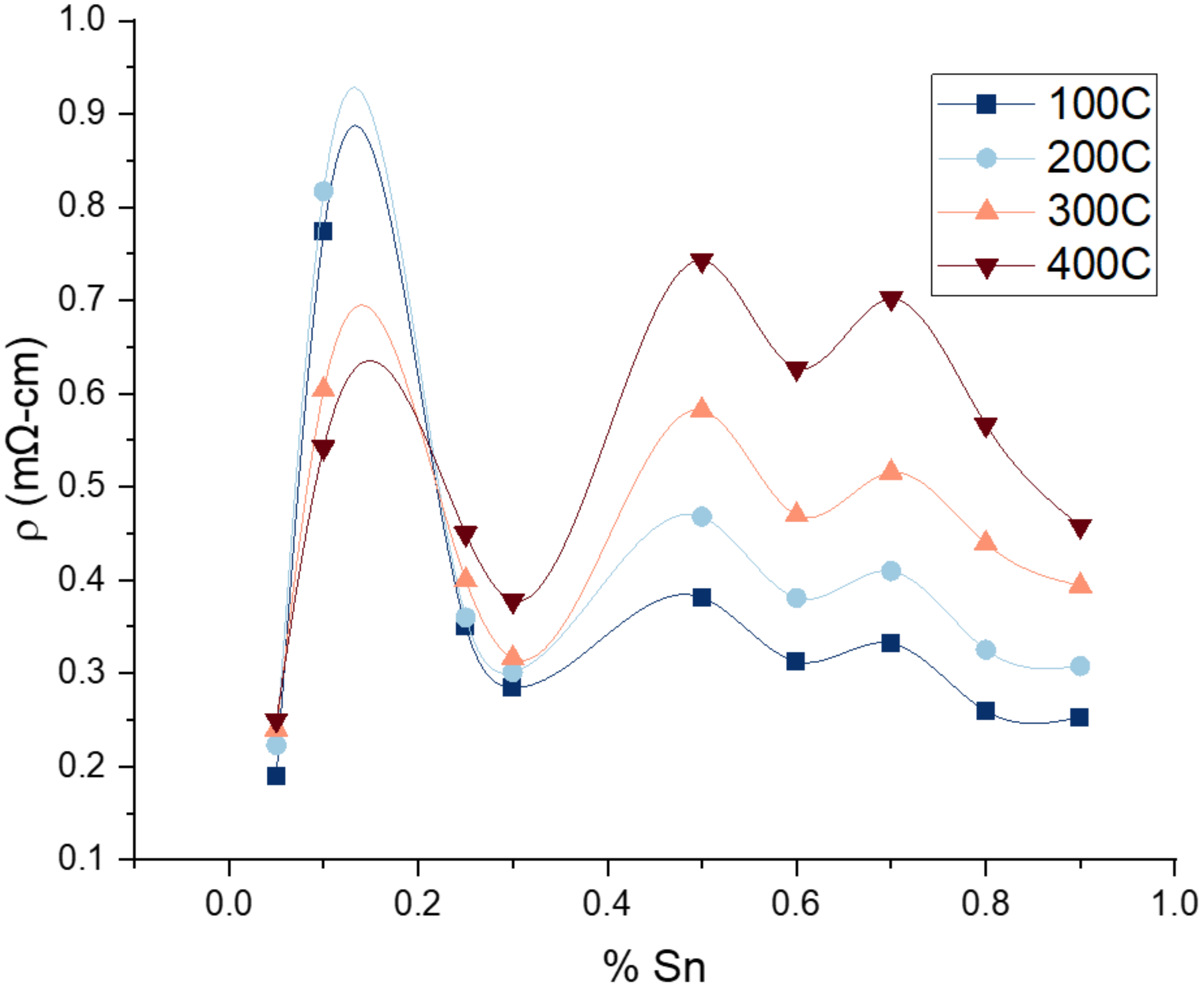

Figure 5.7: Electrical resistivity of Ge(1-x)Sn(x)Te as a function of Sn content x. Note the large increase in resistivity at low Sn concentrations. The peak in the resistivity appears to be shifting to higher Sn concentrations at higher temperatures.

5.2 Seebeck Coefficient in the $Ge_{(1-x)}Sn_{(x)}Te$ system

Closely related to the resistivity is the Seebeck coefficient, another manifestation of the electronic behavior of the system. Seebeck data for this study was measured simultaneously in a low-pressure Helium atmosphere with the resistivity data in the ZEM as detailed in Chapter 3. Measurement of the Seebeck coefficient requires a temperature gradient across the sample which was taken by two spring-loaded thermocouples pressed onto the sample, with a temperature gradient between 1- and 2-degrees C. The ZEM data collection procedure takes three measurements at three gradient values to minimize instrument noise. As the $Ge_{(1-x)}Sn_{(x)}Te$ is a *p*-type conductor, all Seebeck values are positive. In Figure 5.8, the Ge-rich samples are shown alongside the results from the GeTe measurement. As in the resistivity data, the x=0.10 series shows a dramatic fluctuation as it moves through the phase transition temperature range.

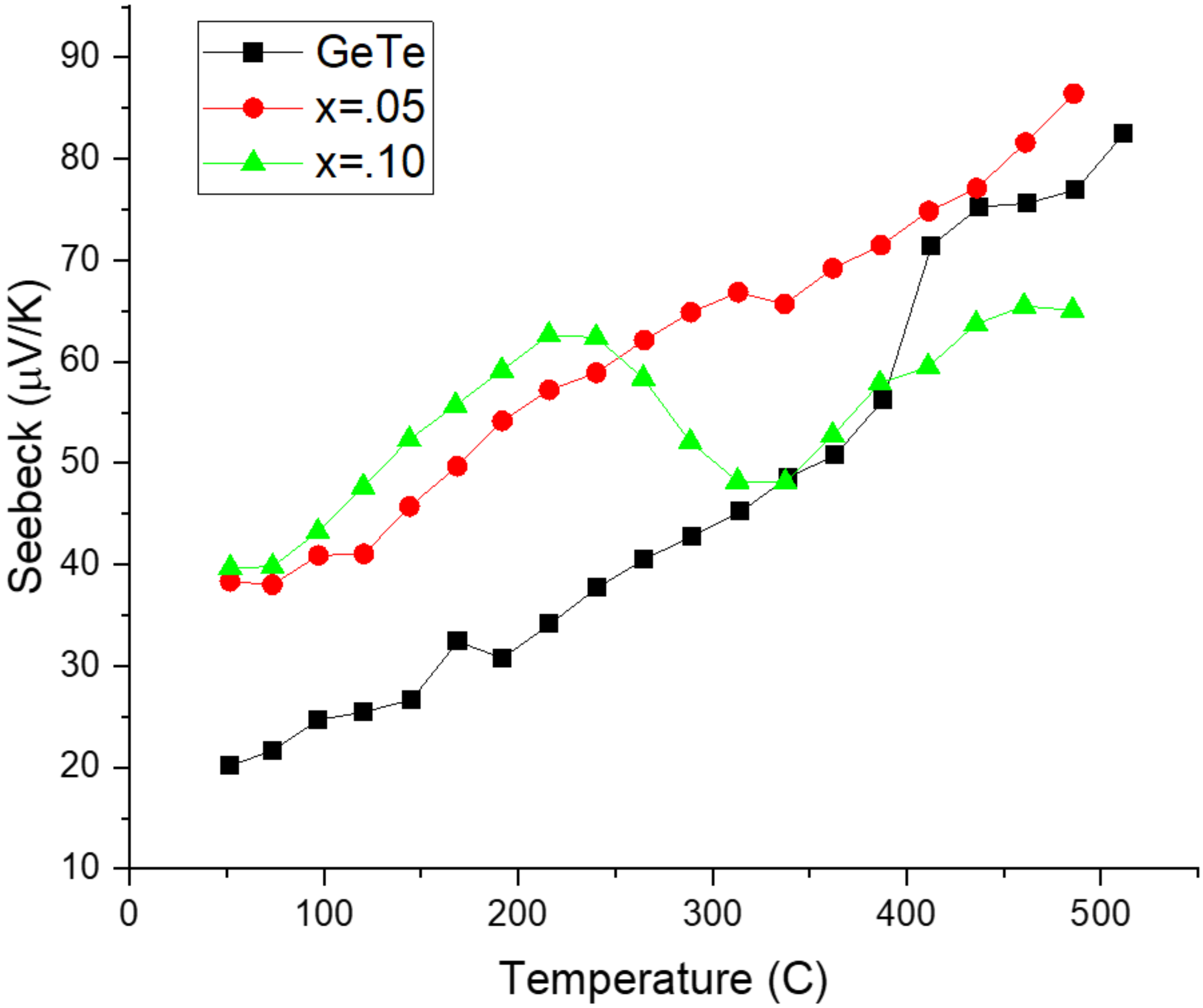

Figure 5.8: GeTe and Ge-rich sample Seebeck data. Note the discontinuities in the data near the phase transition temperatures for GeTe (~400C) and lower temperatures for x=.05 and x=.10.

While the GeTe data series shows an increase in the Seebeck value after the phase transition, the alloyed samples show a decrease. The x=.10 sample begins with a higher Seebeck than its end member GeTe at near-room temperatures, but after its structural transition has a lower value. In Figure 5.9 we can see the other Ge-rich samples that show similar, if more muted, trends.

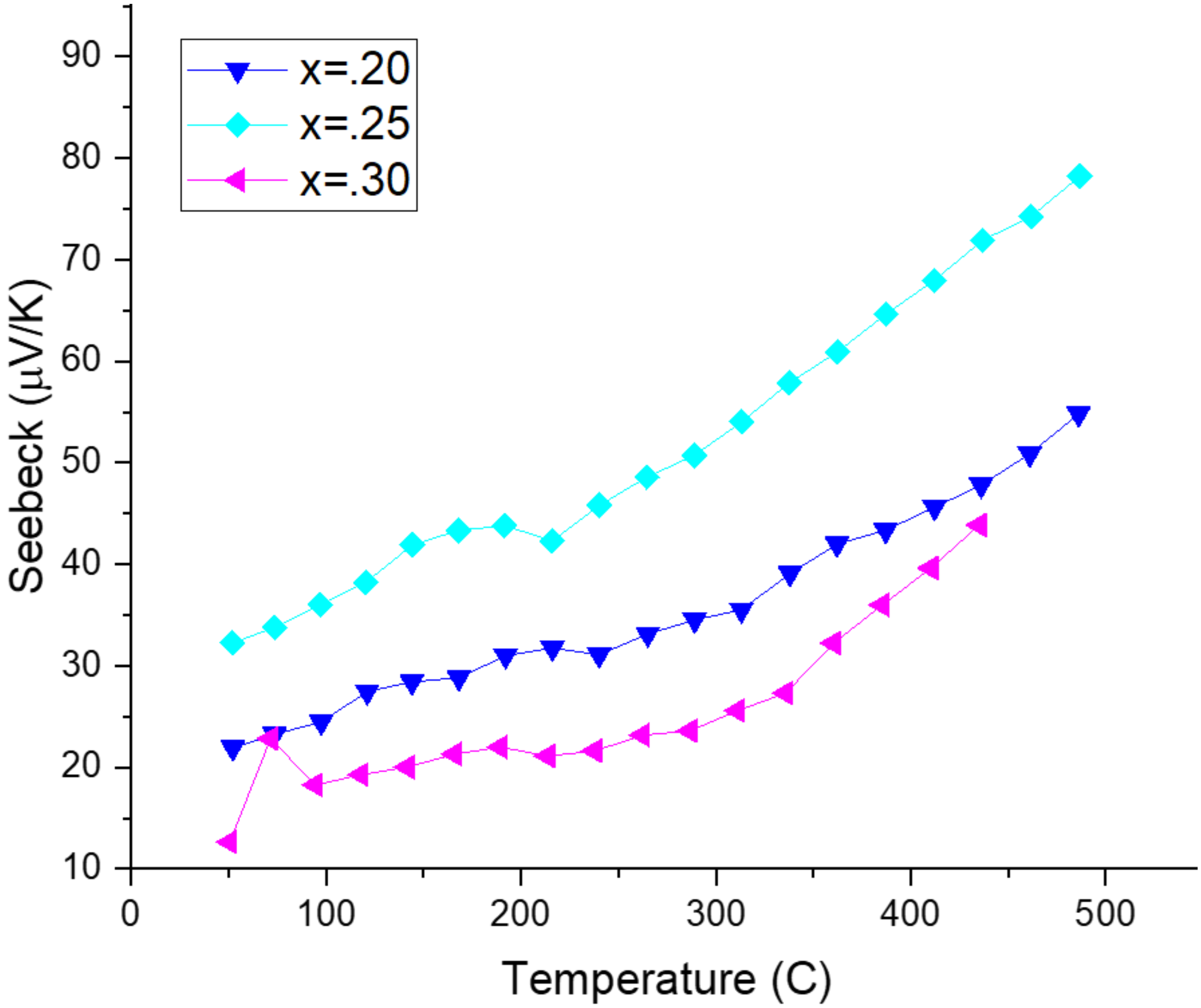

Figure 5.9: Ge-rich sample Seebeck coefficient values. The x=.25 data series shows a subtle discontinuity near the expected structural phase transition temperature.

Unlike the resistivity measurements, the x=.20 samples were consistent in their Seebeck values, but the x=.40 did show some deviation. Below in Figure 5.10 is shown two data series, which correspond to the resistivity data in Figure 5.5.

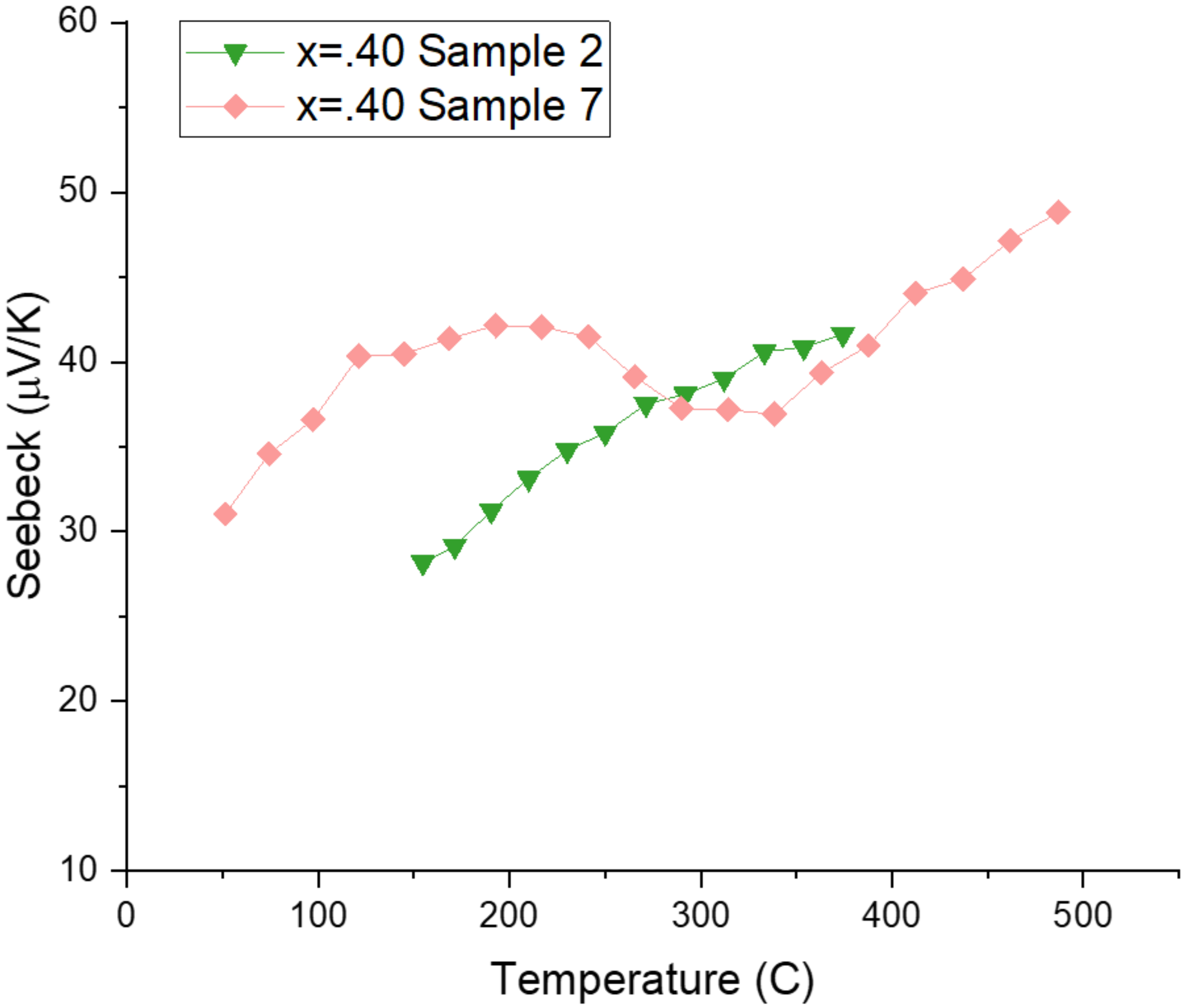

Figure 5.10: Seebeck values for two different x=.40 samples.

For the Sn-rich samples with structural phase transitions near or below room temperature, the Seebeck data shows behavior that mirrors the resistivity data and generally rises with temperature. Figure 5.11 shows Seebeck data for the remainder of the binary alloy system, which in general are higher than the values for Ge-rich samples. The x=0.60 sample had the highest Seebeck values measured in this study.

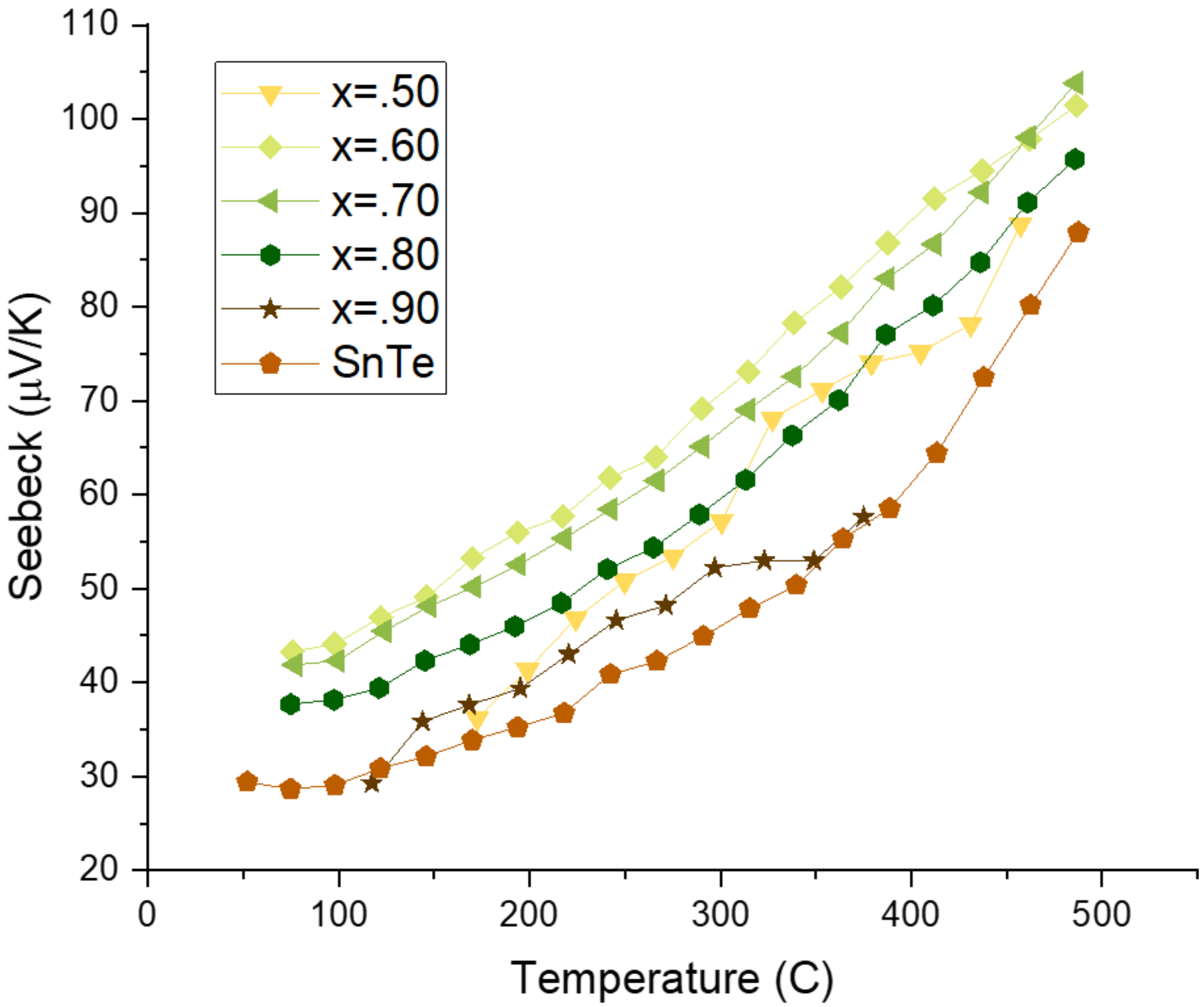

Figure 5.11: Seebeck coefficient values for Sn-rich samples. Rising values with temperature are consistent with resistivity data and suggest metallic behavior.

Armed with both Seebeck and resistivity data, we can then calculate the electronic portion of *ZT*, also known as the power factor (PF), which is the Seebeck squared divided by the resistivity. To make easier use of this data in conjunction with the thermal data below, the Seebeck units of micro-Volts per Kelvin and the resistivity units of milli-Ohm centimeter have been converted to the SI standard units of Watt per meter Kelvin squared (W/mK^2). Often the power factor is expressed in term of micro-Watt per centimeter-Kelvin (μW/cmK), and a "good" thermoelectric will have a power factor in the range of 20-40 μW/cmK. As can be seen, the electronic portion of the performance is far from optimized, but is still reasonably good with the best samples in the 15-20 µW/cmK range at the highest temperatures. With similar Seebeck values to the others in the series but with the lowest resistivity, the x=.05 sample showed the highest power factor. Germanium-rich power factors are shown below in Figure 5.12, while the Tin-rich power factor calculations are shown in Figure 5.13 with the same scale for comparison.

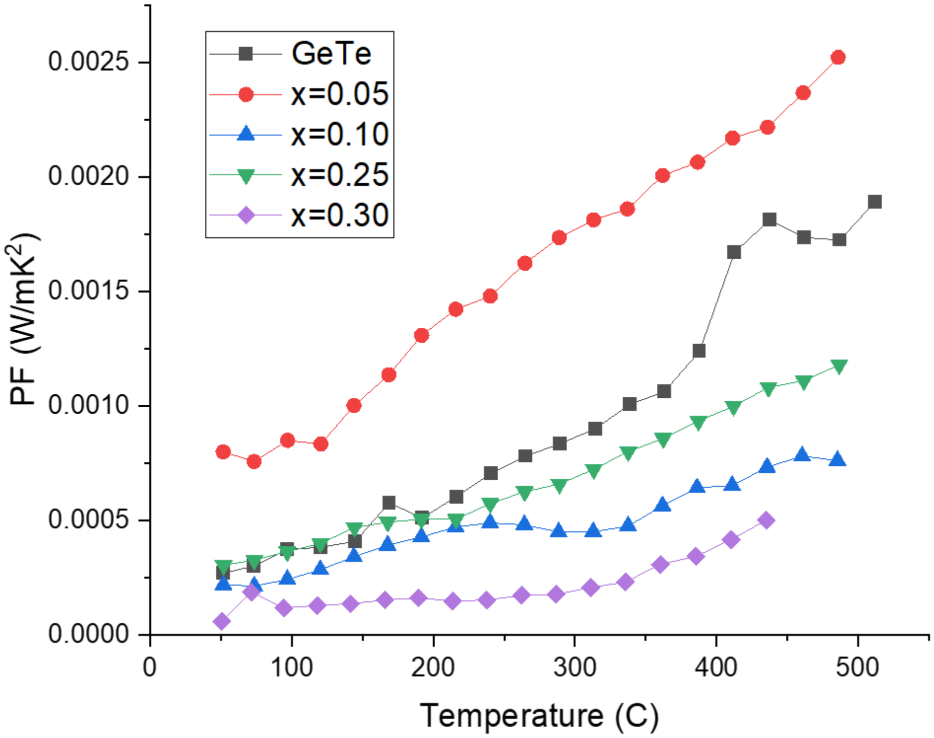

Figure 5.12: Power factor calculations for Ge-rich samples

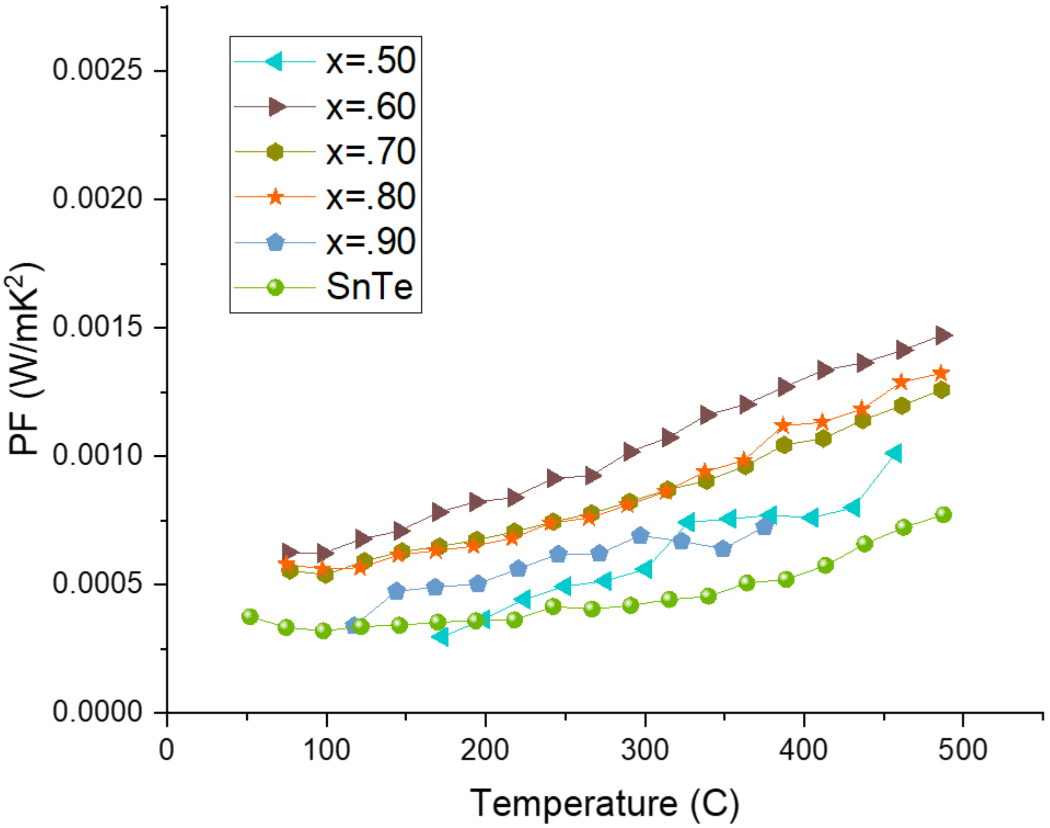

Figure 5.13: Sn-rich power factor calculations

While the x=.05 was the highest performer, GeTe was a close second, with x=0.60 coming in third. In contrast, the lowest performer was the x=0.30 sample, as it had among the lowest Seebeck values as well as a middling resistivity. Even so, none of the data series suggests that any of these samples would exhibit a high ZT ("high" in this context meaning approaching a ZT value of 1) on their own. Rather, these values can serve as a starting point to determine how to best optimize this system for a high ZT, namely tweaking the carrier concentration to increase the Seebeck coefficient while maintaining a relatively low resistivity. What is also notable is how the power factor of GeTe increases as it transitions from a rhombohedral to cubic structural phase. In this case this is driven by the increase in the Seebeck coefficient, as the resistivity also rises at that temperature which lowers the power factor.

5.3 Carrier concentration and mobility via Hall effect

Measurements for carrier concentration and mobility were carried out for a small number of samples that had otherwise undergone full characterization. Samples were thinned to the smallest possible extent, 0.2-0.5mm, and mounted in a custom-built Hall Effect Magnet and subjected to 1.6 T of magnetic fields in both directions at room temperature to determine carrier concentration as described in Chapter 3. Using known sample dimensions and magnetic field strength, carrier concentrations were calculated using the standard relation between Hall voltage and applied current as detailed in Chapter 3. The carrier concentration is shown with a logarithmic scale on the y-axis below in Figure 5.14. A table with all the values of carrier concentration, mobility, and sample resistivity are shown in Table 5.1. Samples mounted on the Hall stage showed a slight increase in resistivity compared to ZEM data, but were within the same order of magnitude.

Sn content 'x'	ρ (mΩ-cm)	$p(10^{20})$	μ ($cm^2V^{-1}s^{-1}$)
0.1	0.619	30	3.5
0.2	0.621	23	4.3
0.3	0.727	6.8	12.7
1	0.13	2.1	298

Table 5.1: Data from Hall measurements. Note the large increase in mobility (μ) and decrease in carrier concentration (p) with the addition of Sn.

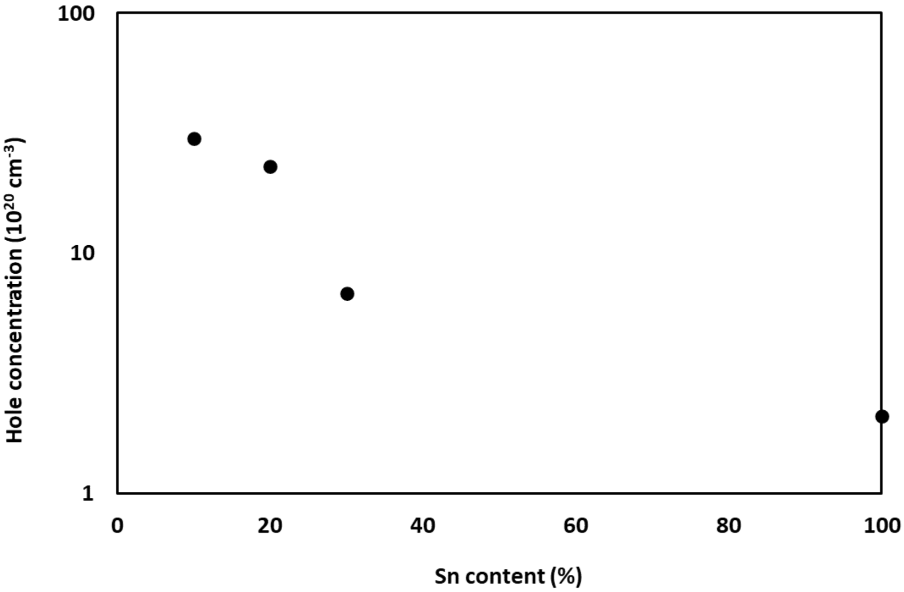

Figure 5.14: Carrier concentration from Hall measurements- note the logarithmic scale. Sn content decreases carrier concentration dramatically.

With a measurement of the carrier concentration, a calculation for the carrier mobility was made possible and is reported below in Figure 5.15. While we saw a ‘hump’ in the carrier concentration data, the mobility data shows a more striking rise in mobility with the inclusion of more Sn. Our sample of SnTe showed the highest mobility of all measured samples with a value of nearly 300 cm^{-2}V^{-1}s^{-1} compared to a value of 3.5 cm^{-2}V^{-1}s^{-1} for the x=0.10 sample.

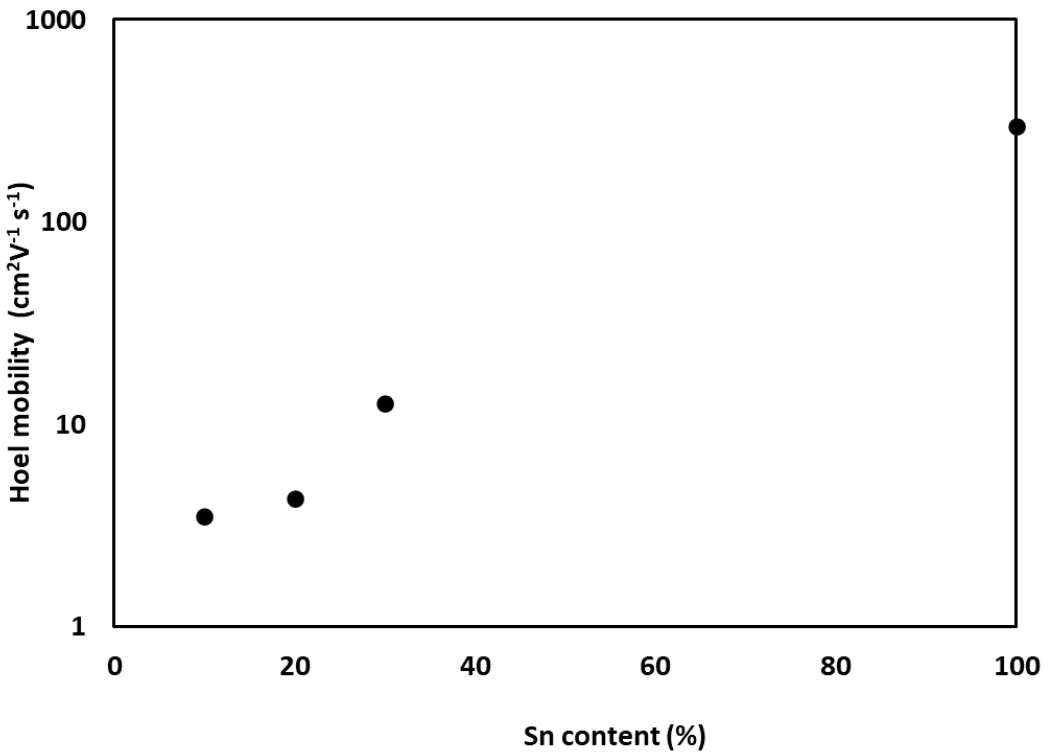

Figure 5.15: Carrier mobility calculated from Hall data. Note the sharp rise in mobility as Sn content increases.

These two sets of information lend us a way to understand the trends observed in the resistivity data. While the carrier concentration data alone might suggest the x=0.10 sample would be more conductive than say SnTe, by virtue of having more carriers, we see here how the mobility increase with increasing Sn content explains in part how the x=0.10 sample in fact had the lowest electric conductivity (highest resistivity, see Figure 5.7).

5.4 Discussion of Electronic Properties

The effect of Ge/Sn vacancies on the transport behavior of these alloys proves to be among the dominant mechanisms observed in this study. Much like the study by Lewis et al, we observed an initial sharp rise in the resistivity of samples as Sn was alloyed on the Ge site. As substitution of Sn for Ge is isovalent, absent of defects we might not expect to see much in the way of differences in transport behavior but here we see substantive differences. As can be seen in Figure 5.7, there is a sharp rise in the resistivity, especially the x=0.10 sample, before it drops off again much like the figure reported by Lewis et al. The behavior of GeTe as a p-type semiconductor is attributed to the vacancies of the Ge site, which each vacancy providing a net +2 charge. Here we see the effect that with a substitution of small amounts of Sn, these vacancies can be filled by Sn atoms hence removing the effects of these +2 sites in the lattice, resulting in a decrease in hole concentration. This is supported by the information provided in the calculations for carrier mobility, as Sn filling a Ge site will cause a sharp rise in the mobility. Other studies [39,42] show that in vacancy suppressed GeTe the mobility values increase by an order of magnitude, suggesting that Ge vacancies come at a high cost to the carrier mobility. Studies by Dong [42] showed that by suppressing vacancies in GeTe, they were able to improve the mobility to 90 $cm^2 V^{-1} S^{-1}$. Our Hall measurements in Figures 5.14 agree with this notion, as we observe a more than one order of magnitude reduction in hole concentration in SnTe compared to lightly doped GeTe. At the same time, the hole mobility (Figure 5.15) rises dramatically with Sn concentration, a clear sign that scattering of holes by vacancies is strongly diminished. The net result on the resistivity is the competing concentration and mobility dependencies shown in Figure 5.7 - an initial rise in resistivity as hole concentration diminishes, and a strong decrease in resistivity at high Sn concentration as the mobility rises to several hundred $cm^2 V^{-1} S^{-1}$.

CHAPTER 6 THERMAL TRANSPORT EFFECTS AND THERMOELECTRIC FIGURE-OF-MERIT

6.1 Total Thermal Conductivity in the $Ge_{(1-x)}Sn_{(x)}Te$ system

In practice, the thermal conductivity measurements were taken before the electrical measurements because the measurement technique has the strictest parameters in terms of sample geometry and to minimize the effect of thermal cycling on thermal conductivity data. As prepared in the way detailed in Chapter 3, 10mm round samples 1-2mm thick of known density were loaded into a Netzsch Laser Flash Analysis (LFA) for measurement. The LFA measured thermal diffusivity directly and when combined as a product with the sample density and the heat capacity the resulting thermal conductivity was calculated. Sample densities and heat capacities are detailed in the Appendix. When possible multiple samples from the same original ingot were measured and what follows is a representative sample of the available data. A select number of samples were run twice or three times in the LFA to check for consistency and no significant deviations were observed. Below in Figure 6.1, the same sample of GeTe is shown with two subsequent measurements on heating and cooling. 15

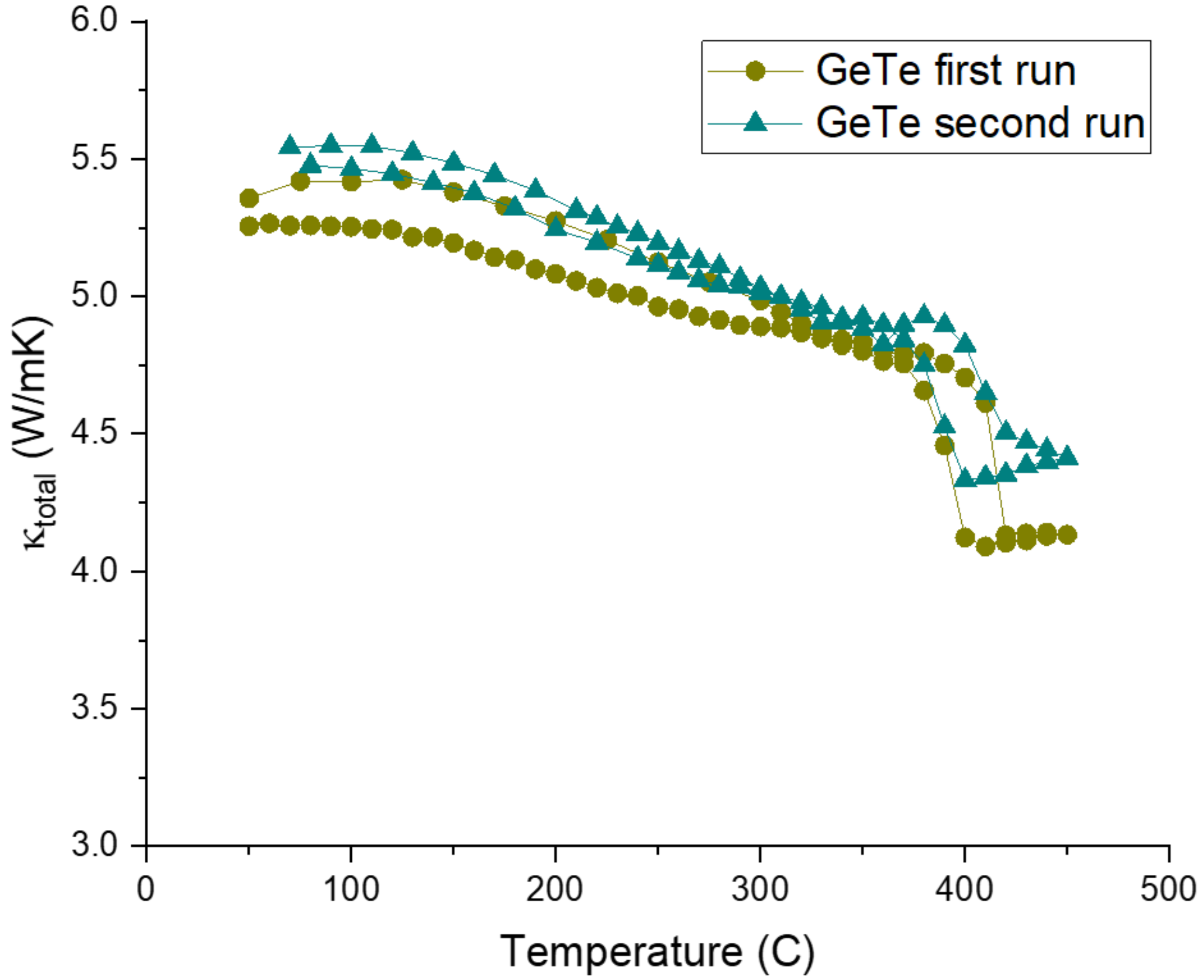

Figure 6.1: Two subsequent thermal conductivity measurements on the same sample of GeTe on heating and cooling. Note the rapid, reversible dropoff in thermal conductivity at the phase transition temperature ~400C. The bottom curves in both series represent the heating portion.

What is remarkable in Figure 6.1 is the magnitude of the change in thermal conductivity right at the structural transition temperature, about 0.7 W/mK. This reduction in thermal conductivity is also quickly reversible in temperature, and as evidenced above is easily reproducible. As will be seen below, other samples in this alloy system did have thermal conductivity increases in the temperature range of the structural transition. This phenomenon was seen across multiple samples of GeTe synthesized for this study, and Figure 6.2 shows different samples of GeTe. There was some ingot-to-ingot variability in the thermal conductivity values for GeTe, but samples from the same ingot showed similar values. What is remarkable is that five samples measured from three ingots of GeTe all exhibit similar drops in thermal conductivity at the transition temperature. This drop in thermal conductivity was significant and reproducible in several samples from different ingots. This drop was on the order of 1 W/mK and reversible, and on cooling the thermal conductivity mirrored that of the heating data in a manner similar to that shown in Figure 6.1.

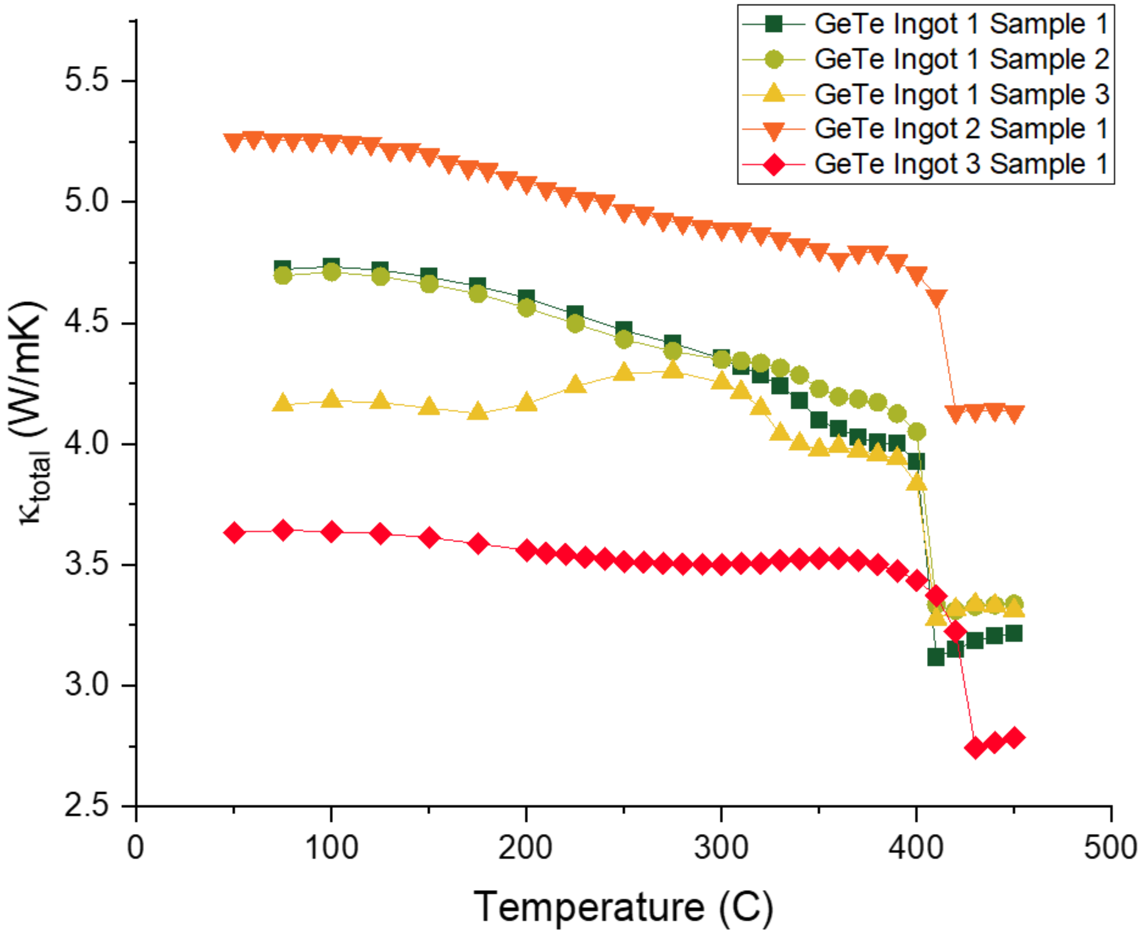

Figure 6.2: Ingot variability in the values of total thermal conductivity of GeTe upon heating. All samples show a distinct drop in thermal conductivity in the vicinity of the structural phase transition temperature of 400 °C. There was some variability in values between ingots on the order of 1-2 W/mK.

As one more piece of contrast, below in Figure 6.3 is similar in concept to 6.2 but instead for samples of SnTe. As this material does not undergo a structural phase transition, we do not observe any discontinuities and we see the durability of these samples and the reproducibility of these measurements. What is shown are three data sets: the first two are the same sample of SnTe made via direct fusion as described in Chapter 3 and the third data set is a sample manufactured from commercial-bought SnTe powder using the same SPS procedure. This was initially done to check for the effects of oxidation in our source elemental powders on thermal conductivity, as been proposed by Isotta et al [108]. and this result shows little deviation from the performance of commercially available powders.

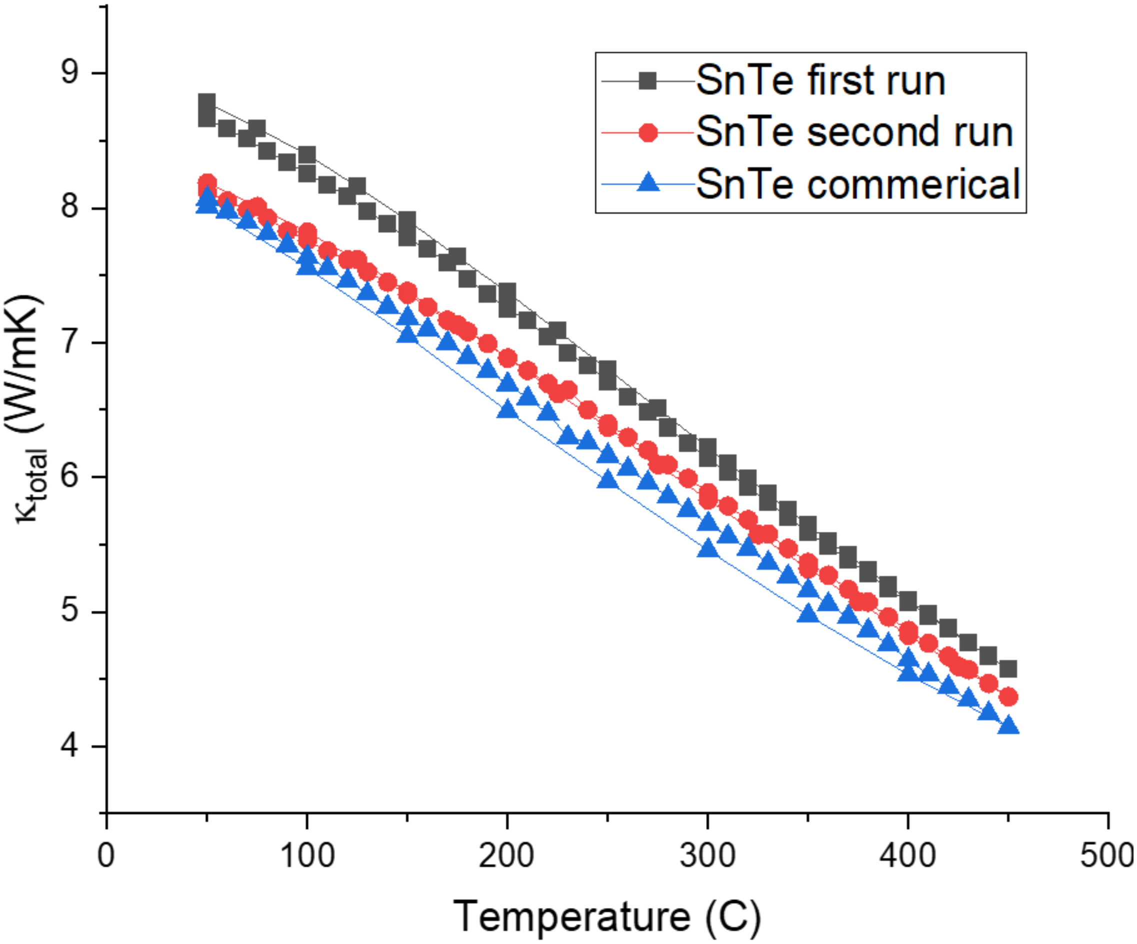

Figure 6.3: Thermal conductivity of SnTe made via direct fusion and commercially available powders on heating and cooling. The more frequent data set represents the heating data.

In addition to having a higher thermal conductivity than GeTe, the SnTe samples also demonstrate a distinct negative slope with temperature while the GeTe (before the transition) remains much flatter. Even with this negative slope, SnTe remains at a higher thermal conductivity than GeTe at all temperatures. It makes sense that GeTe has a slightly lower thermal conductivity than SnTe, because the cation-anion mass differences are greater in GeTe and here we see also that the more complex unit cell of the GeTe structure (below the phase transition) contributes to stronger phonon scattering and in sum a lower thermal conductivity.

With the performance of the end members firmly established we move now to examine the performance of Ge-rich alloys. In Figure 6.4 we see that as we move away from GeTe, the total thermal conductivity falls off from the values of GeTe, and we also observe discontinuities as these samples move through the structural phase transition. Taking the intermediate data for GeTe, we can see that with the smaller concentrations of Sn, the increase in Sn content reduces the total thermal conductivity. What is also notable is how the samples in Figure 6.4 have thermal conductivities that are nearly temperature independent.

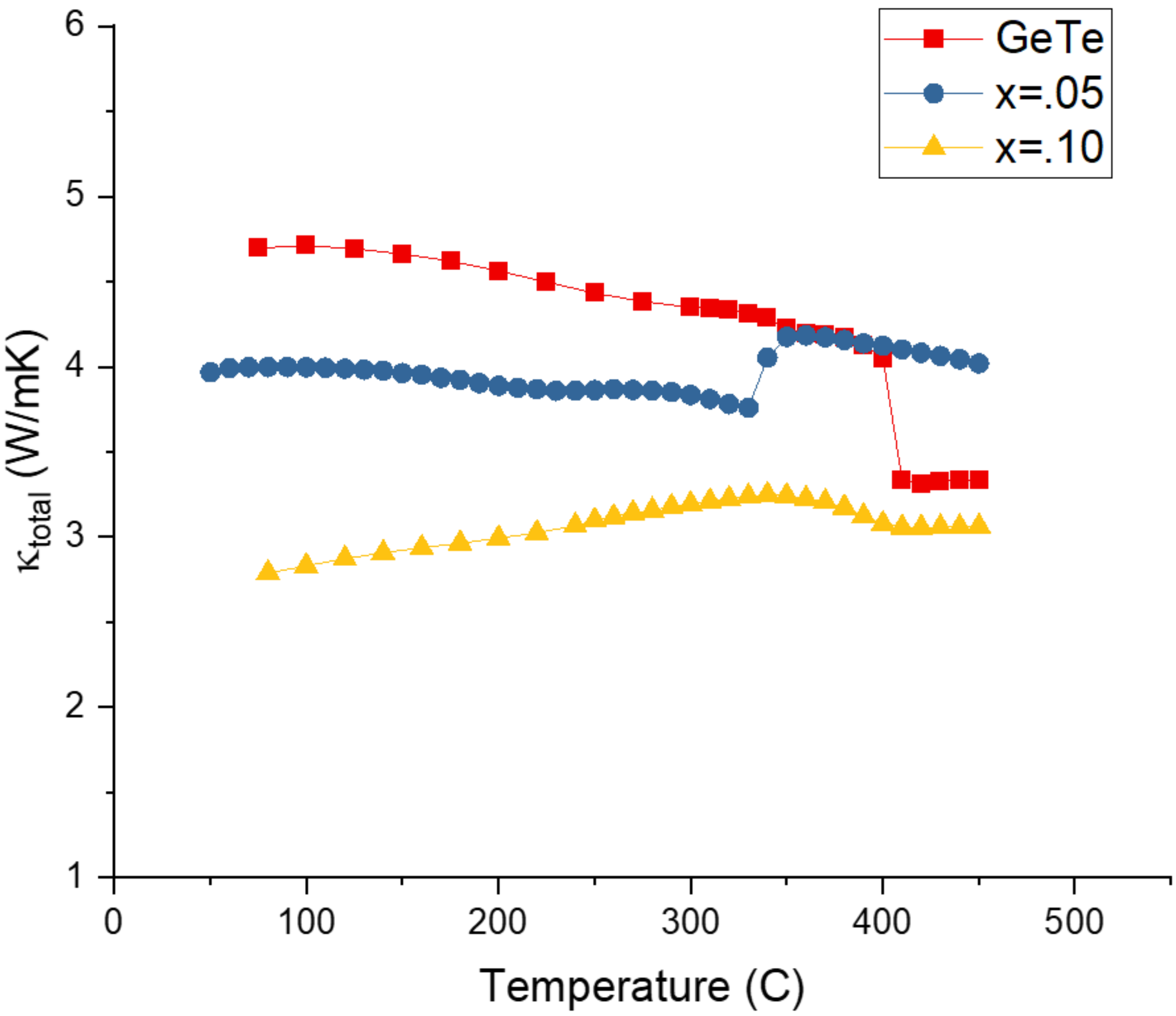

Figure 6.4: Thermal conductivity for Ge-rich samples. Note the total decrease in the total as we move away from the end member GeTe, as well as the weak temperature dependence.

While we observe a decrease in the total thermal conductivity for GeTe and x=0.10, the x=0.05 sample has a sharp *increase* at 350° C. The trend of decreasing thermal conductivity with the addition of Sn is consistent with a mixed-crystal system exhibiting alloy (i.e., mass-difference) scattering. In addition, the temperature at which the structural transition occurs is shifted to a lower temperature, sharply displayed in the x=0.05 data and smoother for the x=0.10. Much like the above data from the electrical measurements in the ZEM, some concentrations of Sn in the range of x=0.20 to x=0.30 showed variability that could not be resolved between multiple measurements. Below in Figure 6.5 we report the data from three different samples of the x=0.20 Sn concentration.

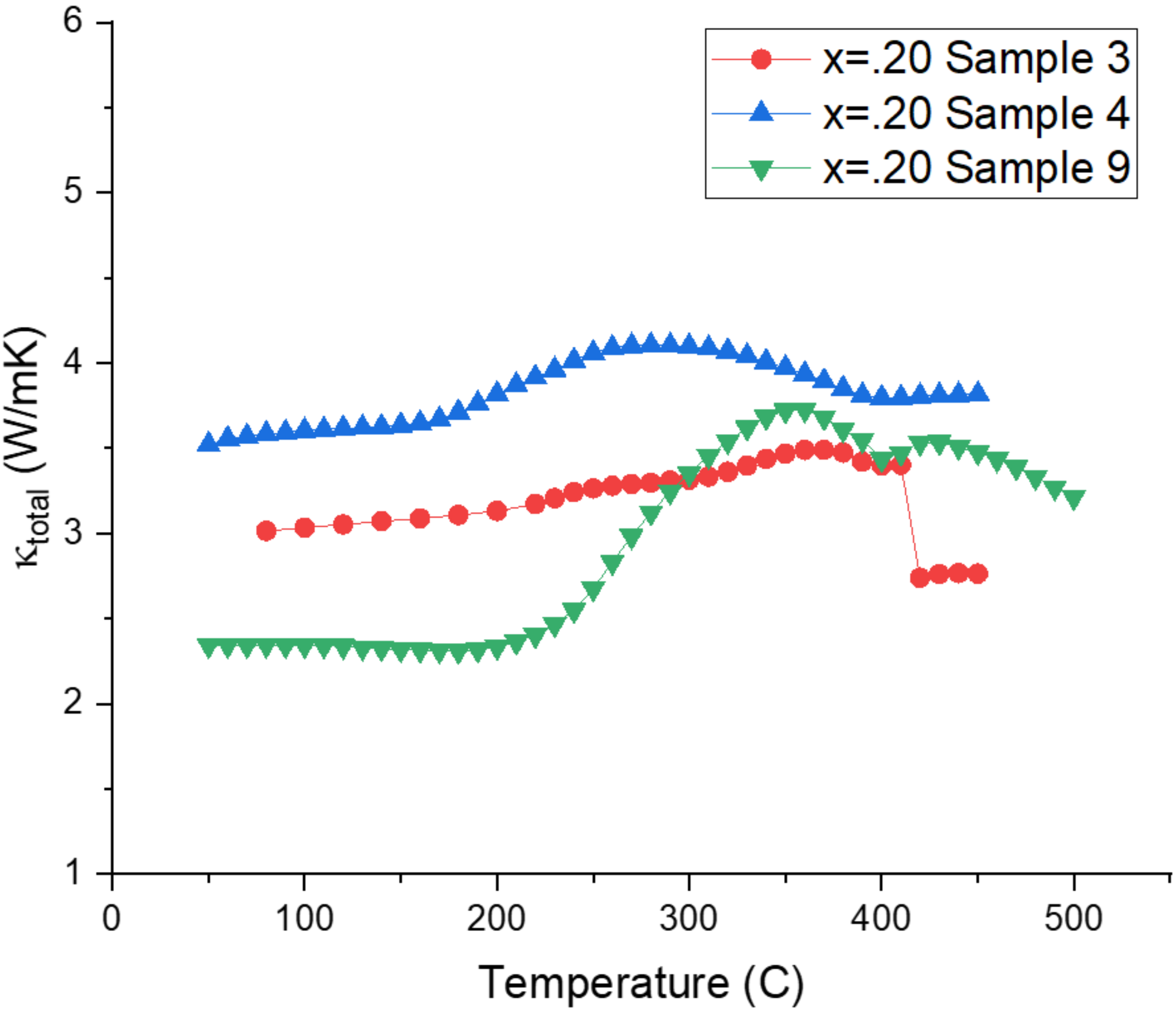

Figure 6.5: Thermal conductivity upon heating of x=.20 samples from three different samples. All samples show increases in thermal conductivity with temperature, before a negative step or slope at elevated temperatures.

While the absolute values varied between samples, the undulating curvature of the three data sets points to the structural phase transition affecting the total thermal conductivity. We estimate this transition at 300 ±25 ° C, which is consistent from our high temperature XRD analysis putting the x=0.25 transition at about 230 ° C, knowing that the x=0.20 transition temperature must be at a higher temperature. After this transition the total thermal conductivity decreases or flattens out. The large spread of the curvature, as opposed to the step seen in the GeTe data, is suggests a more gradual transition between 'rhombic' and 'cubic' behavior. It is hard to say definitively if the x=0.20 samples are at a higher or lower thermal conductivity than that of the x=0.10 sample, so there may be competing mechanisms driving this behavior beyond alloy scattering. Similarly, the x=0.25 and x=0.30 samples measured also had some variability in measurements. Below in Figure 6.6 are displayed the data collected for both x=.25 and x=.30 samples.

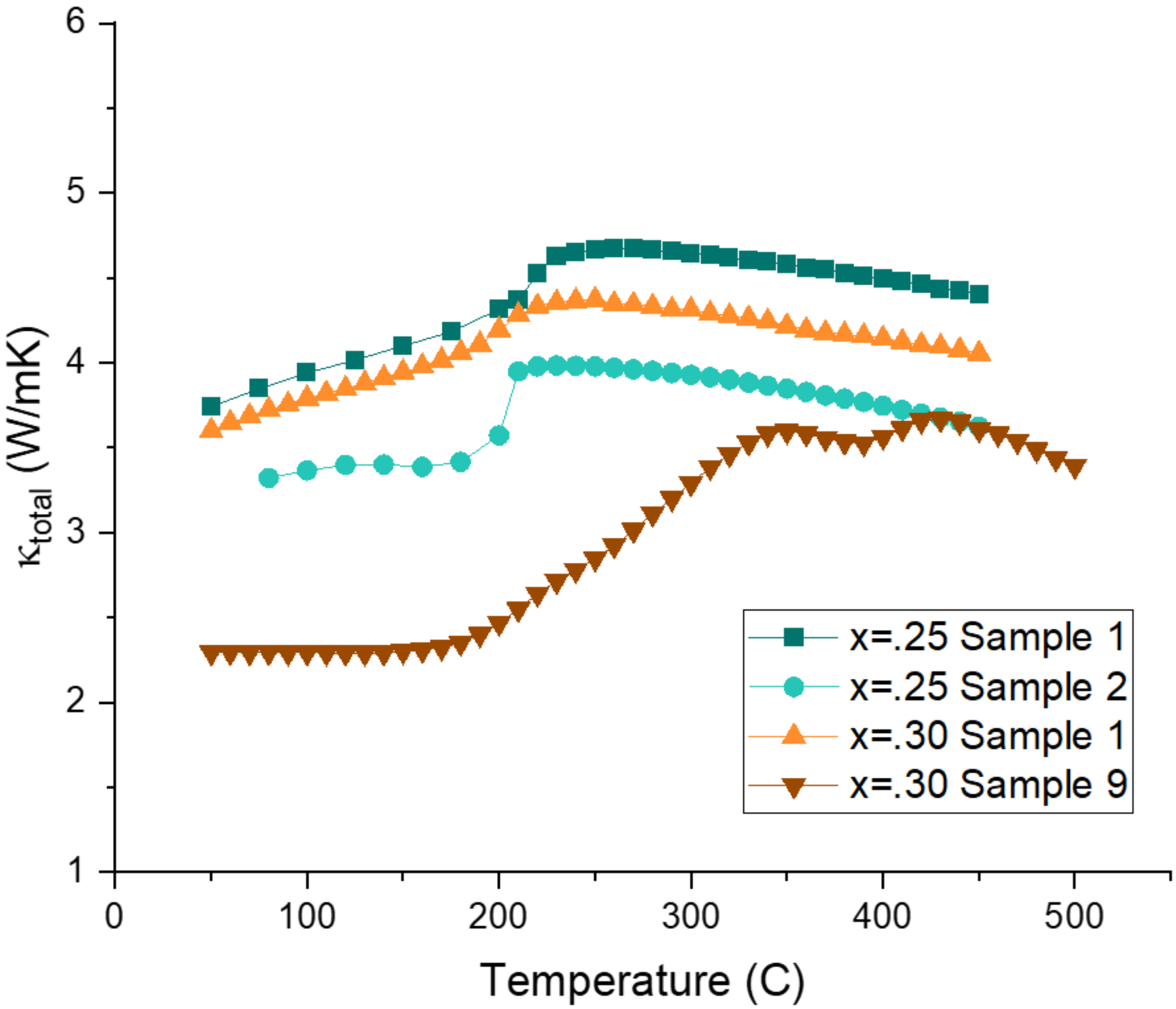

Figure 6.6: Thermal conductivity for x=.25 and x=.30 samples. Data is shown upon heating and demonstrates structural activity in the temperature range measured.

What is evidenced in the data sets for Ge-rich samples is that the structural phase transition strongly influences the thermal behavior, where the thermal conductivity rises with temperature up to the transition, and then decreases or is flat thereafter. For the x=0.25 samples, the sharp rise in the thermal conductivity closely correlates with the structural phase transition observed in the high-temperature XRD data at about 230 ° C. Like the x=0.05 sample and others below, these x=0.25 samples displayed a rise in the thermal conductivity near the transition, unlike the GeTe samples which had a sharp decrease. One x=0.30 sample also showed a very low total thermal conductivity of 2.3 W/mK slightly above room temperature, among the lowest of all samples in this study. Another sample of x=0.30 turned out very similar to the x=0.25 samples. The trend of decreasing thermal conductivity with increasing Sn content is what we would expect, with the minimum thermal conductivity to occur somewhere in the intermediate range where the effects of alloy scattering are maximized.

As was the case for the electronic measurements, thermal data for the samples with x=0.40 and above were generally more ‘well behaved’ than the Ge-rich samples. The x=0.40 data had similar values to other samples on the Ge-rich side, 3-4 W/mK ,suggesting a “bottoming-out” of the bathtub shape suggest by the Klemens model [88,90]. Discontinuities were observed in that sample as well as the x=0.50 and x=0.60 samples. As more Sn was introduced into the material, we observe a neat increase in the thermal conductivity in an ordered trend that was held through Ge-poor samples culminating in end member SnTe. Thermal conductivity data for samples with Sn content from x=.40 to x=.90 are displayed in Figure 6.7.

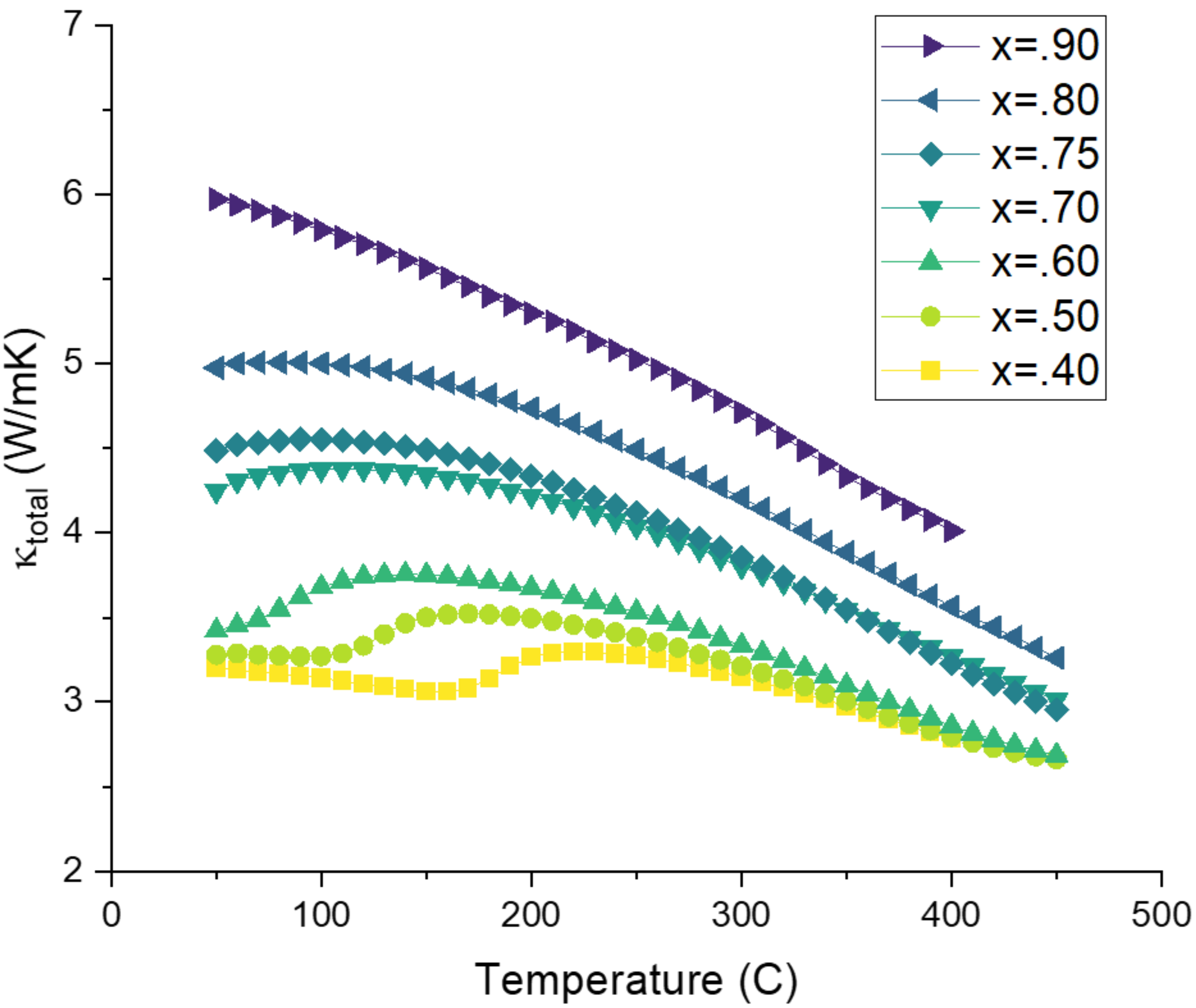

Figure 6.7: Total thermal conductivity for Sn concentrations of x=.40 and above. Note the temperature at which we observe discontinuities in the curve decreases and then disappears with increasing Sn content. This is suggestive of the structural phase transition temperature.

We see changes in curvature for the x=0.40,0.50, and 0.60 thermal conductivity curves which strongly suggests the effect of the change from a rhombohedral to a cubic crystal system. For samples x=0.40,x=0.50 and x=0.60 we see deviations in the thermal conductivity before it peaks and falls with T^{-1} dependence at higher temperatures. There is also a neat shifting of the location of these peaks, where x=0.40 sees changes in curvature about 175° C, while the x=0.50 sees a bend in the curve at 125° C. The temperature range of the x=0.50 sample curvature, between 125-150° C, agrees well with the observations of that sample from high-temperature x-ray diffraction measurements. The thermal conductivity rising continually with Sn content points towards alloy scattering as the mechanism driving these trends. As samples x=0.70 and above have predicted transition temperatures at room temperature and below, our data shows a 'rounding off' of the top of the curve, a shift of the same curve observed for x=0.50 but at lower temperatures. The general trend of decreasing thermal conductivity at higher temperatures is consistent with strong phonon-phonon scattering and we expect that trend would continue until the material approaches its melting point (~700° C) [66]. An updated structure phase diagram with thermal data in addition to structural analysis from XRD is presented in Figure 6.8.

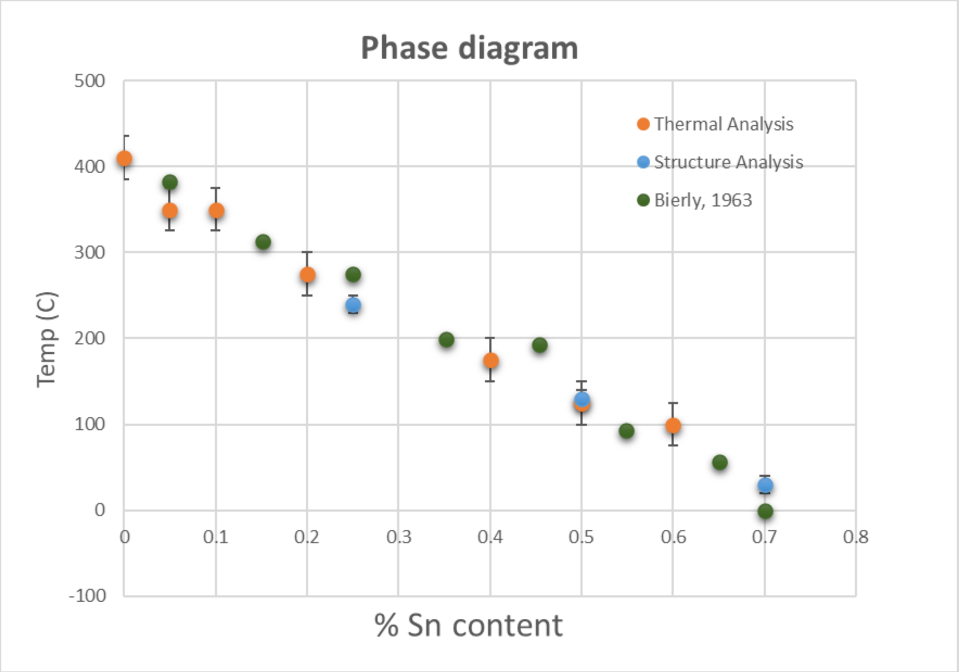

Figure 6.8: Thermal and Structural analysis of phase transition temperatures in the $Ge_{(1-x)}Sn_{(x)}Te$ system. Error bars for the thermal analysis (orange) of ±25 °C reflect the uncertainty in the thermal data.

For a more systemic look at the total thermal conductivity, Figure 6.9 was constructed to display the total thermal conductivity versus the Sn content at various temperatures. The x=0.20, x=0.25, and x=0.30 data are omitted in this figure considering the inconsistency in measured values, but were in the range of 2-4 W/mK. The general trend of the data is consistent with a system with alloy scattering as the dominant mechanism, with a the “bathtub” shape with high values for the end members GeTe and SnTe and a flat minima taking advantage of the disorder between Sn and Ge species on the cation site. What complicates this picture is the effect of the structural phase transition on this trend, as some samples (GeTe, x=0.10), saw thermal conductivities decrease while others (x=0.05, x=0.25,x=0.40,x=0.50) increased in the vicinity of the phase transition.

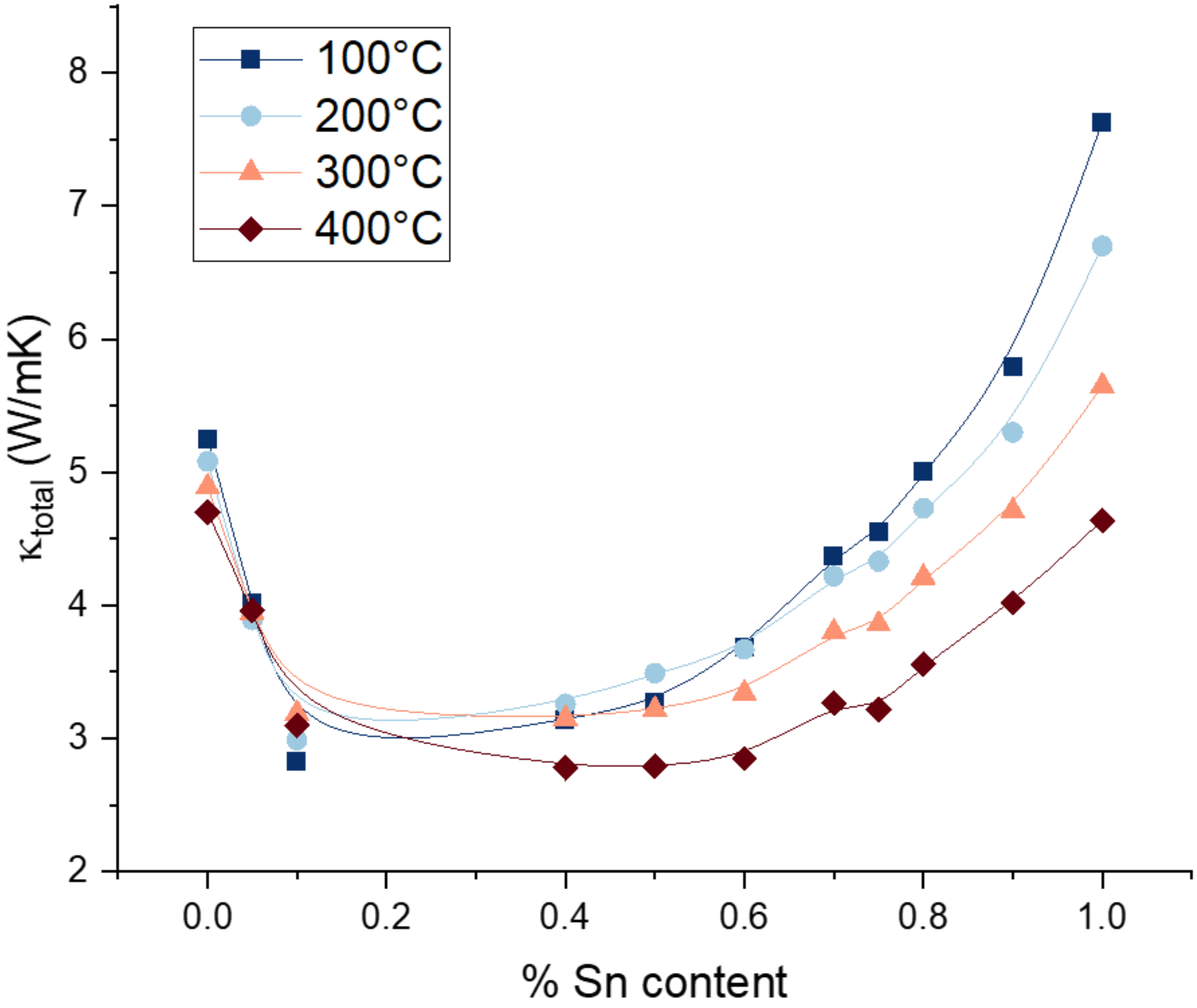

Figure 6.9: Total thermal conductivity trends displayed as a function of Sn content at various temperatures.

6.2 Lattice Thermal Conductivity in the $Ge_{(1-x)}Sn_{(x)}Te$ system

Armed with the wealth of data provided not only from the LFA system total thermal conductivity, but also the resistivity and Seebeck coefficient from the ZEM we can calculate the lattice contribution to the total thermal conductivity as a function of temperature and Sn content. As described in previous chapters, with Equations 6.1-6.3 below we calculate the electronic component thermal conductivity using the Wiedemann-Franz Law and subtracting that from the total to get the lattice thermal conductivity. Instead of using the Lorenz number (*L)* for metals, we use a formulation common in the thermoelectrics community that utilizes the Seebeck coefficient [81]. In practice samples were measured on the LFA first before being sanded into parallelepipeds for the ZEM measurement. We show in the figures below the total thermal conductivity shown above as well as the calculated values for the electronic and lattice contributions. Let us begin with the data for GeTe, below in Figure 6.10.

$$\kappa_{total} = \kappa_{electronic} + \kappa_{lattice} \tag{6.1}$$

$$\kappa_{electronic} = \frac{(L \cdot T)}{\rho} \tag{6.2}$$

$$L = 1.5 + e^{\left(\frac{-(|S|)}{116}\right)} \cdot 10^{-8} W\Omega K^{-2} \tag{6.3}$$

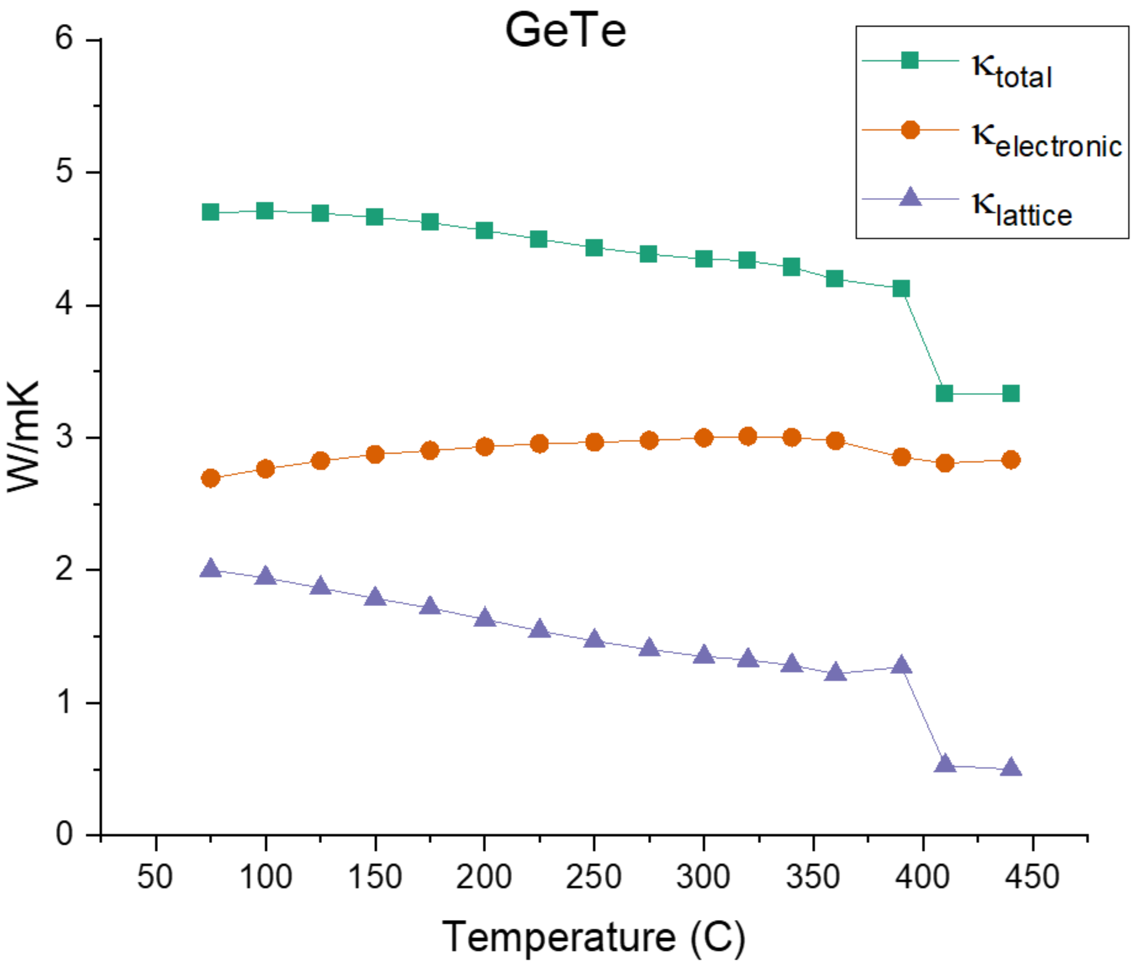

Figure 6.10: Thermal conductivity calculations for GeTe

Here we see that the rapid drop in thermal conductivity is wholly reflected as a decrease in the lattice thermal conductivity. This is strong evidence that the structural phase transition results in a softening in the lattice for cubic GeTe. Other samples showed similar drops, while others saw a rise in the lattice thermal conductivity which will be detailed below. One particularly dramatic example is shown in the x=.10 results shown below in Figure 6.11. In contrast, the results for the x=0.05 point towards a breakdown in the model resulting in unphysical lattice conductivity values.

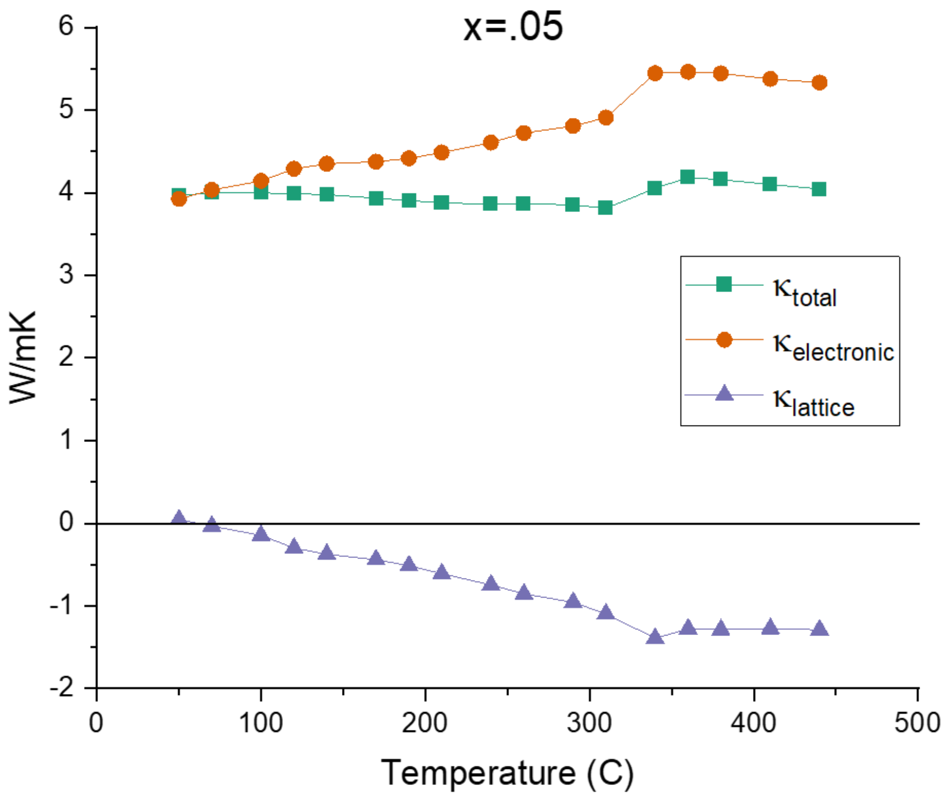

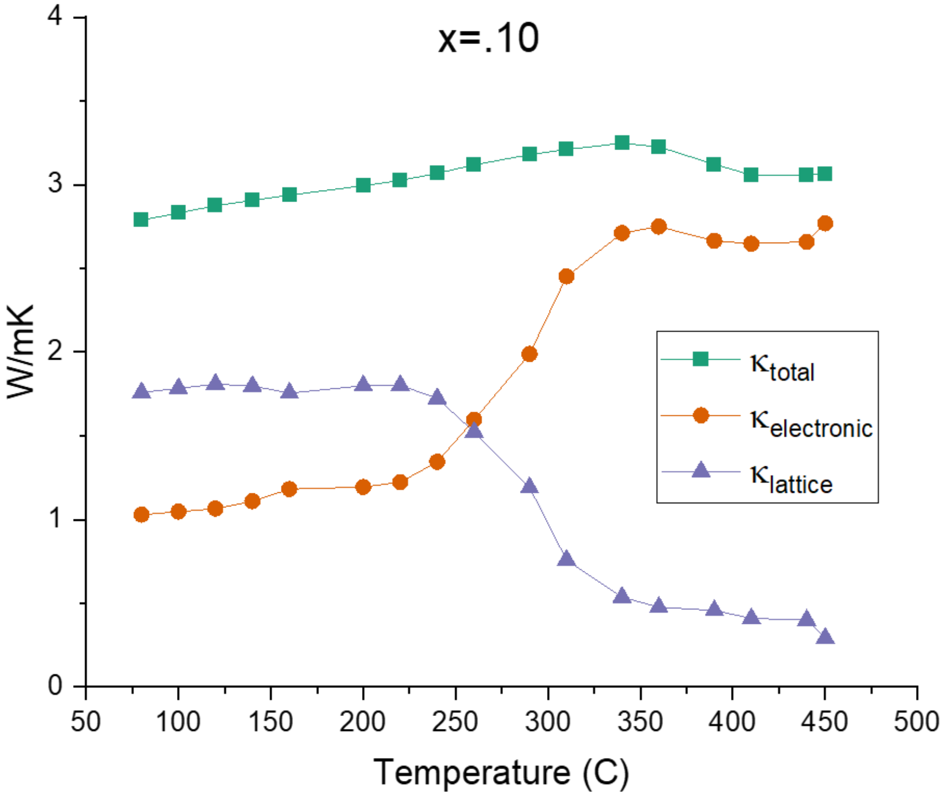

Figure 6.11: Thermal conductivity calculations for x=0.05 and x=0.10

Here in the x=0.10 case we see a rise in the electronic portion (in step with the decrease in resistivity in Figure 5.3) and consequently a decrease in the lattice thermal conductivity. The transition in the total conductivity appears to occur at almost 350 °C while the drop in the lattice curve appears almost 100 ° below this temperature. We also know well that there is a minimum lattice thermal conductivity corresponding to the amorphous limit on the order of ~0.5 W/mK so either this system has a lattice thermal conductivity near this limit, or we are pushing to the limits our application of the Wiedemann-Franz law. Given the relationship between $\kappa_{electronic}$ and electronic resistivity, highly conductive materials will push the values of $\kappa_{electronic}$ higher and higher and may result in electronic contributions whose value is greater than the total thermal conductivity measured on the LFA. We did indeed see this in several samples; the problem-child Sn concentrations of, x=0.20 and x=0.30 and to a lesser extent the x=0.05 and x=0.40 samples. Below in Figure 6.12 are two results from the two x=0.20 samples that demonstrate these non-physical results.

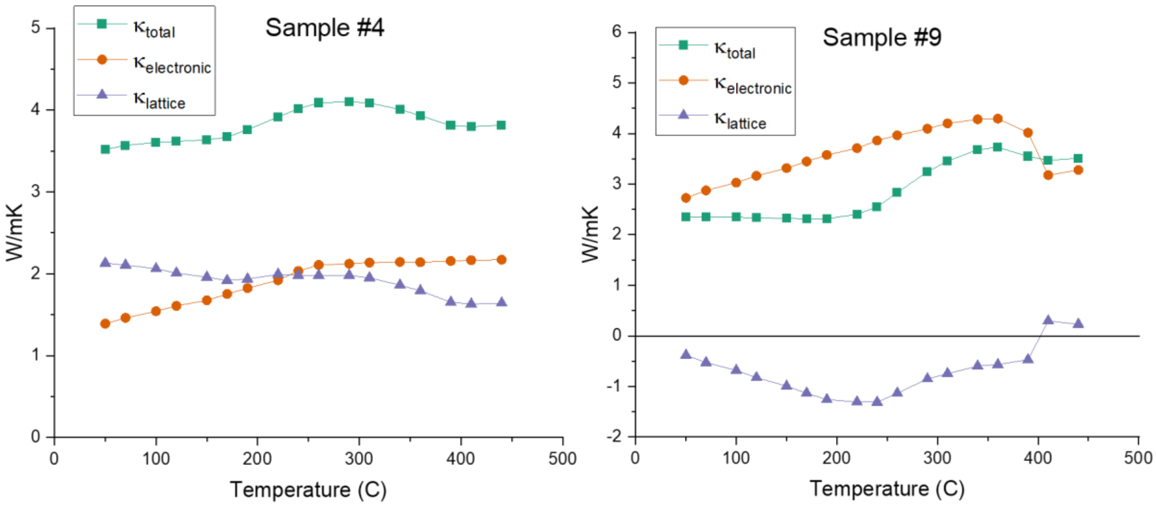

Figure 6.12: Lattice thermal conductivity calculations for two x=.20 samples. Note the non-physical results for sample 9.

As sample 9 had a lower resistivity compared to sample 4 (as shown in Figure 5.4), this difference in resistivity leads to a much higher calculated value for the electronic contribution. In this case, the calculation result was higher than our LFA results, which point towards a negative lattice thermal conductivity, which is unphysical. We saw this again in the results for the x=0.30 sample below in Figure 6.13. This data is from sample 9, as sample 1 from Figure 6.6 broke before it could be measured in the ZEM.

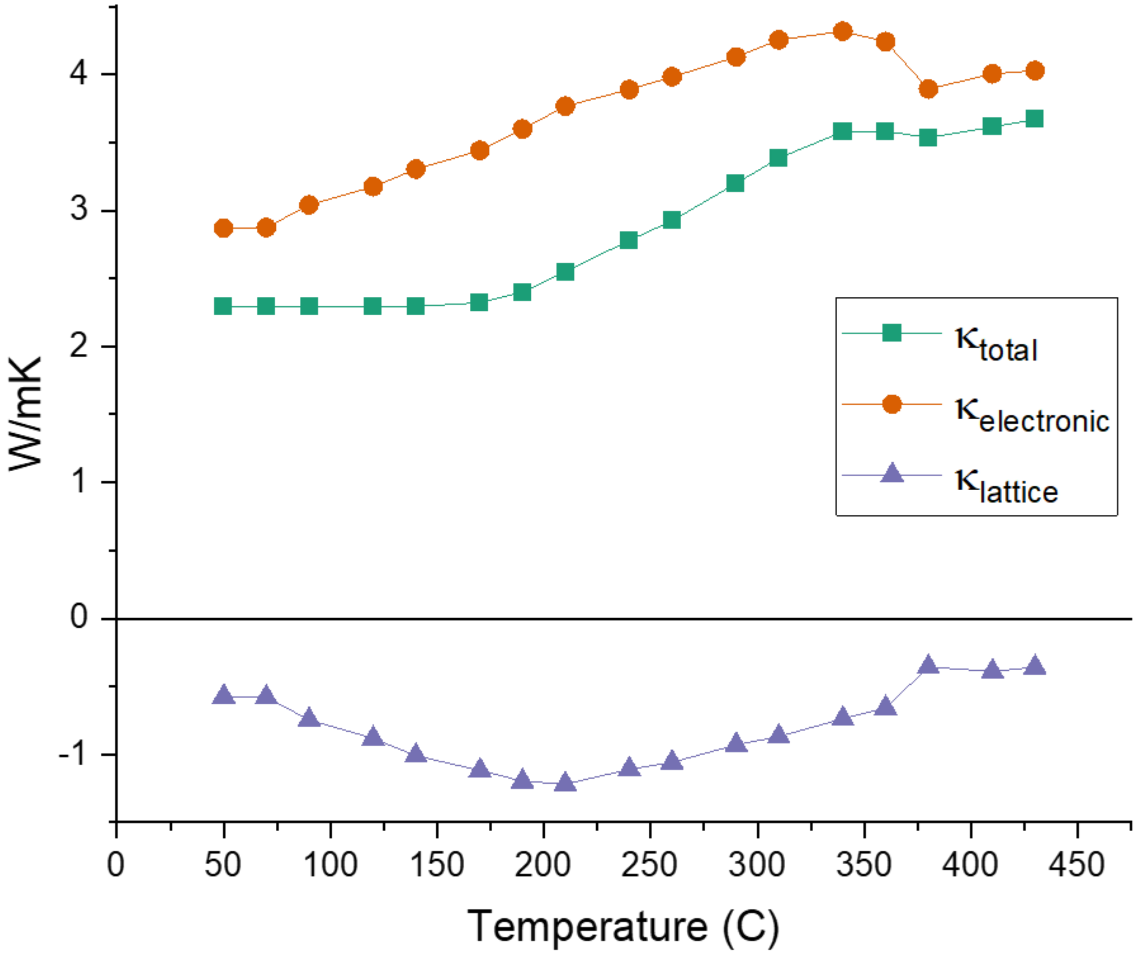

Figure 6.13: Thermal conductivity contributions for the x=.30 sample

While these results may be the most egregious in terms of non-physical results, the samples with higher concentrations of Sn fared better. For the x=.40 sample data shown in Figure 5.5, only sample 7 was able to be measured in both the LFA and ZEM. As this sample had a decrease in resistivity with temperature, it also displayed a decrease in the lattice thermal conductivity.

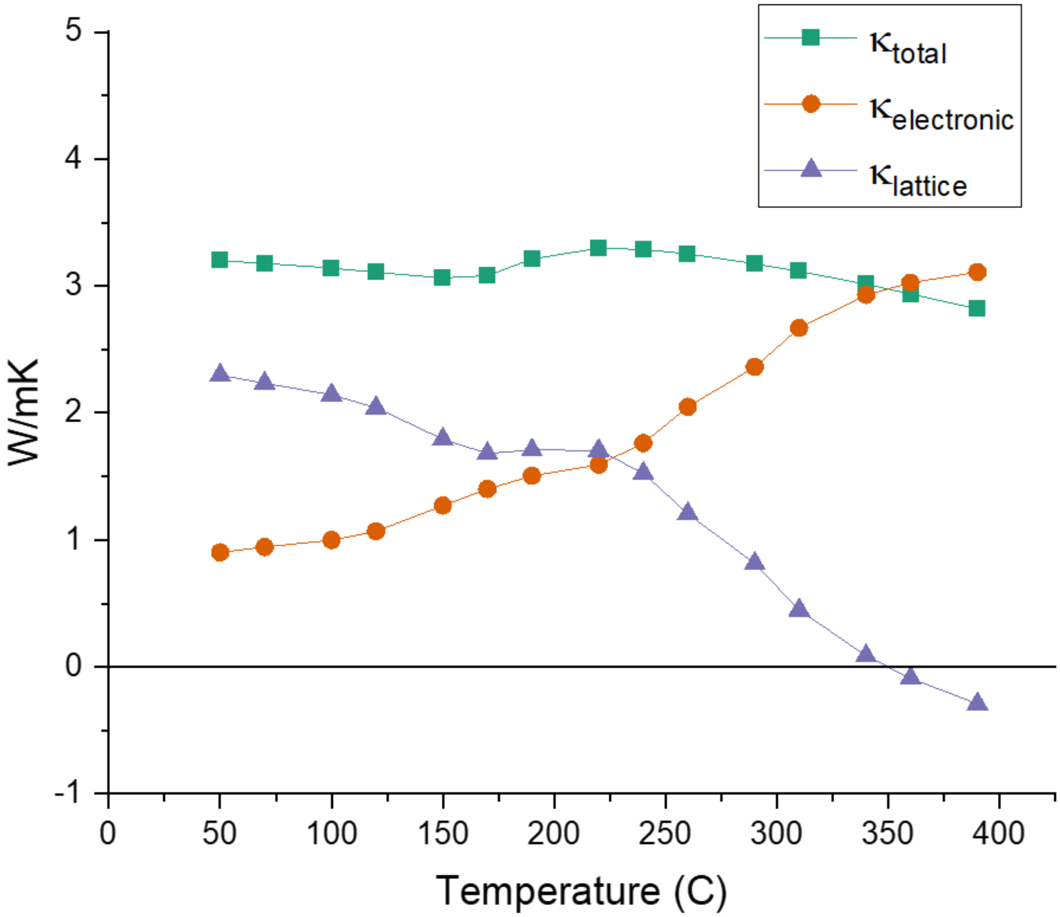

Figure 6.14: Thermal conductivity contributions for the x=.40 sample.

When this sample shows a bend in the total thermal conductivity curve at about 175 °C, this is also the temperature that we see a rapid increase in the electronic portion and a decrease in the lattice thermal conductivity. In fact, it continues to drop to below zero values at the highest measured temperatures. For the curious reader who might wonder what the results would be using the standard value for the Lorenz number, 2.44 x 10^{-8} W Ω K^{-2}, the non-physical results were even ‘worse.’ In our approximation, the calculated Lorenz numbers are smaller than the standard value (usually between 2.0 x 10^{-8} and 2.3 x 10^{-8} W Ω K^{-2},). Using the larger standard value would increase the electronic contribution, which would push lattice thermal conductivity values to be even more negative.

For samples in the middle of the solid solution and on the Sn-rich side, the results for lattice thermal conductivity were much more well behaved. While many had lattice thermal conductivities that were very low, none crossed below zero into non-physical territory. Below in Figure 6.15 we see the results for the x=.50 sample, for which HT-XRD showed undergoes this transition at 140 °C.

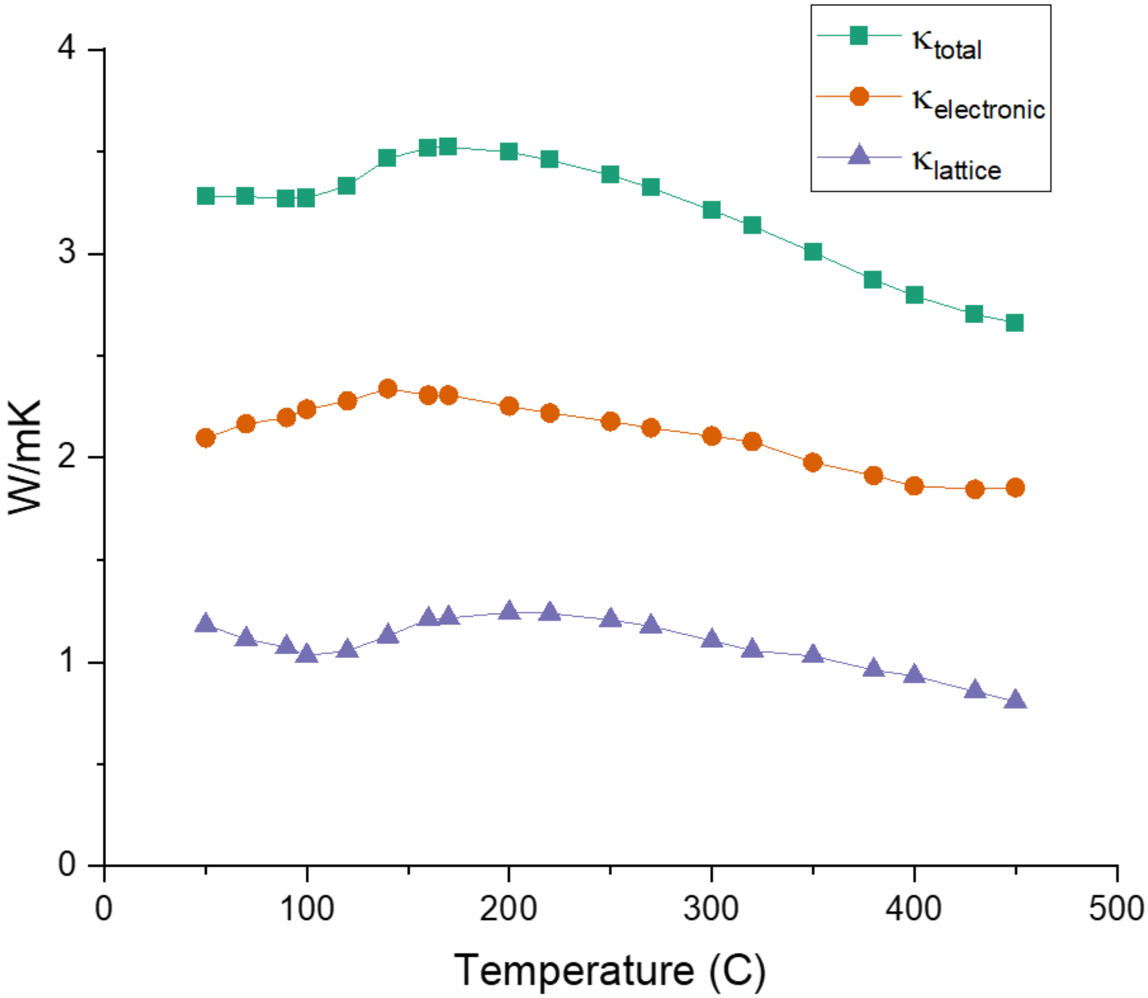

Figure 6.15: Thermal conductivity contributions for the x=.50 sample.

Here we see the total and lattice thermal conductivities mirror each other, where the transition to the cubic system corresponds to a slight increase in the lattice conduction. We saw this again in x=0.60, below in Figure 6.16. For the even-more Sn rich samples, we saw smooth curves as these samples are firmly in the cubic phase throughout the measured temperatures.

Figure 6.17 has the data for the x=0.70 sample.

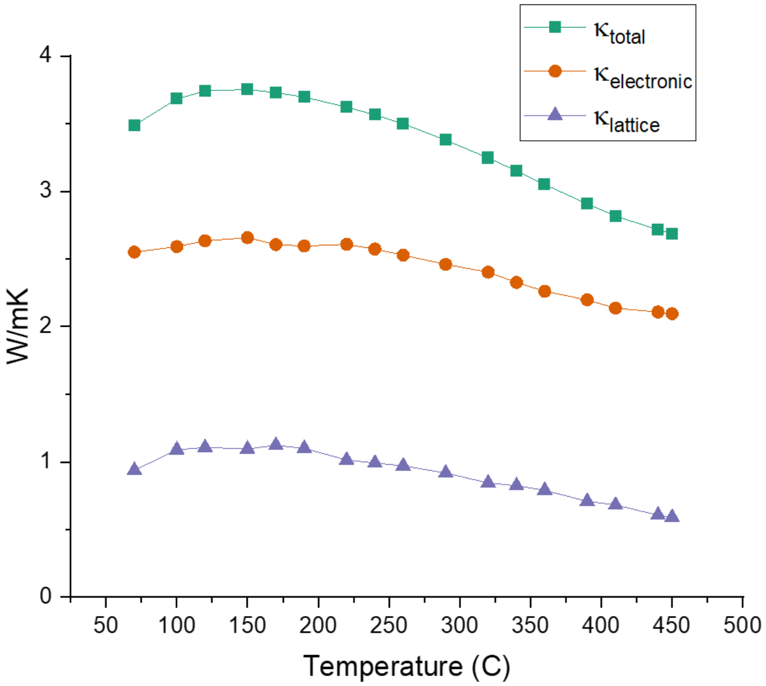

Figure 6.16: Thermal conductivity contributions for the x=.60 sample

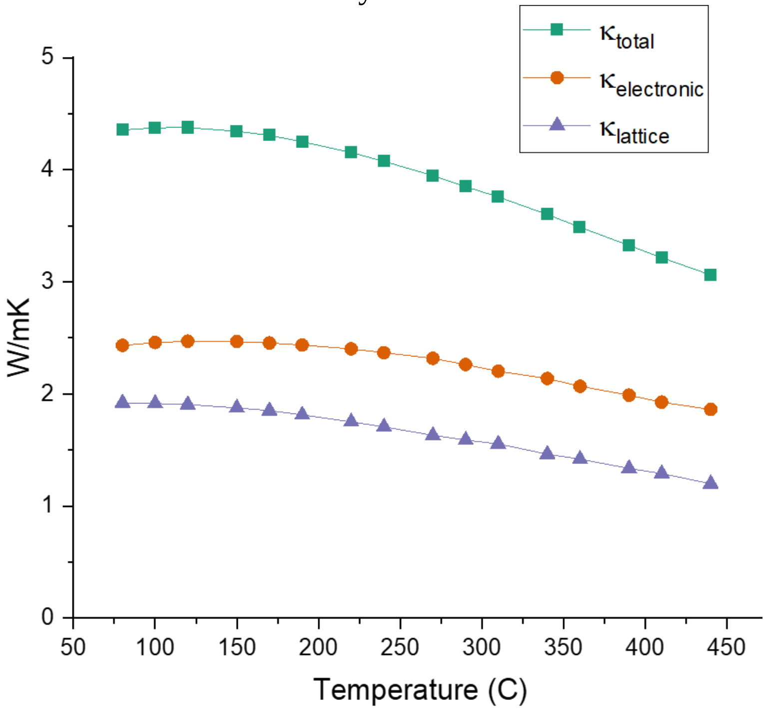

Figure 6.17: Thermal conductivity contributions for the x=.70 sample

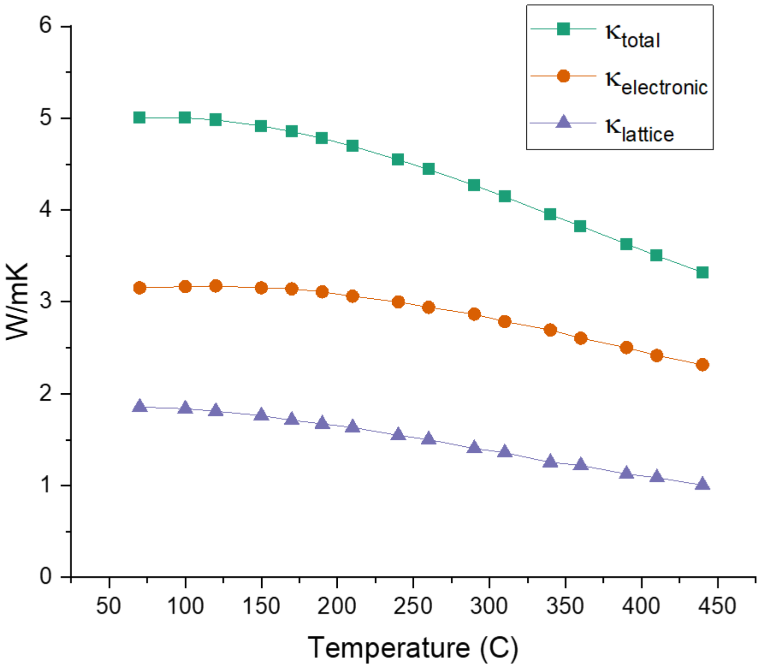

Figure 6.18: Thermal conductivity contributions for the x=.80 sample

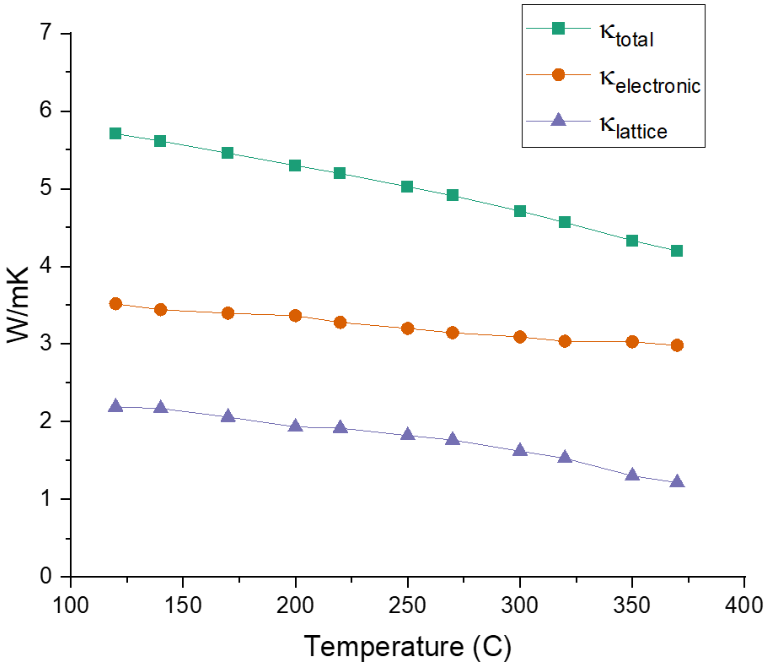

Figure 6.19: Thermal conductivity contributions for the x=.90 sample

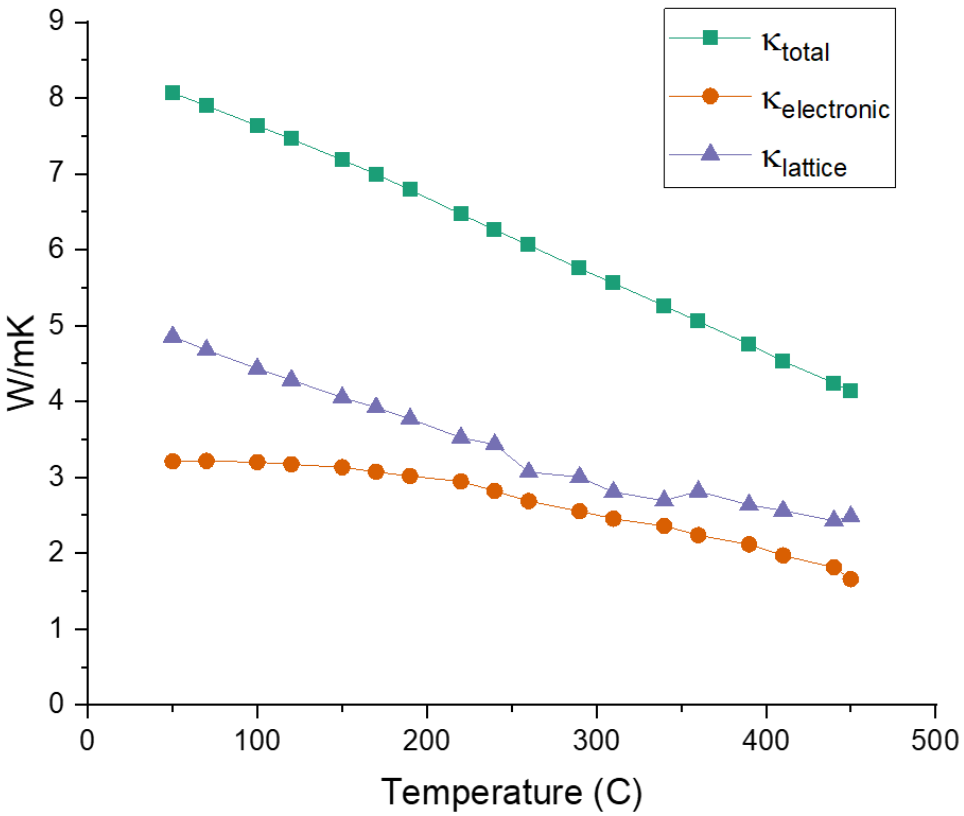

Figure 6.20: Thermal conductivity contributions for the SnTe sample

One thing to note about the results from the Sn-rich samples is that in all cases except for SnTe, the lattice thermal conductivity was less than that of the electronic contribution. For the SnTe sample the lattice contribution was bigger than the electronic. This makes sense, for as we saw with the data provided by the Hall measurement, the SnTe samples had a high carrier mobility. Now that we have presented the results on a per sample basis, we can examine what the trends are when we plot the results as a function of Sn. This is done below in Figure 6.23, and we again recover the ‘bathtub’ shape typical of alloy scattering we saw in Figure 6.9. Results with non-physical values are omitted from this figure. Also shown are just the $\kappa_{lattice}$ trends from the samples above, with the x=0.50 included on both figures for context in Figures 6.21and 6.22.

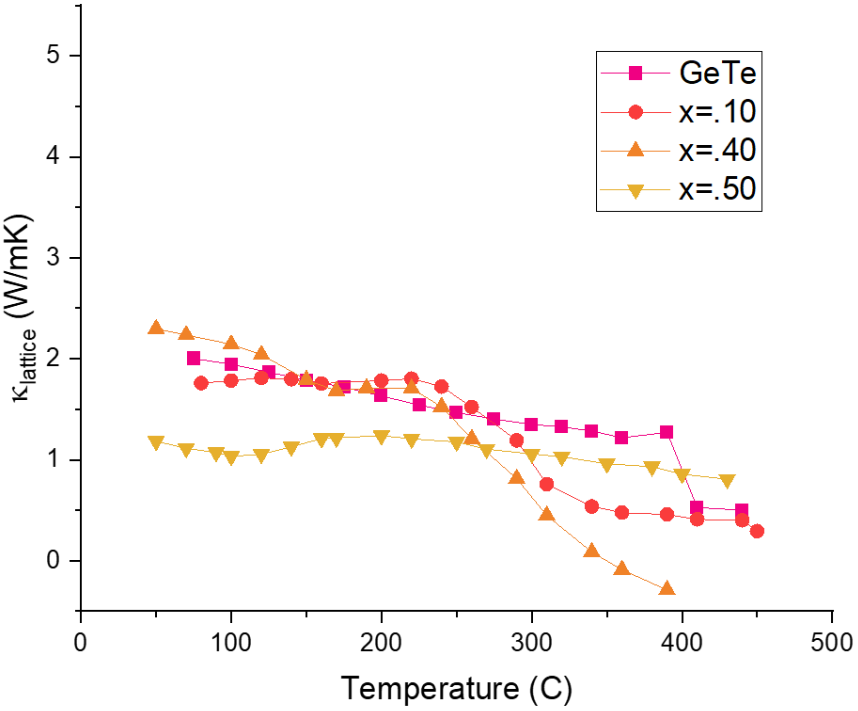

Figure 6.21: Lattice thermal conductivity trends for Ge-rich samples.

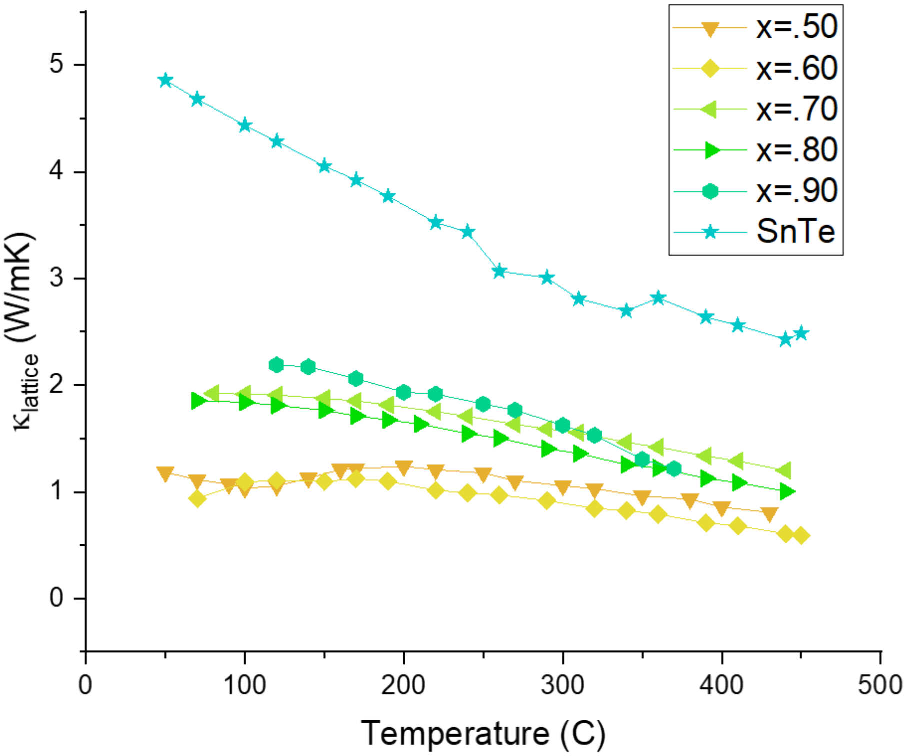

Figure 6.22: Lattice thermal conductivity trends for Sn-rich samples.

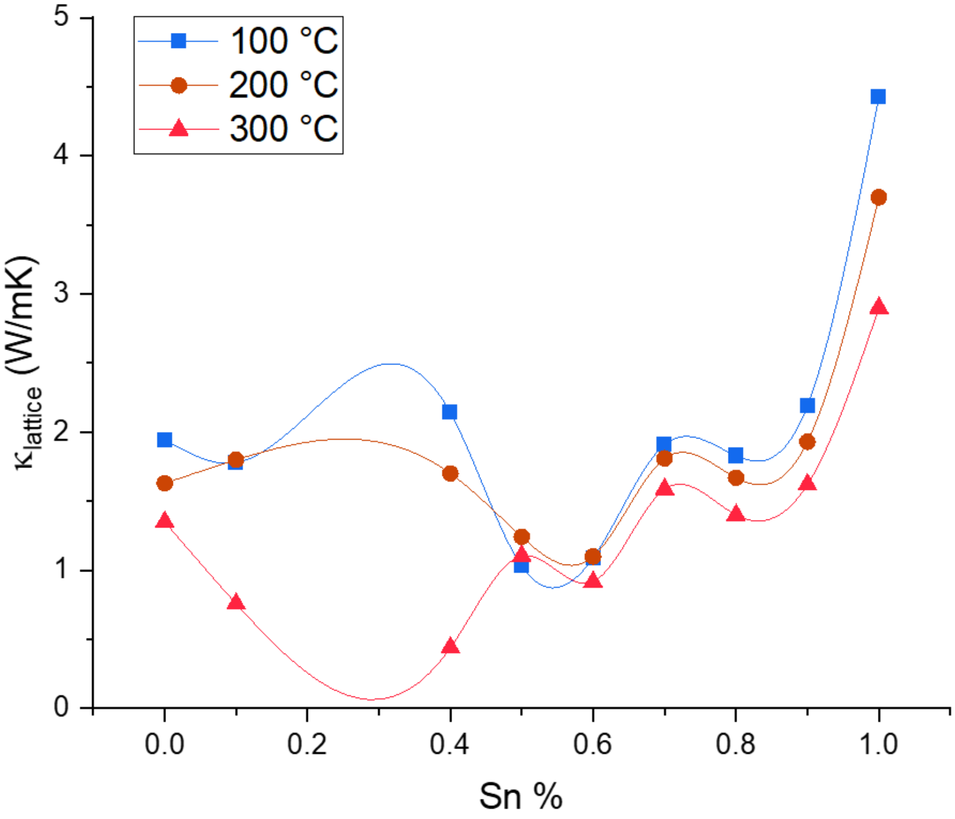

Figure 6.23 Lattice thermal conductivity trends as a function of Sn content at select temperatures.

Further insight into our heat conduction results can be gained by examining them in the light of the recent T = 0 K lattice dynamical calculations of Banik, et al. (Figure 6.24) [75]. Here we see that for SnTe in the cubic rocksalt structure (Figure Aa) optical phonons exhibit a slight instability at the Γ point. This instability causes Sn atoms to move slightly off-center and gives rise to the well-known ferroelectric behavior of SnTe [75]. For the x = 0.75 composition (Figure 6.24b), this instability at the Γ point is significantly enhanced, implying a greater displacement of Ge atoms. As conjectured by Banik, et al., these unstable optical phonon modes engender stronger anharmonic interactions with heat-carrying acoustic phonons, thus giving rise to the low thermal conductivity in Ge-containing samples, as well as the very weak temperature dependence of the lattice thermal conductivity of the endmember GeTe.

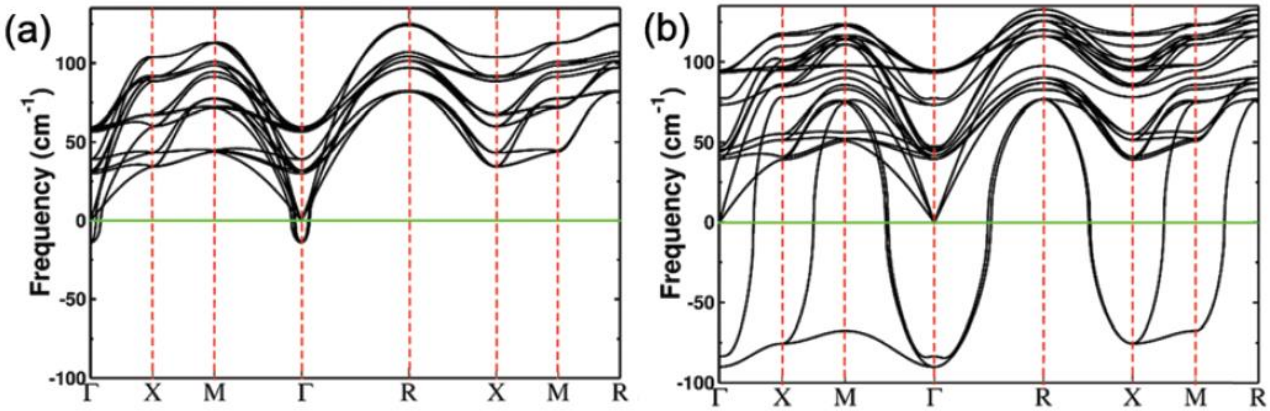

Figure 6.24 Phonon dispersion curves for a) SnTe and b) $Ge_{0.25}Sn_{0.75}Te$ in the cubic rocksalt structure at T = 0 K, according to Banik, et al. The slight instability of optical phonon branches at the Γ point in SnTe becomes strongly pronounced in the alloy.

6.3 Discussion of Thermal Behavior

While the temperature dependence of the thermal conductivity of SnTe is well-behaved (lattice thermal conductivity varying roughly inversely with temperature), GeTe exhibits an unusually low and nearly temperature independent thermal conductivity. We attribute this behavior to a combination of lattice softening and strong anharmonic scattering due to the non-centrosymmetric crystal structure of GeTe. For SnTe/GeTe, mixed crystals, the thermal behavior observed in this study provides a textbook example of a system with strong alloy scattering. While GeTe and SnTe have intrinsically low thermal conductivities, the binary alloy system proved to reduce this conductivity further. We observe strong evidence of alloy scattering, with the lowest thermal conductivities in the middle region of the alloy providing the most disorder in the lattice. The trends in the total thermal conductivity are detailed in Figure 6.9, and this figure captures the 'bathtub' shape predicted by the Klemens model, especially at elevated temperatures.

The trends were also interesting in the temperature regions of the phase transition. While some samples, notably GeTe, found their thermal conductivity reduced in the high-temperature cubic phase other samples, especially those rich in Sn, saw their thermal conductivity increase. The magnitude of the step was the biggest in GeTe, with a step of almost 1 W/mK in both total and lattice thermal conductivity. The size of the step, and the sharpness of the transition, was much smaller for alloyed samples. While GeTe saw a drop in conductivity in a temperature span of roughly 20 degrees, the alloyed samples saw non-linear behavior in a range twice or three times that of GeTe. For example, the x=0.50 saw a rise of 0.25 W/mK spread over an 80-degree range in temperature. Initially we were hoping that the alloyed samples would demonstrate sharper and larger changes in thermal behavior like the end-member GeTe, but this was not the case. What is also unresolved is why some concentrations of these mixed crystals saw a step up versus a step down in thermal conductivity.

We recovered similar alloy-scattering trends when we examined the lattice contributions of the thermal conductivity. When examining the total thermal conductivity, the “bathtub” shape reflected in Figure 6.9 demonstrates that the alloy scattering mechanism (an effect on the lattice thermal conductivity) is the dominant mechanism, in addition to evidence of less dominant phonon-carrier scattering. While some samples produced unphysical results in calculating the size of the lattice contribution, for the physical results we recovered the expected Klemens model shape. There was trouble with the Ge-rich sample stability, reproductivity as well as sample brittleness so further investigation is needed to fully understand the contributions of Ge-rich samples to the understanding of this phase transition. It could be that these samples, with transition temperatures in the range of 200-300 °C, need additional considerations from a synthesis standpoint to make them more consistent. It’s possible that the repeated measurements and synthesis steps at elevated temperatures are introducing stress into the sample. Early attempts at annealing Ge-rich samples below their cubic transition temperature did not appear to improve sample durability. It’s also clear that the Lorenz numbers used historically and from estimates using Seebeck coefficient were unable to produce physical results for many samples. While we can trust the total thermal conductivity numbers, a better calculation for the electronic portions of the thermal conductivity would allow us to say more about the behavior of the lattice thermal conductivity with temperature and near the structural phase transition. In addition further study of the synthesis and properties of Ge-rich alloys could shed additional light on whether slight changes in synthesis procedure produce effects on the thermal behavior.

6.4 Figure-of-merit ZT Calculations

With the wealth of data collected and reported above, we now can complete a calculation of the thermoelectric figure of merit, ZT. Below in Figure 6.25 are the ZT results for Ge-rich samples, for which the x=0.05 was the clear favorite. Due to the high power factor and decent thermal performance, the x=0.05 proved to have the highest ZT of all the results in this study with a ZT of 0.40 at 450 °C. Close behind was the ZT from the GeTe sample, which increased rapidly as it approached and moved through the structural phase transition and had a peak ZT of 0.28 at 450 °C.

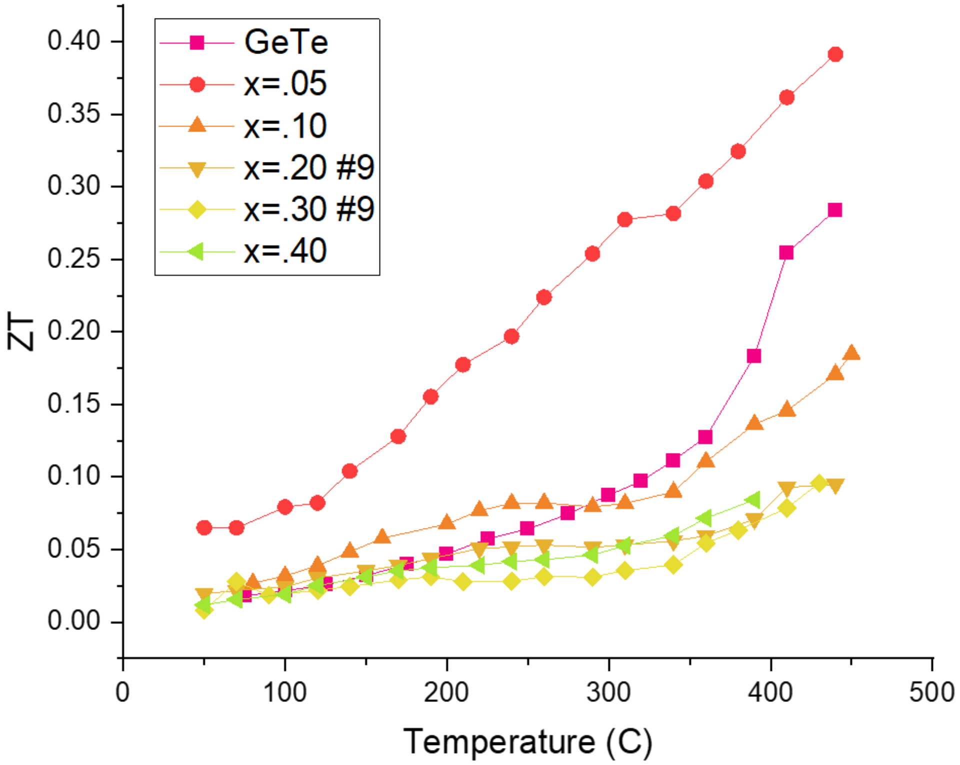

Figure 6.25: ZT trends for Ge-rich samples. Note that the x=.05 sample is the highest performing.

The trends for increasing amounts of Sn proved to result in similar ZT values for x-values x=.10 through x=0.40. As for the Sn-rich samples, the x=0.50 sample had a middling ZT, while surprisingly the x=0.60 sample had the second highest ZT values in this temperature range, peaking at 0.38 at 450 °C . The other Sn-rich samples had values similar to the Ge-rich samples, while the SnTe proved the worst, weighed down by its higher thermal conductivity.

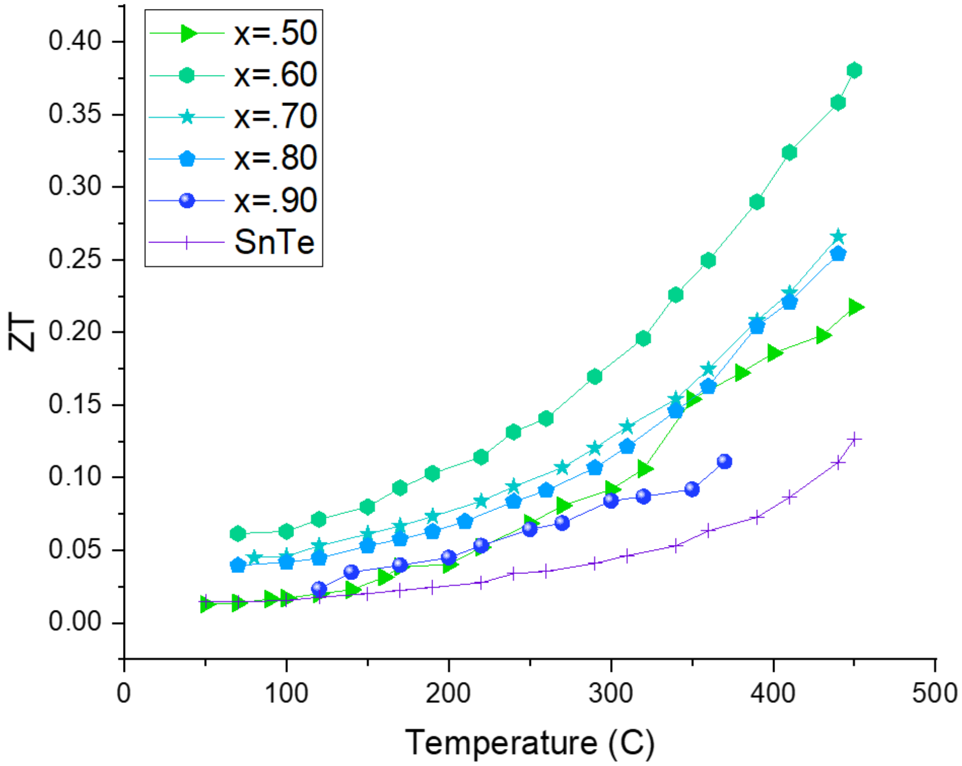

Figure 6.26: ZT trends for Sn-rich samples. Note the high performance of the x=.60 sample.

The x=0.60 sample benefitted from having better Seebeck coefficients than most samples, leading to a high power factor, as well as one of the lowest total thermal conductivities over this temperature range, only getting better at higher temperatures. The ZT values for the other Sn-rich samples were weighed down by both higher thermal conductivity values as well as being generally more resistive. Finally, a figure of ZT values as a function of Sn content is shown below in Figure 6.27. We see here a curious double peak here with the x=0.05 and the x=0.60 samples being high scorers while other concentrations of Sn didn't do so well. GeTe was a better performer than SnTe, as we would expect from the better electronic performance of GeTe as well as the higher thermal conductivity observed in SnTe.

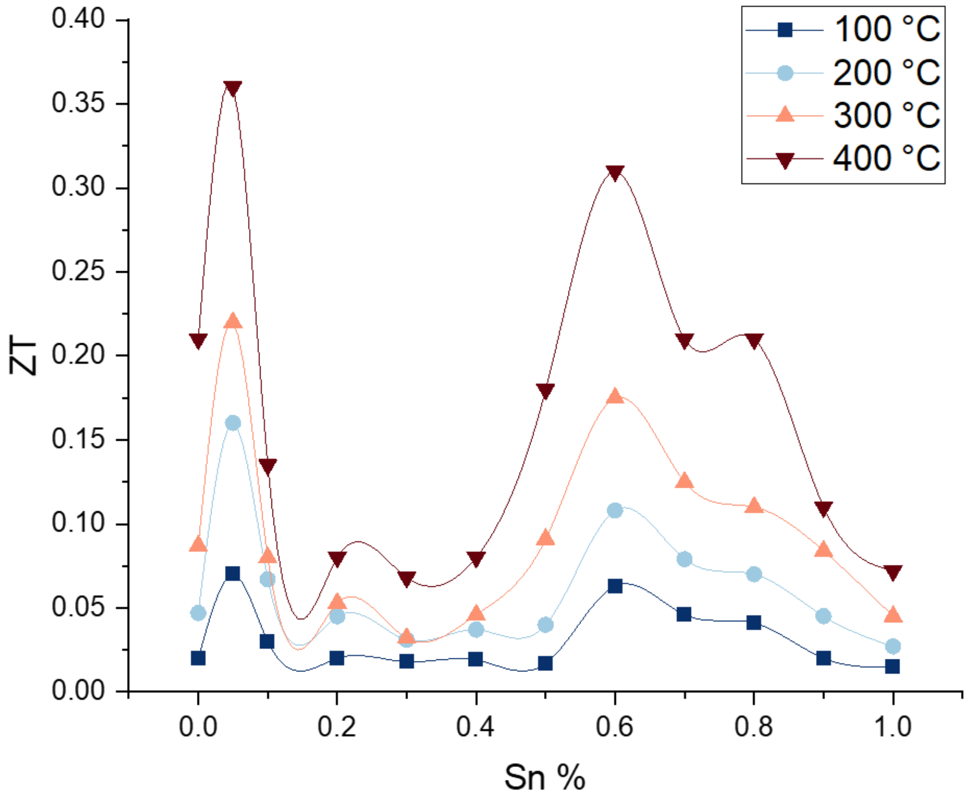

Figure 6.27: ZT trends as a function of Sn content. Note the peaks at x=.05 and x=.60.

While both x=0.05 and x=0.60 were high performers, the nature of their performances was achieved in different ways. With the x=0.05 sample, the measured power factor (S^2/ρ) was the highest measured sample in this study, helped in large part by having one of the lowest resistivities. In contrast, the x=0.60 scored a high ZT in large part due to its thermal behavior, among the lowest in this study especially at higher temperatures. In addition, it benefited from a much better power factor than its x=0.50 and x=0.70 neighbors by having the highest Seebeck coefficient of all samples measured in this study.

Chapter 7 CONCLUSIONS AND FUTURE WORK

In surveying the results and observations reported throughout the study above, we can report several conclusions about the $Ge_{(1-x)}Sn_{(x)}Te$ system. First, we report a way to consistently synthesize polycrystalline samples of high density using direct-fusion, ball-milling and Spark-Plasma Sintering detailed at the end of Chapter 3. By combining structure data obtained from X-ray Diffraction at room temperature as well as at elevated temperature with the data from thermal measurements in the LFA, we can update the phase diagram first laid out by Bierly et al in 1963 shown in Figure 6.8. This expansion of the phase diagram enables follow-up studies to further probe the mechanisms behind the transition as well as provide a roadmap to those developing these materials for thermoelectrics or other applications. The information provided by the RUS analysis leaves tantalizing clues about the softening of elastic modes in the proximity of the structural transition. These observations compare well to previous studies that detail the ferroelectric instability of the cation site in both rhombohedral and cubic structures.

From the electronic and thermal transport data, this study provides a systematic array of data that could be used to plan doping studies to optimize the carrier concentration or other variables. Quite surprisingly, although the samples studies here have not been doped to optimize their thermoelectric properties, some samples achieve reasonably high values of thermoelectric figure of merit. Not unexpectedly, the compositions with lowest thermal conductivity were those near the middle of the binary alloy system. With lattice thermal conductivity values on the order of 1W/mK, these samples are likely approaching the amorphous limit for this system and so further optimization would have to come in the form of altering the electronic behavior of the sample. Further attempts to reduce the lattice thermal conductivity via micro or nano structuring likely will not be as successful, for as we are near the amorphous limit the mean free path for a phonon is approaching the lattice constant of the material already. In addition, the off-centering of Ge and Sn from their lattice sites proposed by Banik et al [75] would provide a scattering site on the order of the lattice constant – a smaller scale than any micro- or nano structuring could achieve. The data shown by the carrier concentration and mobility provide strong evidence of Sn atoms filling Ge vacancies, which suppressed the carrier concentration while improving the carrier mobility. This agrees well with recent studies of vacancy-suppressed GeTe that showed that a suppression of vacancies causes the carrier mobility in GeTe to increase dramatically [39,42,49]. Our work here further highlights the critical role played by vacancies in these alloys and the necessity of controlling them in order to improve the electrical transport characteristics of these materials.

We had a curious result where the measured ZT of these alloys had two peaks; one for x=0.05 and one for x=0.60. These two results show alternate pathways of realizing thermoelectric performance by either maximizing the power factor or by reducing thermal conductivity. It's clear that both samples in question are far from optimized, so achieving a ZT of unity in this alloy system is quite realistic. Substituting Sn for Ge provides a low-cost and more environmentally friendly way of attaining similar performance in a material, increasing the likelihood of adoption for applications. In addition, by tuning the cubic transition temperature with the inclusion of Sn, a device can be tuned to a specific temperature range depending on the application.

From the trends detailed in this study, we can identify several routes forward that would further increase our understanding of the fundamentals of this system as well as improve the performance of these alloys for thermoelectric applications. First, one could execute a full structural study of all alloys in the system at elevated temperatures for both HT-XRD and HT-

RUS. These studies could be used to pinpoint the exact temperatures of phase transition as well as characterize the elastic behavior before, during, and after the phase change. Perhaps the softening of the elastic constants can be tuned to a specific temperature range with Sn content to maximize the elastic properties for thermoelectric applications.

Additional dopants may provide the system with more mechanical stability, making it less brittle, as well as improving the electrical performance. N-type doping to further reduce the hole concentration should be used, as the carrier concentrations measured here are likely far above the optimal levels. By reducing the carrier concentration, the Seebeck coefficient should increase with a small penalty to the electrical conductivity, while also reducing the electronic component of the total thermal conductivity. For almost all samples, the electronic contribution to the thermal conductivity was greater than the lattice contribution, so optimizing the carrier concentration would improve the ZT performance synergistically. This has been tried by others with many having success in improving ZT using various N-type dopants, including Sb and Bi as well as transition-metal co-doping and alloying with Mn, Cu, In, Ga [58,63,111,117]. It is possible that some "TAGS-85" like combination of doping and alloying would yield a high-performing material in this system that would simultaneously optimize the thermoelectric performance while also minimizing the amount of precious, toxic, or rare elements used to do so. As GeTe-based thermoelectrics were developed in response to replacing toxic Pb in PbTe, we now come full circle to examine ways to replace the expensive Ge with less costly and earth abundant elements like Sn. Overall, as many have realized, the GeTe-SnTe system is a seemingly simple system that can serve as a model system to develop a better fundamental understanding of structure-property relationships as well as develop a more thorough understanding in how to design thermoelectrics for better performance.

REFERENCES

[1] van Ruijven, B. J., De Cian, E. & Sue Wing, I. Amplification of future energy demand growth due to climate change. *Nat. Commun*. 10, 1–12 (2019).

[2] Kreps, B. H. The Rising Costs of Fossil-Fuel Extraction: An Energy Crisis That Will Not Go Away. *Am. J. Econ. Sociol.* 79, 695–717 (2020).

[3] O'Neill, B. C. et al. Global demographic trends and future carbon emissions. *Proc. Natl. Acad. Sci. U. S. A.* 107, 17521–17526 (2010).

[4] Pathak, M. WORKING GROUP III CONTRIBUTION TO THE IPCC SIXTH ASSESSMENT REPORT (AR6) Technical Summary. Mitig. Clim. Chang. (2021).

[5] Gowdy, J. Our hunter-gatherer future: Climate change, agriculture and uncivilization. *Futures* 115, 102488 (2020).

[6] Rogelj, J., Forster, P. M., Kriegler, E., Smith, C. J. & Séférian, R. Estimating and tracking the remaining carbon budget for stringent climate targets. *Nature* 571, 335–342 (2019).

[7] Ramanathan, V. & Feng, Y. On avoiding dangerous anthropogenic interference with the climate system: Formidable challenges ahead. *Proc. Natl. Acad. Sci. U. S. A.* 105, 14245–14250 (2008).

[8] Li, J. et al. Scattering and absorbing aerosols in the climate system. *Nat. Rev. Earth Environ.* 3, 363–379 (2022).

[9] Forman, C., Muritala, I. K., Pardemann, R. & Meyer, B. Estimating the global waste heat potential. *Renew. Sustain. Energy Rev*. 57, 1568–1579 (2016).

[10] US Department of Energy, Lawrence Livermore National Laboratory, Estimated Energy Flow Chart, http://flowcharts.llnl.gov/. (Accessed: 28 June 2023).

[11] Seebeck, T. J. Ueber die magnetische Polarisation der Metalle und Erze durch Tempeeratur-Differenz. *Ann. Phys*. 82(2):133-160, (1826)

[12] Peltier, J.C. Nouvelles experiences sur la caolricite des courants electriques. *Ann Chim Phys.* 56(371):371, (1834)

[13] Thomson. W.Account of Researches in Thermo-Electricity. *Proc. R Soc. London*, 7(0): 49-58, (1854)

[14] Altenkirch E. Uber den Nutzeffect der Thermosaule. *Phys Zeitschrift*. 10:560-580, (1909)

[15] Ioffe A. F., *et al*; Semiconductor Thermoelements and Thermoelectric Cooling. *Physics Today* 1 May ; 12 (5): 42. (1959)

[16] Onsager, L. Reciprocal relations in irreversible processes I. *Phys Rev.* 37:405-426 (1931).

[17] Goldsmid, H.J. The Electrical Conductivity and Thermoelectric Power of Bismuth Telluride. *Proc Phys. Soc. London*, 71 (460): 633-646, (1958).

[18] Lloyd I. Shure *et al*. NASA TM X-52158 N66-14775. Technical Report, Lewis Research Center (1965)

[19] NASA. Space Radioisotope Power Systems: Multi-Mission Radioisotope Thermoelectric Generator. (2008).

[20] Zhao, L.-D. et al. Ultralow thermal conductivity and high thermoelectric figure of merit in SnSe crystals. *Nature* 508, 373–377 (2014).

[21] Snyder, G. J. & Toberer, E. S. Complex thermoelectric materials. *Nat. Mater.* 7, 105–114 (2008).

[22] LeBlanc, S., Yee, S. K., Scullin, M. L., Dames, C. & Goodson, K. E. Material and manufacturing cost considerations for thermoelectrics. *Renew. Sustain. Energy Rev*. 32, 313–327 (2014).

[23] Shi, X., Chen, L. & Uher, C. Recent advances in high-performance bulk thermoelectric materials. *Int. Mater. Rev.* 61, 379–415 (2016).

[24] Gayner, C. & Kar, K. K. Recent advances in thermoelectric materials. *Prog. Mater. Sci.* 83, 330–382 (2016).

[25] Nolas, G. S., Morelli, D. T. & Tritt, T. M. Skutterudites: a phonon-glass-electron crystal approach to advanced thermoelectric energy conversion applications. *Annu. Rev. Mater. Sci.* 29, 89–116 (1999).

[26] Snyder, G. J., Christensen, M., Nishibori, E., Caillat, T. & Iversen, B. B. Disordered zinc in Zn4Sb3 with phonon-glass and electron-crystal thermoelectric properties. *Nat. Mater.* 3, 458–463 (2004).

[27] Chen, Z. G., Shi, X., Zhao, L. D. & Zou, J. High-performance SnSe thermoelectric materials: Progress and future challenge. *Prog. Mater. Sci.* 97, 283–346 (2018).
[28] Rowe, D. M. Applications of nuclear-powered thermoelectric generators in space. *Appl. Energy* 40, 241–271 (1991).

[29] Giri Joshi. et al. Enhanced thermoelectric figure of merit in nanostructured n-type silicon germanium bulk alloy. 8, 12, 4670–4674. *Nano Letters* (2008)

[30] Zevalkink, A. et al. A practical field guide to thermoelectrics: fundamentals, synthesis, and characterization. *Appl. Phys. Rev.* (2018).

[31] Zhou, C. et al. Polycrystalline SnSe with a thermoelectric figure of merit greater than the single crystal. *Nat. Mater.* 20, 1378–1384 (2021).

[32] Samanta, M. & Biswas, K. Low Thermal Conductivity and High Thermoelectric Performance in (GeTe)1-2x(GeSe)x(GeS)x: Competition between Solid Solution and Phase Separation. *J. Am. Chem. Soc*. 139, 9382–9391 (2017).

[33] Wu, D. et al. Origin of the high performance in GeTe-based thermoelectric materials upon Bi2Te3 doping. *J. Am. Chem. Soc.* 136, 11412–11419 (2014).

[34] Rosenthal, T. et al. Enhancing the thermoelectric properties of germanium antimony tellurides by substitution with selenium in compounds GenSb2(Te 1-xSex)n+3 (0 ≤ x ≤ 0.5; N ≥ 7). *Chem. Mater.* 26, 2567–2578 (2014).

[35] Li, J. et al. Electronic origin of the high thermoelectric performance of GeTe among the p-type group IV monotellurides. *NPG Asia Mater.* 9, e353-8 (2017).

[36] Levin, E. M., Cooling, C., *et al.* Crystal structure, magnetization, 125Te NMR, and Seebeck coefficient of Ge49Te50R1 (R= La, Pr, Gd, Dy, and Yb). *Materials Chemistry and Physics*, 192, 58-66. (2017).

[37] Li, J. et al. Simultaneous Optimization of Carrier Concentration and Alloy Scattering for Ultrahigh Performance GeTe Thermoelectrics. *Adv. Sci.* 4, (2017).

[38] Li, J. et al. Low-Symmetry Rhombohedral GeTe Thermoelectrics. *Joule* 2, 976–987 (2018).

[39] Zhang, X. et al. Vacancy Manipulation for Thermoelectric Enhancements in GeTe Alloys. *J. Am. Chem. Soc*. 140, 15883–15888 (2018).

[40] Liu, H. et al. Band and Phonon Engineering for Thermoelectric Enhancements of Rhombohedral GeTe. *ACS Appl. Mater. Interfaces* 11, 30756–30762 (2019).

[41] Bu, Z. et al. Dilute Cu2Te-alloying enables extraordinary performance of r-GeTe thermoelectrics. Mater. *Today Phys*. 9, 1–7 (2019).

[42] Dong, J. et al. Medium-temperature thermoelectric GeTe: Vacancy suppression and band structure engineering leading to high performance. *Energy Environ. Sci.* 12, 1396–1403 (2019).

[43] Zhang, X. et al. GeTe Thermoelectrics. *Joule* 4, 986–1003 (2020).

[44] Jiang, Y. et al. Evolution of defect structures leading to high ZT in GeTe-based thermoelectric materials. *Nat. Commun.* 13, (2022).

[45] Levin, E. M., Besser, M. F. & Hanus, R. Electronic and thermal transport in GeTe: A versatile base for thermoelectric materials. *J. Appl. Phys*. 114, (2013).

[46] Edwards, A. H. et al. Electronic structure of intrinsic defects in crystalline germanium telluride. *Phys. Rev. B - Condens. Matter Mater. Phys.* 73, 1–13 (2006).

[47] Fukuma, Y., Asada, H., Arifuku, M. & Koyanagi, T. Carrier-enhanced ferromagnetism in Ge1-xMnxTe. *Appl. Phys. Lett.* 80, 1013–1015 (2002).

[48] Kimber, S. A. J. et al. Dynamic crystallography reveals spontaneous anisotropy in cubic GeTe. *Nat. Mater.* 22, 311–315 (2023).

[49] Liu, Z. Shaping the role of germanium vacancies in germanium telluride : metastable cubic structure stabilization , band structure modification , and stable N-type conduction. *NPG Asia Mater*. (2020) doi:10.1038/s41427-020-00247-y.

[50] Adamczyk, J. M. et al. Symmetry breaking in Ge1−xMnxTe and the impact on thermoelectric transport. *J. Mater. Chem*. A 10, 16468–16477 (2022).

[51] Tan, G. et al. High thermoelectric performance of p-type SnTe via a synergistic band engineering and nanostructuring approach. *J. Am. Chem. Soc.* 136, 7006–7017 (2014).

[52] Tan, G. et al. High Thermoelectric Performance SnTe-In2Te3Solid Solutions Enabled by Resonant Levels and Strong Vacancy Phonon Scattering. *Chem. Mater.* 27, 7801–7811 (2015).

[53] Tan, G. et al. Valence Band Modification and High Thermoelectric Performance in SnTe Heavily Alloyed with MnTe. *J. Am. Chem. Soc.* 137, 11507–11516 (2015).

[54] Tan, G. et al. Codoping in SnTe: Enhancement of thermoelectric performance through synergy of resonance levels and band convergence. *J. Am. Chem. Soc.* 137, 5100–5112 (2015).

[55] Wu, H. et al. Synergistically optimized electrical and thermal transport properties of SnTe via alloying high-solubility MnTe. *Energy Environ. Sci.* 8, 3298–3312 (2015).

[56] Li, W. et al. Band and scattering tuning for high performance thermoelectric Sn1−xMnxTe alloys. *J. Mater.* 1, 307–315 (2015).

[57] Pei, Y. et al. Interstitial Point Defect Scattering Contributing to High Thermoelectric Performance in SnTe. *Adv. Electron. Mater*. 2, 1–8 (2016).

[58] Li, S. M. *et al.* Phases and thermoelectric properties in stoichiometric Sn1−xMnxTe and non-stoichiometric Sn1−yMn1.1yTe alloys. *Mater. Des.* **108**, 51–59 (2016).

[59] Zhang, X. *et al.* Enhancing thermoelectric performance of SnTe via nanostructuring particle size. *J. Alloys Compd.* **709**, 575–580 (2017).

[60] Li, W. *et al.* Advances in Environment-Friendly SnTe Thermoelectrics. *ACS Energy Lett.* **2**, 2349–2355 (2017).

[61] Zheng, L. *et al.* Interstitial Defects Improving Thermoelectric SnTe in Addition to Band Convergence. *ACS Energy Lett.* **2**, 563–568 (2017).

[62] Tan, G. *et al.* High Thermoelectric Performance of p-Type SnTe via a Synergistic Band Engineering and Nanostructuring Approach. *J. Am. Chem. Soc.* **2**, 8625–8637 (2017).

[63] Al Rahal Al Orabi, R. *et al.* Ultralow Lattice Thermal Conductivity and Enhanced Thermoelectric Performance in SnTe:Ga Materials. *Chem. Mater.* **29**, 612–620 (2017).

[64] Wang, L. *et al.* Hierarchical Structuring to Break the Amorphous Limit of Lattice Thermal Conductivity in High-Performance SnTe-Based Thermoelectrics. *ACS Appl. Mater. Interfaces* **12**, 36370–36379 (2020).

[65] Jiang, Q. *et al.* High Thermoelectric Performance in SnTe Nanocomposites with All-Scale Hierarchical Structures. *ACS Appl. Mater. Interfaces* **12**, 23102–23109 (2020).

[66] Shtanov, V. I., *et al.* A contribution to the phase diagram of the system Ge-Sn-Te and the conditions of (Sn, Ge)Te crystal growth. *J. Alloys Compd.* **476**, 812–816 (2009).

[67] Bierly, J. N., Muldawer, L. & Beckman, O. The continuous rhombohedral-cubic transformation in GeTe-SnTe alloys. *Acta Metall.* **11**, 447–454 (1963).

[68] Lewis, J. E. & Lasjaunias, J. C. Specific heat and resistivity of the GeTe-SnTe alloy system. *Philos. Mag.* **32**, 687–696 (1975).

[69] Rehwald, W. & Lang, G. K. Ultrasonic studies of phase transitions in the tin telluride-germanium telluride system SnxGe1-xTe. *J. Phys. C Solid State Phys.* **8**, 3287–3296 (1975).

[70] Prakash, S., Gupta, H. C. & Tripathi, B. B. Thermal properties of narrow-band-gap semiconducting mixed crystals Ge(x)Sn(1-x)Te. **27**, (1983).

[71] Yashina, L. & Leute, V. The phase diagrams of the quasibinary systems (Pb,Ge)Te and (Ge,Sn)Te. **313**, 85–92 (2000).

[72] Sivabharathy, M., Sankar, N., Saravanan, R. & Ramachandran, K. Optical, thermal and phase transition studies in Sn1-xGe xTe. *Bull. Mater. Sci.* **28**, 675–679 (2005).

[73] Wu, C. C., Ferng, N. J. & Gau, H. J. Thermoelectric properties of Ge1-xSnxTe crystals grown by vertical Bridgman method. *J. Cryst. Growth* **304**, 127–132 (2007).

[74] Robert, M. C. & Saravanan, R. Single crystal X-ray analysis of the electronic structure of the thermoelectric material Sn1-xGexTe. *Indian J. Phys.* **84**, 1203–1210 (2010).

[75] Banik, A. *et al.* Engineering ferroelectric instability to achieve ultralow thermal conductivity and high thermoelectric performance in Sn 1-: X Ge x Te. *Energy Environ. Sci.* **12**, 589–595 (2019).

[76] Ashcroft N., Mermin, N. *Solid State Physics* Thomson Press (1976).

[77] Sze. S.M. *Physics of Semiconductor Devices* Wiley-Interscience, second edition (1981).

[78]Bardeen, J. Shockley ,W. Deformation potentials and mobilities in non-polar crystals. *Phys Rev.* 80(1) 72-80 (1950).

[79] Conwell, E. *et al*. Theory of Impurity Scattering in Semiconductors. *Phys Rev.* 77(3) 388-390 (1950)

[80] Tritt, T.M. *Annual Review of Materials Research*. **41** 433 (2011).

[81] Kim, H. S., Gibbs, Z. M., Tang, Y., Wang, H. & Snyder, G. J. Characterization of Lorenz number with Seebeck coefficient measurement. *APL Mater.* **3**, 1–6 (2015).

[82] Wiedemann G, Franz R. Ueber die Warme-Leitungsfahgkeit der Metalle. *Ann der Phys, und Chemie,* 165 (8): 497-531 (1853).

[83] Berman R. *Thermal Conduction in Solids*. Oxford University Press (1976).

[84] Kopp, R. E. *et al.* Communicating future sea-level rise uncertainty and ambiguity to assessment users. *Nature Climate Change* (2023) doi:10.1038/s41558-023-01691-8.

[85] Matthiessen, A.; Vogt, C. *Annalen der Physik.* 198, 19–78. (1864),

[86] Bauer Pereira, P. *et al.* Lattice dynamics and structure of GeTe, SnTe and PbTe. *Phys. Status Solidi Basic Res.* **250**, 1300–1307 (2013).

[87] Morelli, D. T., Perry, T. A. & Farmer, J. W. Phonon scattering in lightly neutron-irradiated diamond. *Phys. Rev. B* **47**, 131–139 (1993).

[88] Klemens, P. G. The scattering of low-frequency lattice waves by static imperfections. *Proc. Phys. Soc. Sect. A* **68**, 1113–1128 (1955).

[89] Rayleigh, John William Strutt Baron. *The theory of sound*. Vol. 2. Macmillan, (1896).

[90] Gurunathan, R., Hanus, R. & Snyder, G. J. Alloy scattering of phonons. *Mater. Horizons* **7**, 1452–1456 (2020).

[91] Slack, G. A. Thermal conductivity of potassium chloride crystals containing calcium. *Phys. Rev.* **105**, 832–842 (1957).

[92] Slack, G. A. The Thermal Conductivity of Nonmetallic Crystals. *Solid State Phys. - Adv. Res. Appl.* **34**, 1–71 (1979).

[93] Gurunathan, R., Hanus, R., Dylla, M., Katre, A. & Snyder, G. J. Analytical Models of Phonon-Point-Defect Scattering. *Phys. Rev. Appl.* **13**, 1 (2020).

[94] Migliori, A. *et al.* Resonant ultrasound spectroscopic techniques for measurement of the elastic moduli of solids. *Phys. B Phys. Condens. Matter* **183**, 1–24 (1993).

[95] Migliori, A.; Maynard, J. *Review of scientific instruments*, 76, 121301 (2005).

[96] Visscher, W. M., Migliori, A., Bell, T. M. & Reinert, R. A. On the normal modes of free vibration of inhomogeneous and anisotropic elastic objects. *J Acoust Soc Am* **2162**, 2154–2162 (1991).

[97] Zadler, B. J., Le Rousseau, J. H. L., Scales, J. A. & Smith, M. L. Resonant ultrasound spectroscopy: Theory and application. *Geophys. J. Int.* **156**, 154–169 (2004).

[98] Leisure, R. G., & Willis, F. A. Resonant ultrasound spectroscopy. *Journal of Physics: Condensed Matter*, *9*(28), 6001.(1997).

[99] Introduction to Alamo Creek Engineering, http://www.rusalamocreek.com/, (Accessed on 06/25/2023), 2023.

[100] Balakirev, F. LANL RUS data acq package, https://github.com/ffb- LANL/resonant-ultrasound/releases, 2019

[101] Balakirev, F. F., Ennaceur, S. M., Migliori, R. J., Maiorov, B. & Migliori, A. Resonant ultrasound spectroscopy: The essential toolbox. *Rev. Sci. Instrum.* **90**, (2019).

[102] *LFA 467 HyperFlash* (2022) *NETZSCH*. Available at: https://analyzing-testing.netzsch.com/en-US/products/thermal-diffusivity-and-conductivity/lfa-467-hyper-flash-light-flash-apparatus (Accessed: 28 June 2023).

[103] *Ulvac Zem-3.* Available at https://www.ulvac.com/userfiles/files/Components/Thermal-Analysis-and-Coating/Thermoelectric-Testers/ZEM-3.pdf (Accessed: 28 June 2023).

[104] Hall, E. H. On a New Action of the Magnet on Electric Currents. **2**, 287–292 (1879).

[105] Li, S.P., Li, J.Q., Wang, Q.B., Wang, L., Liu, F.S. and Ao, W.Q. Synthesis and thermoelectric properties of the (GeTe) 1-x (PbTe) x alloys. *Solid state sciences*, *13*(2), pp.399-403. (2011).

[106] O. Madelung, U. Rössler, M. S. (ed. . Germanium telluride (GeTe) heat capacity, density, melting point. *Non-Tetrahedrally Bond. Elem. Bin. Compd. I* **724**, 1–2 (2005).

[107] Beattie, A. G., Temperature Dependence of the Elastic Constants of Tin Telluride *J. Appl. Phys*., 40, 4818–4821, (1969).

[108] Isotta, E. *et al.* Effect of Sn oxides on the thermal conductivity of polycrystalline SnSe. *Mater. Today Phys.* **31**, 100967 (2023).

[109] Seddon, T., Farley, J. M. & Saunders, G. A. An acoustic anomaly at the phase transition in GeTeSnTe alloy single crystals. *Solid State Commun.* **17**, 55–57 (1975).

[110] Xing, G. *et al.* Thermoelectric properties of p-type cubic and rhombohedral GeTe. *J. Appl. Phys.* **123**, (2018).

[111] Li, J., Zhang, X., Lin, S., Chen, Z. & Pei, Y. Realizing the High Thermoelectric Performance of GeTe by Sb-Doping and Se-Alloying. *Chem. Mater.* **29**, 605–611 (2017).

[112] Isotta, E., Peng, W., Balodhi, A. & Zevalkink, A. Elastic Moduli: a Tool for Understanding Chemical Bonding and Thermal Transport in Thermoelectric Materials. *Angew. Chemie* **135**, (2023).

[113] Chatterji, T., Kumar, C. M. N. & Wdowik, U. D. Anomalous temperature-induced volume contraction in GeTe. *Phys. Rev. B - Condens. Matter Mater. Phys.* **91**, 1–8 (2015).

[114] Suwardi, A. *et al.* Tailoring the phase transition temperature to achieve high-performance cubic GeTe-based thermoelectrics. *J. Mater. Chem. A* **8**, 18880–18890 (2020).

[115] Edwards, A. H. *et al.* Electronic structure of intrinsic defects in crystalline germanium telluride. *Phys. Rev. B - Condens. Matter Mater. Phys.* **73**, 1–13 (2006).

[116] Pashinkin, A.S., Malkova, A.S. & Mikhailova, M.S. Standard enthalpy and heat capacity of solid tin telluride. *Russ. J. Phys. Chem.* **80**, 1342–1343 (2006).

[117] Liu, Z. *et al.* Phase-transition temperature suppression to achieve cubic GeTe and high thermoelectric performance by Bi and Mn codoping. *Proc. Natl. Acad. Sci. U. S. A.* **115**, 5332–5337 (2018).

[118] Petit, A.-T.; Dulong, P.-L. "Recherches sur quelques points importants de la Théorie de la Chaleur". *Annales de Chimie et de Physique* (in French). **10**: 395–413. (1819).

[119] Siebeneck, H J [1]; Minnear, W P; Bradt, R C; Hasselman, D P.H, “Thermal diffusivity of nonstoichiometric titanium dioxide”, *J. Amer. Cer. Soc* **59**, 1 (1975).

APPENDIX:

Sample density was a critical parameter to ensure sample quality. Samples of low density would upset the many measurements that rely on models that take the density into account, including the LFA thermal data as well as the RUS data. To determine the theoretical density of samples throughout the series, a theoretical density was calculated via a linear rule of mixtures between the two end members. End-member densities were determined from literature sources [106-107] which were in good agreement in variety of sources: 6.14 g/cc for GeTe and 6.44 g/cc for SnTe. A table of measured sample densities is displayed below in Table A.1. Samples were measured both geometrically with calipers as well as via an Archimedes method and little deviation was found between measurements.

Sample Sn content	Geometric Density (g/cc)	Theoretical Density (g/cc)	% Density
0	5.85	6.14	95%
0.05	5.86	6.155	95%
0.1	6.103	6.17	99%
0.2 #4	5.91	6.2	95%
0.2 #9	5.96	6.2	96%
0.25	6.21	6.215	100%
0.3	5.92	6.23	95%
0.4 #2	6.05	6.26	96%
0.4 #7	5.98	6.26	96%
0.5	6.069	6.29	96%
0.6	6.14	6.32	97%
0.7	6.202	6.35	98%
0.75	6.37	6.365	100%
0.8	6.26	6.38	98%
0.9	6.28	6.41	98%
1	6.31	6.44	98%

Table A.1: Measured sample geometric densities. Note how samples are all at or above 95% theoretical density.

In addition to sample density, the heat capacity of samples was calculated via their stoichiometry using the Dulong-Petite law, a common approach for thermoelectric materials well above their Debye temperatures. Using known molar masses and the gas constant *R*, we calculate heat capacity with the following relation:

$$3R = \frac{M}{\#}\,C$$

Where (*M/#*) is the molar mass per atom in the crystal cell (for us, the average molar mass per atom in the unit cell, #=2), *C* is the heat capacity and *R* is the universal gas constant. A table of the heat capacities used in the study above are listed below in table A.2. Calculated values agree well with literature values for heat capacity in GeTe and SnTe [106,116-117].

Sample Sn content	Mass per atom (g/mol)	Heat Capacity (J/g K)
0	100.105	0.2492
0.05	101.25725	0.2463
0.1	102.4095	0.2436
0.2	104.714	0.2382
0.25	105.86625	0.2356
0.3	107.0185	0.2331
0.4	109.323	0.2282
0.5	111.6275	0.2235
0.6	113.932	0.2189
0.7	116.2365	0.2146
0.75	117.38875	0.2125
0.8	118.541	0.2104
0.9	120.8455	0.2064
1	123.15	0.2025

Table A.2: Calculated heat capacities for samples used in the study.